Numerical Investigation of Haemodynamics in Spiral-Inducing Grafts using Eulerian and Lagrangian Frameworks

Andres Ruiz Soler

A Thesis Submitted in Partial Fulfilment
of the Requirements of the Manchester Metropolitan University
for the Degree of Doctor of Philosophy

2017

School of Engineering
Faculty of Science and Engineering
Manchester Metropolitan University

A mis padres y hermano, por todo.

A mi abuelo, quien me inspiró a contribuir a la mejora de la salud cardiovascular.

To all of those suffering from vascular diseases with a hope that this investigation could help to improve their health, living conditions and well-being.

Abstract

A large range of vascular diseases require the replacement of blood vessels. By-pass grafting is a widely used treatment, in particular for high risk-patients, and consists of the connection of autologous/prosthetic graft and veins/arteries in order to repair the regular blood supply through occluded or damaged vessels. However, the development of stenosis due to thrombosis, atherosclerosis and intimal hyperplasia, linked to unfavourable haemodynamic patterns, reduces the long-term efficiency of the treatment. The identification of the natural blood motion as a swirling flow in the whole arterial system has resulted in new promising lines of research in cardiovascular devices in order to increase the patency rates of graft anastomoses by reproducing this physiological phenomenon.

The impact of the proposed research lies in the numerical investigation of the influence of different design parameters of novel spiral-inducing grafts on haemodynamics, with the objective of understanding the physics of the problem and determinating the most relevant geometrical parameters. Conventional Eulerian metrics highlighted the effects of the ridge cross-sectional shape and, particularly, the position of the ridge around the perimeter of the graft on inducing an enhanced swirling blood flow. The Lagrangian approach, which assumes the blood as a heterogeneous solid-liquid suspension, allows to assess the individual behaviour and movement of representative particles travelling in the continuous phase and again highlighted the influence of the ridge orientation from this perspective. The correlation between distributions of friction forces and terminal locations of particles in the wall of the host artery showed a predominant deposition in regions of low wall shear stress, in agreement with those assumptions that were initially considered as optimisation criteria.

Contents

List of Tables

List of Figures

List of Symbols and Acronyms

α [-]: Womersley number.

ρ $[kg\,m^{-3}]$: Density of the blood.

μ $[kg\,m^{-1}\,s^{-1}]$: Dynamic viscosity.

η $[kg\,m^{-1}\,s^{-1}]$: Apparent viscosity.

$\bar{\bar{\tau}}$ $[kg\,m^{-1}\,s^{-2}]$: Stress tensor.

$\boldsymbol{\tau}_w$ $[kg\,m^{-1}\,s^{-2}]$: WSS vector.

$\dot{\gamma}$ $[s^{-1}]$: Shear strain rate.

ϕ [rad]: Particle impact angle.

A_g $[m^2]$: Cross-sectional area of graft.

A_p $[m^2]$: Cross-sectional area of particle.

A_r $[m^2]$: Cross-sectional area of ridge.

C_D [-]: Drag coefficient.

C_{VM} [-]: Virtual mass coefficient.

CSR [-]: Cross-Sectional Ratio.

D [m]: Diameter of graft.

$\boldsymbol{F}_B$ $[N]$: Bouyancy force.

$\boldsymbol{F}_D$ $[N]$: Drag force.

$\boldsymbol{F}_P$ $[N]$: Pressure gradient force.

$\boldsymbol{F}_R$ $[N]$: Rotational forces.

$\boldsymbol{F}_{VM}$ $[N]$: Virtual mass force.

$\boldsymbol{g}$ $[m\,s^{-2}]$: Gravity vector.

h $[m^2\,s^{-2}]$: Helicity density.

H [m]: Pitch.

HR [-]: Height ratio.

L_1 $[m]$: Length of the semi-major axis.

L_2 $[m]$: Length of the semi-minor axis.

$\dot{m}$ $[kg\,s^{-1}]$: Mass flow rate.

m_f $[kg]$: Mass of the fluid.

m_p $[kg]$: Mass of the particle.

OSI [-]: Oscillatory shear index.

p $[Pa]$: Static pressure.

Q $[m^3\,s^{-1}]$: Volume flow rate.

R $[MPa\,s\,m^{-3}]$: Flow resistance.

Re [-]: Reynolds number.

R_n [-]: Normal restitution coefficient.

R_t [-]: Tangential restitution coefficient.

RRT $[Pa^{-1}]$: Relative Residence Time.

St [-]: Strouhal number.

T $[s]$: Waveform period.

t_1 $[s]$: Peak flow phase.

t_2 $[s]$: Reversed flow phase.

$TAWSS$ $[Pa]$: Time-Averaged Wall Shear Stress.

$TAWSSG$ [-]: Time-Averaged Wall Shear Stress Gradient.

$\boldsymbol{u}$ $[m\,s^{-1}]$: Velocity of the fluid.

$\boldsymbol{u}_p$ $[m\,s^{-1}]$: Velocity of the particle.

u_{red} $[m\,s^{-1}]$: Reduced velocity.

v $[m\,s^{-1}]$: Y-component of velocity.

v_{yz} $[m\,s^{-1}]$: Secondary velocity.

w $[m\,s^{-1}]$: Z-component of velocity.

ν $[m^2\,s^{-1}]$: Kinematic viscosity.

WR [-]: Width Ratio.

WSS $[Pa]$: Wall Shear Stress.

$\boldsymbol{x}_T$ [m]: Particle trajectory.

ABG: Arterial Bypass Graft.

AV: Arterio-Venous.

AVG: Arterio-Venous Graft.

CAD: Computer-Aided Design.

CAD: Coronary Artery Disease.

CABG: Coronary Artery Bypass Graft.

CFD: Computational Fluid Dynamics.

ePTFE: Expanded Polytetrafluoroethy-lene.

ETS: End-To-Side.

FSI: Fluid-Structure Interaction.

FVM: Finite Volume Method.

HA1: Upper wall region of the host artery.

HA2: Lateral side of the host artery at orientation 90°.

HA3: Bed region of the host artery.

HA4: Lateral side of the host artery at orientation 270°.

HPC: High Performance Computing.

IH: Intimal Hyperplasia.

LBM: Lattice-Boltzmann Method.

PET: Polyethylene Terephthalate.

PVD: Peripheral Vascular Disease.

RMS: Root Mean Squared.

SLF: Spiral Laminar Flow.

SMAHT: Small Amplitude Helical Technology.

TEO: Trailing Edge Orientation.

VFT: Vascular Flow Technologies.

Chapter 1

Introduction

1.1 Motivation

Heart and blood vessel disorders cause approximately 40 percent of deaths in the European Union with a consequent economic impact of €196 billion per year for national health systems [1]. The occlusion of arteries produced by vascular diseases or damaged vessels, particularly in high risk-patients, requires the use of prosthetic or natural grafts with a variety of possible anastomoses in order to repair the regular blood supply [2,3]. A graft anastomosis consists of the connection of an autologous or prosthetic graft and veins or arteries. Arterial Bypass Grafts (ABGs), for improving the blood flow, and Arterio-Venous Grafts (AVGs), for creating an access point for haemodialysis treatment for patients with renal diseases, are the main applications of vascular graft anastomosis. However, the development of stenosis at the junction due to thrombosis, atherosclerosis and Intimal Hyperplasia (IH) reduces the long-term efficiency of such treatments. Although the pathology of the graft failure due to the above-mentioned diseases has not been accurately elucidated, it is well documented that haemodynamic factors play an essential role [2]. Among the

different haemodynamic factors, the identification of the blood motion as a spiral flow in the whole arterial system produced by the complicated geometry and blood flow conditions of the vascular system [4] has recently inspired novel designs of prosthetic grafts which tend to mimic this natural phenomenon using helical and spiral configurations [5]. The helical flow opens a range of possible applications such as solutions for occlusion of arteries or grafts, improvement of stents performance and the diagnosis of arterial status. These potential benefits come as a result of the blood flow stabilisation, inhibition of stagnation and flow separation points, uniformity of wall shear stress, energy efficiency and enhancement of oxygen transport [4].

In parallel, Computational Fluid Dynamics (CFD) has proven its effectiveness as a powerful tool in order to characterise complex fluid flows, analyse the haemodynamic forces [6] and obtain the optimal design of graft anastomosis that improves the patency rate and minimises the graft failure and the need for re-operation. In the physiological aspect, numerical methods also allow for characterising blood using homogeneous or heterogeneous fluid models and implementing patient-specific boundary conditions, thereby increasing the rigour and accuracy of the biological model and identifying possible regions of proliferation of vascular diseases.

The combination of these two technology trends, helical/spiral prosthetic grafts and CFD simulations, will be used to elucidate the effects of inducing secondary flow motions in vascular graft anastomosis and the potential improvement in graft performance and patency rates.

1.2   Graft anastomosis

An anastomosis is a surgical connection between an autologous or prosthetic graft and veins or arteries inside the human body. From a geometrical point of view and

depending on the surgical intervention, the graft anastomoses can be executed as end-to-side (as shown in Figure 1.1), end-to-end, and side-to-side configurations [7].
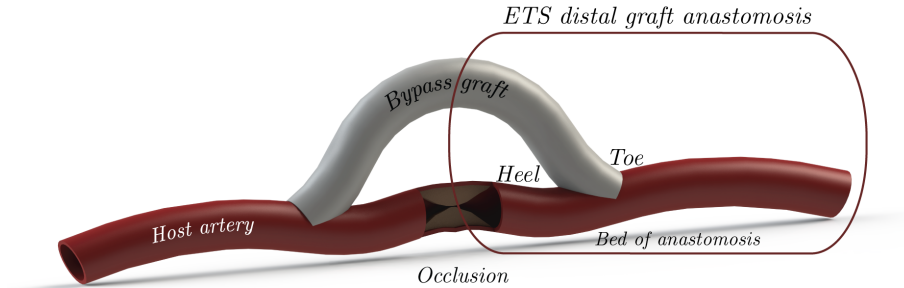
Figure 1.1: Schematic of an End-To-Side (ETS) distal graft anastomosis, subject of study in the present work.

In general, vascular grafts can be categorised under the following two main applications:

- **Arterial Bypass Grafts:** Each year over a million vascular grafts are used in current medical practice. Examples of the application of ABGs include Peripheral Vascular Disease (PVD) and Coronary Artery Disease (CAD). In ABGs, currently, the use of autologous grafts or natural vessels represents the preferential option but is adversely affected by unsuitability and unavailability of occurring vessels, particularly blood vessels less than 6 mm in diameter that are highly demanded, as well as additional surgery for the patient [8]. Hence, prosthetic grafts, following either biomaterial or tissue engineered approaches, are necessarily employed. Current prosthetic surgical options commonly include Dacron (Polyethylene Terephthalate, PET) and expanded Polytetrafluoroethylene (ePTFE). Unfortunately, prosthetic grafts are known to exhibit unsatisfactory long-term performances as a consequence of the development of stenosis in the anastomotic region [9]. Therefore, much research on graft

geometries and anastomosis designs is being performed to reduce failure rates and improve patency rates, particularly for vessels under 6 mm in diameter.

- **Arterio-Venous Grafts:** AVGs are mainly used for creating an 'access point' for haemodialysis treatments for patients with renal diseases. The recent increase in the incidence of diabetes mellitus and the need for haemodialysis in patients with this disorder has expanded the number of patients who require the implantation of ePTFE grafts for vascular access.

1.3   Physiological mechanisms of graft failure

The widely accepted role of haemodynamic conditions on physiological mechanisms associated with graft failure has been extensively shown in literature [7,10,11]. However, despite the identification of this influence, there is still no unanimity about the relationship between haemodynamic metrics and physiological mechanisms linked to the development of the most common vascular diseases resulting in graft failure: thrombosis, atherosclerosis, intimal hyperplasia and stenosis.

Thrombosis is a blood clot, thrombus, produced by the adhesion and accumulation of platelets and red blood cells which entails the risk of rupture and diffusion through the bloodstream. Thrombosis has been clinically associated with the diagnosis of atherosclerosis [12]. Haemodynamically, this disease has been linked to patterns of low velocity and retrograde flow or recirculation which are observed in stenoses. It is also considered as an initiating factor of early failure in small diameter vascular grafts due to the low blood flow rate [12–14]. However, once again, discrepancies can be observed in literature and other theories attribute high levels of shear stress with platelet accumulation [10].

Atherosclerosis is characterised by the narrowing of an artery because of the formation and development of plaque and represents one of the leading causes of death [15]. Atherosclerotic lesions arise due to the accumulation of atherogenic lipids [16] and are associated with abnormal flow conditions, flow separation and recirculation, which can also be induced as a result of postsurgical treatments [4]. These flow patterns are characterised by low and oscillatory wall shear stress [10, 17–19]. In this sense, Malek *et al.* [15] state the threshold in shear stress of $0.4\ Pa$ under which the region is prone to develop atherosclerosis.

Intimal hyperplasia represents the main cause of failure in distal end-to-side anastomoses due to the proliferation of smooth muscle cells that occlude the blood vessel lumen [7, 20–24]. Particularly in prosthetic grafts and ETS anastomotic configurations, intimal hyperplasia has been mainly identified at region of flow separation (i.e. toe and heel, see Figure 1.1), suture lines and bed of anastomosis [25, 26] and, therefore, linked to the surgical deployment and design of the anastomosis.

As mentioned above, atherosclerosis and intimal hyperplasia can produce the abnormal and severe narrowing of a blood vessel, known as stenosis [27]. As a result of the geometrical modification of the fluid domain, haemodynamics is affected by non-uniform conditions downstream of the region of stenosis, characterised by flow separation and recirculation [6, 12]. The degree of stenosis directly influences the blood velocity (associated with the Venturi effect), pressure loss, flow separation, turbulence and viscous losses. From stenoses greater than 50%, pressure loss becomes significant and flow separation occurs under extremely low Reynolds number, in the order of 10 [10, 11].

1.4 Spiral motion of blood flow

One of the most significant contributions to the improvement of haemodynamics in grafts was based on the identification of the natural blood flow as spiral in the whole arterial system. This behaviour is induced by the pulsatile nature of the flow [28] and the rotational compressive pumping of the heart [29] that is supported by the tapered, elastic, curved and non-planar geometry of the arterial system [30, 31].

Spiral blood flow has been identified in the right distal superficial and common femoral arteries [28], across the ascending [32] and descending aorta [33], right coronary artery and common iliac arteries [24, 30, 34–38]. It has also been observed in the intracranial, carotid siphon, and pulmonary, right pulmonary artery, vascular systems [39, 40]. However, the rotational direction of the flow pattern has been shown as variable depending on the blood vessel and the cardiac phase.

The benefit of this flow pattern and the relevance of spiral grafts lie in avoiding the deposition of blood cells, stabilising the motion, increasing the uniformity of Wall Shear Stress (WSS), decreasing the energy dissipation and removing unfavourable haemodynamic environments such as turbulence, stagnation and oscillatory shear stress [4, 28, 37], which are believed to be the main causes of IH at anastomotic configurations. The oxygen and mass transports are favoured by the sweep effect in the presence of atherosclerotic plaque in the arterial wall [36, 41]. Furthermore, helical flow has been hypothesized as a potential mechanism to assess the propensity to arterial diseases [42, 43] as well as to avoid the occlusion or re-stenosis in prosthetic grafts, stents and arteriovenous shunts as a result of the increased WSS and velocity components near the arterial wall [24].

The present investigation will be developed in concordance with this physiological revelation and the new designs of prosthetic grafts, introduced in Chapter 2,

that have started to take a new direction toward improving the patency of grafts by mimicking this novel flow field augmentation.

1.5   Rheology of the blood

Blood is a complex multi-phase fluid composed of particles (red blood cells, white blood cells and platelets) travelling in a continuous phase (blood plasma). Except under elongational stress, blood plasma can be considered as a Newtonian fluid, i.e. liquid with constant viscosity. The volume concentration and different mechanical properties of haematocrit, that can amount about 40 to 45%, generates the non-Newtonian behaviour of the blood. This effect, predominantly induced by the high concentration and mechanical properties of red blood cells, is presented in the form of shear thinning, viscoelasticity, thixotropy and yield stress [44]. The decrease in viscosity with increasing levels of shear rates is known as shear thinning [45]. The linear viscoelastic behaviour of blood is associated with the reversible deformation of the three-dimensional microstructure of red blood cells, knows as rouleaux, and is particularly identified at low shear rates and under pulsatile conditions [45, 46]. In addition to the low load conditions required for the aggregation of red blood cells, the composition of the continuous phase and, particularly, fibrinogen plasma protein have been also linked to the formation of such structures [45, 46]. The transient formation and breakup of these three-dimensional microstructures of red blood cells define the thixotropy of blood [46]. Although this time-dependent property has reported a minor impact on blood rheology, it is predominantly observed under low shear rates over long periods of time [44, 47]. Yield stress characterises the resistance of the fluid to flow and has been linked to blood clotting and thrombus formation [46]. The rheological flow resistance is associated with the developement

7

of aggregates and, as a consequence, with the concentration of erythrocytes (red blood cells) and fibrinogen as well as the thixotropic behaviour of blood [44].

In relation to this investigation, the viscosity of blood as a non-Newtonian fluid depends on the level of shear stress. Studies in this field set a shear rate threshold of $100\ s^{-1}$ under which non-Newtonian effects are remarkable [44,45,48–51]. As alluded to above, this behaviour is particularly important in small vessels, such as capillaries, and zones of large arteries characterised by low shear rates (i.e. bends, bifurcations, anastomoses and aneurysms) due to the development of three-dimensional structures of erythrocytes [44,45,50,52–56]. The influence of these fluid flow characteristics are reported in axial and secondary flow profiles as well as steady-state and transient WSS-based metrics [57].

Despite the heterogeneous composition of blood, the most common haemodynamic approaches consider the blood as a continuous fluid and the effect of blood particles is usually simplified by using non-Newtonian models extensively studied in the literature. The most widely used non-Newtonian models in haemodynamics are Carreay-Yasuda and Casson viscosity laws. Other alternatives include power law, Herschel-Bulkley, Oldroyd-B, Yeleswarapu, Bingham, Eyring-Powell, Ree-Eyring and Quemada viscosity models [44].

1.6   Fluid mechanics

Fluid mechanics is the scientific discipline which studies the motion and behaviour of those materials unable to resist shear stress, i.e. fluids (liquids and gases). Traditionally, the description of the motion of a fluid can be simultaneously addressed using the Eulerian or Lagrangian formulation [58].

1.6.1 Eulerian and Lagrangian descriptions

The most common approach in fluid mechanics and, particularly, in haemodynamics is the Eulerian method that measures the temporal evolution of fluid magnitudes in each point of the fluid domain, $\boldsymbol{x}$. The use of this description lies in the equations of velocity and every fluid magnitude f:

$$\boldsymbol{u} = \boldsymbol{u}(\boldsymbol{x}, t) \qquad f = f(\boldsymbol{x}, t) \tag{1.1}$$

Eulerian haemodynamic metrics are used in Chapter 3 to analyse the performance of the different designs of spiral grafts.

For its part, the Lagrangian formulation assesses the fluid field by measuring fluid metrics over the motion of each fluid element through its trajectory, which allows to study the behaviour of particles. The use of this description lies in the trajectory equation over time, $\boldsymbol{x}_T$, described by the particle located in $\boldsymbol{x}_0$ at the initial time $t = t_0$ for every fluid magnitude f:

$$\boldsymbol{x} = \boldsymbol{x}_T(\boldsymbol{x}_0, t) \qquad f = f(\boldsymbol{x}_0, t) \tag{1.2}$$

Further information about different numerical Lagrangian approaches and the use of this description to study the behaviour of idealised blood particles in the different designs of spiral grafts can be found in Chapter 4.

1.6.2 Computational Fluid Dynamics

The simultaneous increase in complexity of engineering problems, that often involve multiple physics (fluid dynamics, mechanical properties, electromagnetic behaviour, design optimisation, etc.), and the power-to-cost ratio of computers have brought

with them an exponential increase in the use of numerical techniques, including computational fluid dynamics in biomedical engineering within the framework of translational medicine.

Particularly, for prosthetic grafts, research is currently being undertaken under two separate strands; the first tends to focus on tissue-engineering and biomaterial science, while the second is concerned with biomechanics, flow field augmentations and haemodynamic forces. Although both approaches are related by haemorheology and its influence in tissue perfusion [45], the attention of the present work is focused on the latter and relies on CFD to investigate the effects of secondary flow on distal graft anastomosis configurations.

The working structure for this and, in general, for any CFD study is made up of the following stages: (1) geometry definition and/or reconstruction of the fluid problem, (2) meshing of the computational domain, (3) CFD setup and specification of fluid properties, boundary conditions and parameters of the numerical procedure and, finally, (4) post-processing and analysis of results.

Software packages

The increasing and multidisciplinary use of CFD techniques has resulted in a wide variety of software packages of recognised solvency. According to the above-mentioned working structure, the software used in each of the stages of this project is enumerated as follows:

- **CAD**: ANSYS DesignModeler. Version 17.1, Academic Research CFD license. ANSYS Inc., Canonsburg, PA, USA.

- **Mesh**: ANSYS Meshing. Version 17.1, Academic Research CFD license. ANSYS Inc., Canonsburg, PA, USA.

- **CFD solver**: ANSYS CFX. Version 17.1, Academic Research CFD license. ANSYS Inc., Canonsburg, PA, USA.

- **Post-processing**: ANSYS CFD-Post (Version 17.1, Academic Research CFD license, ANSYS Inc., Canonsburg, PA, USA) and Ensight (CEI Inc., Research Triangle Park, NC, USA).

1.7 Methodology

The aim of the proposed research lies in the haemodynamic characterisation, identification of the most relevant geometrical parameters and preliminary design optimisation of spiral-inducing prosthetic grafts.

Following a comprehensive literature review and the description of the state-of-the-art in bypass grafting, different design strategies of a conventional end-to-side distal graft anastomosis with internal helical ridge are analysed in order to carry out an appropriate design comparison under the same boundary conditions. Different cross-sectional designs, orientations, pitches and number of the ridges have been tested here in order to determine the effect of each design parameter on haemodynamics and, consequently, on physiological mechanisms associated with the development of stenosis, thrombosis, atherosclerosis and intimal hyperplasia.

The Eulerian description of fluid mechanics represents the traditional approach of computational haemodynamics by considering the blood as a continuous and non-Newtonian fluid. Both steady-state and unsteady flow conditions will be introduced in this research to simulate physiological conditions of the circulatory system. Some of the haemodynamic metrics which will be investigated in this project include secondary flow, Wall Shear Stress (WSS), pressure drop, helicity, retrograde flow,

Oscillatory Shear Index (OSI), Time-Average WSS (TAWSS), TAWSS Gradient (TAWSSG) and Relative Residence Time (RRT). Further information about these haemodynamic parameters and their mathematical definitions will be presented in Chapter 3. Widely accepted assumptions about the above-mentioned fluid dynamic metrics will be used to justify the potential correlation with physiological mechanisms associated with the formation and development of vascular diseases and to assess the graft performance.

In line with the above, the combination of Eulerian and Lagrangian descriptions provides a different haemodynamic approach by considering the blood as a heterogeneous solid-liquid suspension. This computational procedure enables to account the transport and tracking of blood particles and, as a result, to study the regions of deposition prone to the development of vascular diseases without the need of intermediary hypothesis, often contradictory.

1.8 Organization of the thesis

This thesis *'Numerical Investigation of Haemodynamics in Spiral-Inducing Grafts using Eulerian and Lagrangian Frameworks'* covers the assessment of design parameter effects on haemodynamics in a novel spiral-inducing prosthetic graft from the two theoretical descriptions of fluid mechanics.

The remainder of this report is organised as follows. Chapter 2 reviews the current status of bypass graft design and geometrical parameters studied in the literature together with their effects on haemodynamics. The design strategy for the spiral-inducing graft assumed throughout the project will be introduced in this chapter. Chapter 3 describes the use of the traditional Eulerian description, considering the blood as a homogeneous fluid, in order to understand the physics of the fluid

problem and compare the influence of the different design parameters on the fluid flow field. Chapter 4 explores the use of the non-conventional Lagrangian approach by considering the blood as a heterogeneous multi-phase mixture and enabling the assessment of discrete particle trajectories and their deposition on the anastomotic region. Lastly, conclusions and an outline of future work, which complements this study, are drawn in Chapter 5.

Chapter 2

Problem Definition

2.1 Introduction

The direct influence of the domain geometry and fluid conditions on haemodynamics has resulted in an extensive research into design parameter effects associated with bypass anastomoses and prosthetic grafts.

This chapter will review previous works studying geometrical factors as a basis for deepening knowledge related to current designs of spiral-inducing grafts and its surgical deployment. The common characteristics of the problem using the Eulerian and Lagrangian frameworks will also be defined in terms of geometrical and fluid dynamic conditions. Once the operating point of prosthetic grafts is specified, two different design strategies are proposed in order to assess the effect of ridge designs on the blood flow. The design strategy will be selected in order to ensure that the different geometrical designs are compared under the same boundary conditions and particularly, under a similar pressure drop or vascular resistance.

Therefore, all geometrical and fluid dynamic parameters followed throughout this study will be defined in the following sections.

2.2 Literature review

2.2.1 Geometrical parameters in bypass anastomoses and prosthetic grafts

Since flow patterns are directly related to the geometry of the bifurcation, the design of the graft and its connection to the host artery, much research has addressed the effect of a large range of design parameters in bypass anastomoses and prosthetic grafts.

Tissue remodelling and the patency rate of grafts have been related to the anastomotic angle [2], among other factors. Low angles have mainly reported more uniform haemodynamic metrics and reduction of peak and oscillatory values of WSS [59–65]. In contrast, Do *et al.* [6] studied the effect of the anastomotic angle in a partially occluded end-to-side distal graft anastomosis showing a decrease in reverse flow with a certain increase of the angle.

Graft diameter has been shown as an important parameter in the biological response to this treatment. While grafts of small diameter can lead to vessel occlusion and early graft failure due to platelet thrombosis as a result of the overstimulation produced by high levels of shear stress [10, 66, 67], high-diameter grafts can induce intimal thickening because of low shear stress and abnormal flow conditions, i.e. flow separation and recirculation [10]. Despite this fact, large graft calibers are generally preferred in order to induce more uniform distributions of WSS and to avoid spatial and temporal oscillations of WSS-based haemodynamic metrics [59, 68, 69].

Out-of-plane configurations have reported lower temporal oscillations of WSS as well as improved flow patterns in the occluded region when compared with conventional designs [70, 71]. The enhanced behaviour has been associated with the

introduction of a circumferential velocity component to the bulk velocity of blood that results in the dissipation of conventional Dean vortices into a single dominant vortex. The reduction and increase of the helical pitch and amplitude, respectively, have been suggested to improve the graft performance [72]. However, the deployment of non-planar graft configurations can be restricted by surgical factors [73].

Other studies have gained an insight into different configurations of distal graft anastomosis by introducing hoods [74] and cuffs [75] with the purpose of improving the adaptation of the blood flow and redistributing the development of IH at the anastomosis.

2.2.2 Helical and spiral grafts

Building on the benefits of the physiological spiral flow of blood, described in Chapter 1, two of the most innovative designs of prosthetic grafts are Spiral Flow Graft and SwirlGraft:

- **Spiral Flow Graft:**

  'Spiral Laminar Flow (SLF) Peripheral Vascular Graft', initially studied by Stonebridge and colleagues [31,37] at Ninewells Hospital in Dundee (Scotland) and subsequently commercialised by Vascular Flow Technologies (VFT) Ltd., consists of a prosthetic ePTFE graft design that is engineered to induce spiral flow through an internal ridge within its distal end. The results of an early clinical non-randomised study for VFT peripheral bypass graft were promising and showed primary patency rates of 81% for above-the-knee bypasses and 57.3% for below-the-knee bypasses at 30 months of follow-up. The respective secondary patency rates were 81% and 64% [81]. Similar improvements were also found when using the spiral flow graft for AV access for haemodialysis

('Spiral Flow AV Access Graft'). Through inducing spiral blood flow using an internal ridge, the SLF graft is claimed to: 1) reduce laterally directed forces and near-wall turbulence, 2) suppress acute thrombus formation with no increase in platelet activation, 3) reduce WSS gradient and oscillatory shear index, 4) enhance oxygen flux to the arterial wall and 5) reduce luminal surface low-density lipoproteins concentration [5,82]. While the initial results reported in [81] highlight the potential for the idea of spiral-inducing grafts in bypass surgeries, in a very recent clinical investigation, Bechara [82] carried out a single-centre study on patients undergoing infrainguinal bypass using VFT's spiral laminar flow graft compared against Propaten (a heparin-bonded ePTFE graft produced by W.L. Gore) and found that the spiral laminar flow graft had not led to higher patency rates in comparison to the conventional ePTFE grafts. This finding highlights the need for further investigation on the design and improving the performance of these grafts with more effective spiral ridges.

- **SwirlGraft:**

'SwirlGraft', developed by Caro and colleagues [76] at Veryan Medical Ltd., is a new Arterio-Venous (AV) shunt graft with a helical out-of-plane geometric feature, also known as 'SMall Amplitude Helical Technology' (SMAHT). Compared to a conventional ePTFE graft, the animal experiments reported in [76] demonstrated that there was less thrombosis in SwirlGraft. The difference became even more significant after 8 weeks of implementation. To date, a number of researchers have simulated the blood flow in out-of-plane grafts geometries that induce 3D swirling [70–72, 77–79]. Whilst the majority of the previous numerical simulations have studied the helical flow using various

mean flow and wall shear stress-based haemodynamic parameters, Cookson *et al.* [77] used high-order particle tracking, and an information entropy measure to understand and quantify the mixing effect in helical geometries and found the optimal helical geometry, in terms of mixing versus pressure loss. SMAHT has also inspired other novel flow field augmentation techniques including the work of Cookson *et al.* [80] which has shown that joining together two helical geometries, of different helical radii, would enhance mixing, with a minor increase in pressure loss [77].

Recent investigations by the author's research group [83] suggest that the combination of a spiral ridge(s) with graft out-of-plane helicity can further enhance the swirling effect in the flow. However, whilst several researchers have numerically simulated the blood flow in out-of-plane graft geometries [70–72, 77–79], there are currently very few research papers in the literature investigating grafts with internal spiral ridges [4]. Therefore, the focus of this thesis will be restricted to this type of graft, with an aim of understanding the flow physics and haemodynamic forces and improving the ridge design through conducting a parametric study on various geometrical parameters. This research would have a wide range of beneficiaries including hospitals and the healthcare systems, medical practitioners and the therapeutic technology industry.

2.3 Problem definition

2.3.1 Geometrical definition

In the present study, the design of a novel spiral-inducing graft has been assessed from the haemodynamic point of view. Figure 2.1 represents the simplified geometry

of an End-To-Side (ETS) distal graft anastomosis, that connects the prosthetic graft and host artery with an angle of 60 degrees, according to experimental studies by Kokkalis *et al.* [5] and in line with previous work carried out by the author's research group [83]. The internal diameters of host artery and graft are set to 6 mm, according to the order of magnitude of a peripheral artery bypass grafting.

The stenosis is considered complete and, therefore, the blood flow through the graft is not affected by competitive flow from the stenosis. The distance between the stenosis and heel of anastomosis is 12.92 mm, approximately 2 times the diameter of the graft, in concordance with the experimental model of Spiral Laminar Flow Peripheral Vascular Graft (Vascular Flow Technologies Ltd., Dundee, UK) assessed by Kokkalis *et al.* [5].

The swirling flow is induced by means of one or more spiral ridges in the internal wall of the graft. In order to understand the haemodynamic effects of the ridge design, different cross-sectional shapes, orientations, number and pitches of the ridge have been tested by means of the design approaches A and B, explained in Section 2.4. Three different monitoring planes located at 1 mm, 5 mm and 50 mm distal from the toe of the anastomosis have been considered in order to evaluate the haemodynamic parameters in the host artery, in line with the experimental procedure carried out by Kokkalis *et al.* [5].
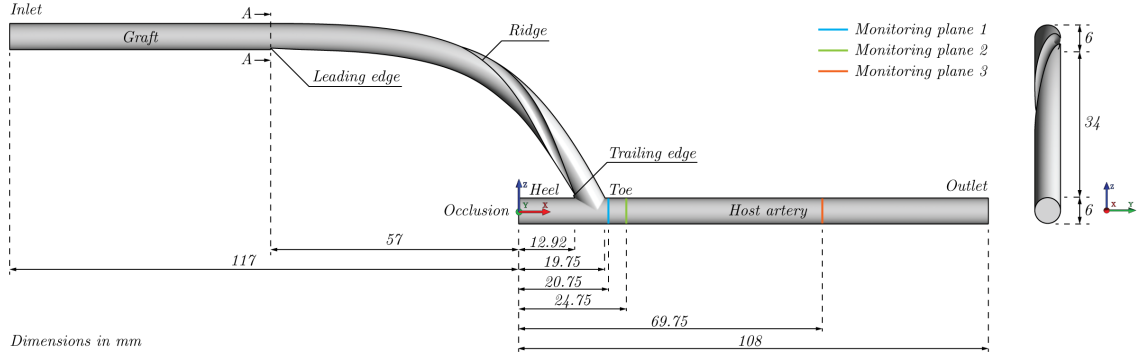
Figure 2.1: Schematic of the computational model.

2.3.2 Dynamic definition

The Reynolds number, Re, is a dimensionless fluid dynamic parameter that represents the ratio of inertial to viscous forces and provides an estimation of the flow regime: laminar or turbulent.

$$Re = \frac{\rho V D}{\mu} \tag{2.1}$$

Where ρ is the density of the fluid, V is the velocity of the fluid, μ is the dynamic viscosity and D is the characteristic distance, i.e. the diameter of graft or host artery. In the present problem, the Reynolds number has been set to $Re = 570$, according to a normal flow condition in the peripheral system [5, 84]. Consequently, the flow regime can be assumed as laminar.

When implementing transient flow conditions, the pulsatile behaviour can be characterised by the Womersley number, α, that describes the ratio of transient inertial forces to viscous forces or the reduced velocity, u_{red}, that is the inverse of

20

the Strouhal number and represents the relationship between the distance travelled by the mean flow and the diameter [85].

$$\alpha = \frac{D}{2}\sqrt{\frac{2\pi}{vT}} \qquad\qquad u_{red} = \frac{1}{St} = \frac{uT}{D} \qquad\qquad (2.2)$$

Where v is the kinematic viscosity ($v = \mu/\rho$), T represents the period of the pulsatile cicle and St is the Strouhal number. As will be observed in Chapters 3 and 4, the patient-specific velocity waveform implemented at the inlet results in a Womersley number of 4.34.

The boundary condition at the inlet was specified in terms of velocity according to the aforementioned Reynolds number. Fully developed flow is ensured by the initial extension of the graft of 60 mm, ten times the diameter of the graft and host artery [86]. At the outlet, zero pressure conditions were considered [6, 87]. Further details related to the different fluid dynamics approaches considered throughout this study (Eulerian or Lagrangian frameworks) will be explained in Chapters 3 and 4.

The walls have been considered as rigid and non-slip [6, 71, 83]. Although the assumption of rigid walls is far from being physiological at certain flow regimes in arteries and veins, Ku *et al.* [10] showed that this premise can be considered acceptable for Reynolds and Womersley numbers in the range of (100, 1000) and (1, 10), respectively, as is in this case, in which the influence of wall elasticity is reduced. Other computational investigations [88, 89] also reported a minor effect of compliance mismatch on local haemodynamics.

2.4 Design strategies

The evolution of the design strategy used throughout this study is presented here. Both design strategies consider the influence of the cross-sectional shape (circular and elliptical ridges), orientation of the trailing edge, number of ridges and different ridge pitches. With the purpose of analysing the effect of such geometrical parameters on the blood flow under similar dynamic conditions, the suitability of design strategies A and B (defined below) is assessed in terms of the pressure drop and flow resistance produced in the fluid domain.

Note that in all design schematics, the direction of the blood flow should be interpreted as moving into the page.

2.4.1 Design Strategy A

The initial design strategy of spiral ridge(s) was considered by independently assessing the height and width of the spiral as well as the number of ridges without preliminary constraints in terms of total cross-sectional area.

Cross-sectional designs

Different sizes of circular and elliptical ridges were tested in order to assess the effect of the cross-sectional shape. In the case of the circular ridge, the variation of the size is defined through the Cross-Sectional Ratio (CSR):

$$CSR = \frac{A_r}{A_g} \tag{2.3}$$

where A_r and A_g represent the cross-sectional area of the ridge and graft, respectively. The cross-sectional area of the graft is 28.27 mm^2 corresponding to a graft diameter of 6 mm.

The effects of the elliptical ridge have been studied separately. The variation of the height is assessed (keeping the width of the ellipse fixed), by defining the Height Ratio (HR) as:

$$HR = \frac{L_1}{D} \tag{2.4}$$

where L_1 is the length of the semi-major axis, D is the diameter of the graft and L_2 is set to 0.9 mm.

Similarly, the variation of the width is studied (by keeping the height of the ellipse fixed), through defining the Width Ratio (WR) as:

$$WR = \frac{L_2}{D} \tag{2.5}$$

where L_2 is the length of the semi-minor axis and L_1 is set to 0.9 mm.

In the numerical tests conducted in the this study, the values of 5, 15 and 30% have been assigned to the parameters that define the size of the ridge (i.e. CSR, HR and WR).

Orientation of the ridge

The procedure to analyse the impact of orientation of the trailing edge on haemodynamics involves the rotation of the centre of the ridge to the positions 0°, 90°, 180° and 270°. The trailing edge orientations 0° and 180° represent the toe and heel of the anastomosis, respectively. The case of single circular ridge and $CSR = 15\%$

Cross-Sectional Designs

Circular Ridge   Elliptical Ridge - Height   Elliptical Ridge - Width
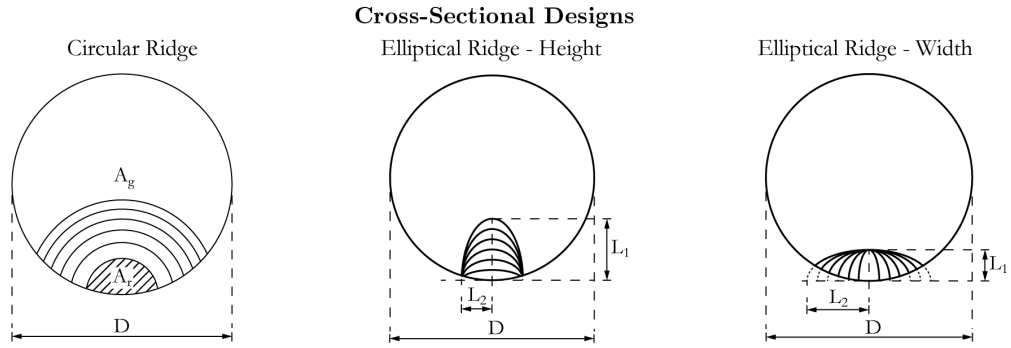
Figure 2.2: Schematic of the different cross-sectional shapes of ridge considered in design strategy A.

was selected as a reference size to assess the effects of different ridge trailing edge orientations.

Orientation of the Ridge

0º   90º   180º   270º
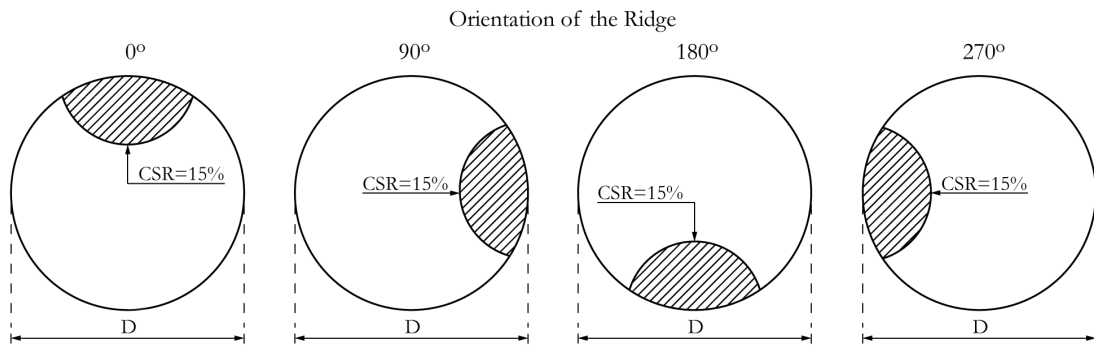
Figure 2.3: Schematic of the different orientations of ridge considered in design strategy A.

Number of ridges

The effects of the number of ridges were assessed by means of three configurations with single, double and triple ridges. The circular ridge with $CSR = 15\%$ was chosen as a reference size to generate the equally-spaced multi-ridge designs.
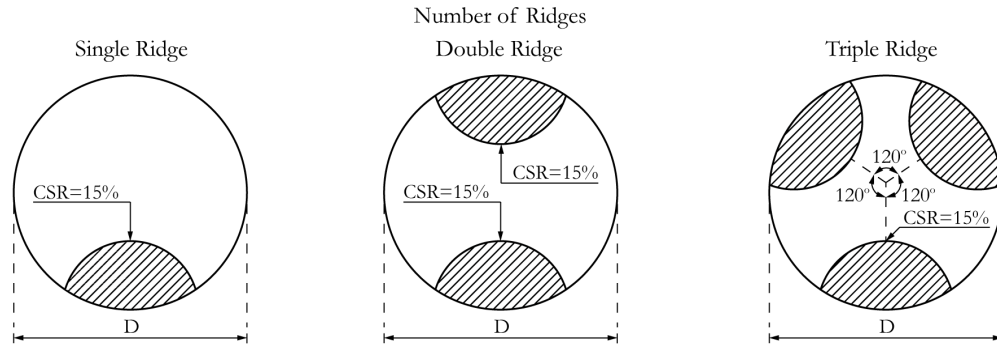
Figure 2.4: Schematic of the different multi-ridge configurations considered in design strategy A.

Pitch of the ridge

The influence of the pitch, H, on haemodynamics was evaluated through a variation of $\pm 20\%$ in the helical pitch of the single circular ridge with $CSR = 15\%$ ($H_{ref} = 86.54\ mm$). In all cases, the orientation of the ridge was set as in the reference case (i.e. $180°$).
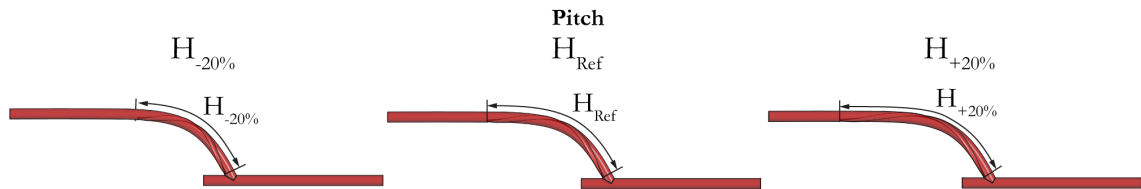
Figure 2.5: Schematic of the the different ridge pitches considered in design strategy A.

All aforementioned features that define the different geometrical configurations in design strategy A are summarised in Table 2.1.

2.4.2 Design Strategy B

With the purpose of comparing the different design of spiral grafts under similar fluid dynamic conditions, the design strategy B evaluates similar graft configurations to

Table 2.1: Features of the different configurations of ridge design considered in design strategy A.

			L_1 [mm]	L_2 [mm]	Orientation of the ridge(s)	Number of ridge(s)	Pitch [mm]
Cross-sectional designs	*Elliptical Height*	*HR 30%*	1.8	0.9	180°	1	86.54
		HR 15%	0.9	0.9	180°	1	86.54
		HR 5%	0.3	0.9	180°	1	86.54
	Circular ridge	*CSR 30%*	2.58	2.58	180°	1	86.54
		CSR 15%	1.76	1.76	180°	1	86.54
		CSR 5%	0.98	0.98	180°	1	86.54
	Elliptical Width	*WR 30%*	0.9	1.8	180°	1	86.54
		WR 15%	0.9	0.9	180°	1	86.54
		WR 5%	0.9	0.3	180°	1	86.54
Trailing edge orientation		0°	1.76	1.76	0°	1	86.54
		90°	1.76	1.76	90°	1	86.54
		180°	1.76	1.76	180°	1	86.54
		270°	1.76	1.76	270°	1	86.54
Number of ridges		*Single*	1.76	1.76	180°	1	86.54
		Double	1.76	1.76	0°, 180°	2	86.54
		Triple	1.76	1.76	60°, 180°, 300°	3	86.54
Pitch		$H_{+20\%}$	1.76	1.76	180°	1	103.85
		H_{ref}	1.76	1.76	180°	1	86.54
		$H_{-20\%}$	1.76	1.76	180°	1	69.23

the ones described above but also implementing the constraint of constant total cross-sectional area of ridge(s).

Cross-sectional designs

The effect of the cross-sectional shape on haemodynamics was also assessed by considering circular and elliptical ridges. In this case, the circular ridge is considered as the reference case for further design parameters and the radius is set to 1.5 mm, giving a ratio of approximately 10% between the cross-sectional area of the ridge and graft (i.e. blockage ratio). The effects of the elliptical ridge have been studied through the variation of the vertical semi axis and keeping the cross-sectional area of the ridge fixed. As shown in Figure 2.6, in the numerical tests conducted here, the ratio between the vertical semi axis, L_1, and the diameter of the graft, D, is

set to 0.2 (elliptical ridge - width), 0.25 (circular ridge) and 0.3 (elliptical ridge - height).

Cross-Sectional Designs

Elliptical Ridge - Width · · · · · · Circular Ridge · · · · · · Elliptical Ridge - Height

$L_1=0.2D$
$L_2=0.385D$

$L_1=L_2=0.25D$

$L_1=0.3D$
$L_2=0.197D$

L_1

L_2

L_1

L_2

L_1

L_2
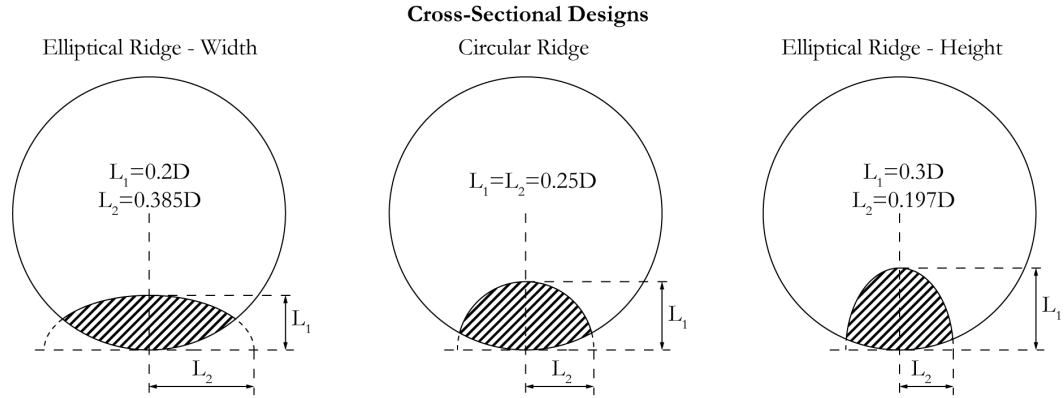
Figure 2.6: Schematic of the different cross-sectional shapes of ridge considered in design strategy B.

Orientation of the ridge

Similarly, the procedure to analyse the impact of the ridge trailing edge orientation on haemodynamics again involves the rotation of the centre of the ridge to the positions 0°, 90°, 180° and 270°, along the circumference of the graft, near the anastomosis. Note that the case of single circular ridge that was selected as the 'reference' configuration corresponds to the trailing edge orientation 180°, consistent with the current design of VFT's 'Spiral Flow Peripheral Vascular Graft' [5].

Number of ridges

The effects of the number of ridges were also assessed by means of three configurations with single, double and triple ridges. The single circular ridge is chosen as the reference cross-sectional shape to generate equally-spaced ridges. However, in the multi-ridge configurations, the radius of the circular ridges is decreased to keep
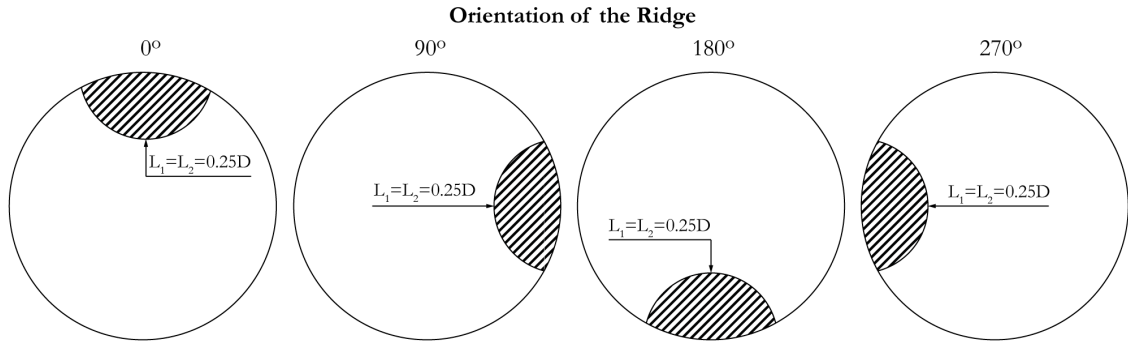
Figure 2.7: Schematic of the different orientations of ridge considered in design strategy B.

the total cross-sectional area fixed at 3.157 mm^2 for all three cases. Therefore, the radius of the ridge would be 1.04 mm and 0.84 mm in the double and triple ridge configurations, respectively.
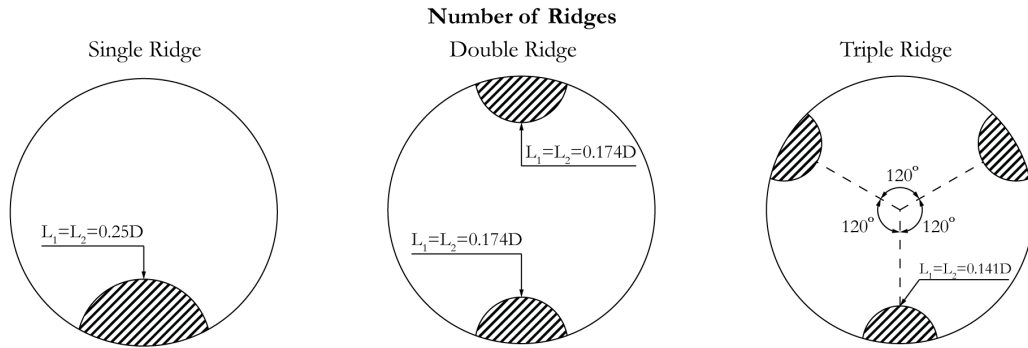
Figure 2.8: Schematic of the different multi-ridge configurations considered in design strategy B.

Pitch of the ridge

Similar variations of ridge pitch to those taken in design approach A and illustrated in Figure 2.5, were also considered in design strategy B. In constrast, the cross-sectional areas of the ridge were set as in the reference case of design approach B, i.e. single circular ridge with $L_1 = L_2 = 1.5$ mm.

All aforementioned features that define the different geometrical configurations in design strategy B are summarised in Table 2.2.

Table 2.2: Features of the different configurations of ridge design considered in design strategy B.

		L_1 [mm]	L_2 [mm]	Orientation of the ridge(s)	Number or ridges	Pitch [mm]
Cross-sectional designs	*Elliptical - Height*	1.8	1.18	180°	1	86.54
	Circular ridge	1.5	1.5	180°	1	86.54
	Elliptical - Width	1.2	2.31	180°	1	86.54
Trailing edge orientation	0°	1.5	1.5	0°	1	86.54
	90°	1.5	1.5	90°	1	86.54
	180°	1.5	1.5	180°	1	86.54
	270°	1.5	1.5	270°	1	86.54
Number of ridges	*Single*	1.5	1.5	180°	1	86.54
	Double	1.04	1.04	0°, 180°	2	86.54
	Triple	0.84	0.84	60°, 180°, 300°	3	86.54
Pitch	$H_{+20\%}$	1.5	1.5	180°	1	103.85
	H_{ref}	1.5	1.5	180°	1	86.54
	$H_{-20\%}$	1.5	1.5	180°	1	69.23

2.5 Discussion

The numerical simulation of the above-mentioned configurations enables the analysis of haemodynamic parameters such as the distributions of secondary velocity magnitude and flow resistance in the fluid domain. Further details about the computational model used in these simulations as well as the complete analysis of results will be given in Chapters 3 and 4.

Figures 2.9 and 2.10 represent the distributions of secondary velocity at monitoring plane 3, located at 50 mm distal from the toe of the anastomosis where the effects of the swirling motion are more meaningful, for the different cases of both design strategies A and B described in Section 2.4. As can be observed, both design

strategies give rise to conclusions in a similar direction by highlighting the influence of the elliptical ridge, the trailing edge orientation, the increase of the number of ridges and the decrease of the ridge pitch in producing an enhanced swirling flow. However, an appropriate quantitative comparison of results requires the analysis of the different geometrical designs under the same boundary conditions and particularly, under a similar pressure drop or vascular resistance.

The appropriate blood flow supply to organs and tissues is regulated by the resistance against the flow and the consequent pressure drop. Together with the rheology of the blood, the geometry of vessels are the main parameters involved in the adjustment of blood flow by means of vasoconstrictor and vasodilator mechanisms.

The traditional description of blood in computational modelling as a homogeneous fluid together with the dynamic definition of the problem presented in Section 2.3, that will be further explained in Chapter 3, were used to analyse the resulting pressure drop or equivalent flow resistance in the fluid domain, defined in Equation 2.6 [83, 90].

$$R = \frac{\int_0^T \Delta P \; Q dt}{\int_0^T Q^2 dt} \tag{2.6}$$

Where ΔP represents the pressure drop ($\Delta P = P_{inlet} - P_{outlet}$) and Q is the volumetric flow rate.

Table 2.3 illustrates the values of pressure drop and flow resistance when the design approach is free of constraints associated with the total cross-sectional area of ridge(s). Unacceptable variations of up to 112.1% are reported when comparing with the reference case ($CSR = 15\%$), leading to an inappropriate numerical comparison due to different pressure drop conditions in the different cases.

Table 2.3: Pressure drop and flow resistance in the fluid domain for the different configurations of spiral ridge(s) using the design configuration A.

			Pressure drop $[Pa]$	Flow resistance $[MPa\ s\ m^{-3}]$
Cross-sectional design	*Elliptical ridge - Height*	*HR 30%*	550.35	61.40
		HR 15%	496.37	55.38
		HR 5%	469.81	52.42
	Circular ridge	*CSR 30%*	785.11	87.60
		CSR 15%	586.67	65.45
		CSR 5%	502.43	56.06
	Elliptical ridge - Width	*WR 30%*	507.93	56.67
		WR 15%	496.37	55.38
		WR 5%	485.17	54.13
Trailing Edge Orientation		0°	571.23	63.73
		90°	581.82	64.91
		180°	586.67	65.45
		270°	591.12	65.95
Number of ridges		*Single*	586.67	65.45
		Double	783.77	87.45
		Triple	1244.06	138.80
Pitch		$H_{+20\%}$	598.42	66.77
		H_{ref}	586.67	65.45
		$H_{-20\%}$	540.55	60.31

In contrast to approach A, the design strategy B is based on setting the total cross-sectional area of ridge(s) to be constant. This limits the difference in the pressure drop of different cases, or equivalent flow resistance, to 3.5% with respect to the reference configuration (as shown in Table 2.4), thus, making a numerically valid comparison between different design parameters.

The design strategy B was therefore the approach adopted in the present work.

Table 2.4: Pressure drop and flow resistance in the fluid domain for the different configurations of spiral ridge(s) using the design configuration B.

		Pressure drop $[Pa]$	Flow resistance $[MPa\ s\ m^{-3}]$
Cross-Sectional Design	*Elliptical - Height*	565.68	63.11
	Circular Ridge	550.34	61.40
	Elliptical - Width	535.49	59.74
Trailing Edge Orientation	0°	531.13	59.26
	90°	543.05	60.59
	180°	550.34	61.40
	270°	545.86	60.90
Number of Ridges	*Single*	550.34	61.40
	Double	546.29	60.95
	Triple	547.32	61.06
Pitch	$H_{+20\%}$	559.31	62.40
	H_{ref}	550.34	61.40
	$H_{-20\%}$	537.99	60.02

Cross-Sectional Designs

Elliptical Ridge - HR 30% Elliptical Ridge - HR 15% Elliptical Ridge - HR 5%

Circular Ridge - CSR 30% Circular Ridge - CSR 15% Circular Ridge - CSR 5%

Elliptical Ridge - WR 30% Elliptical Ridge - WR 15% Elliptical Ridge - WR 5%

Orientation of the Ridge

0°   90°   180°   270°

Number of Ridges

Single Ridge   Double Ridge   Triple Ridge

Pitch

$H_{-20\%}$ H_{Ref} $H_{+20\%}$
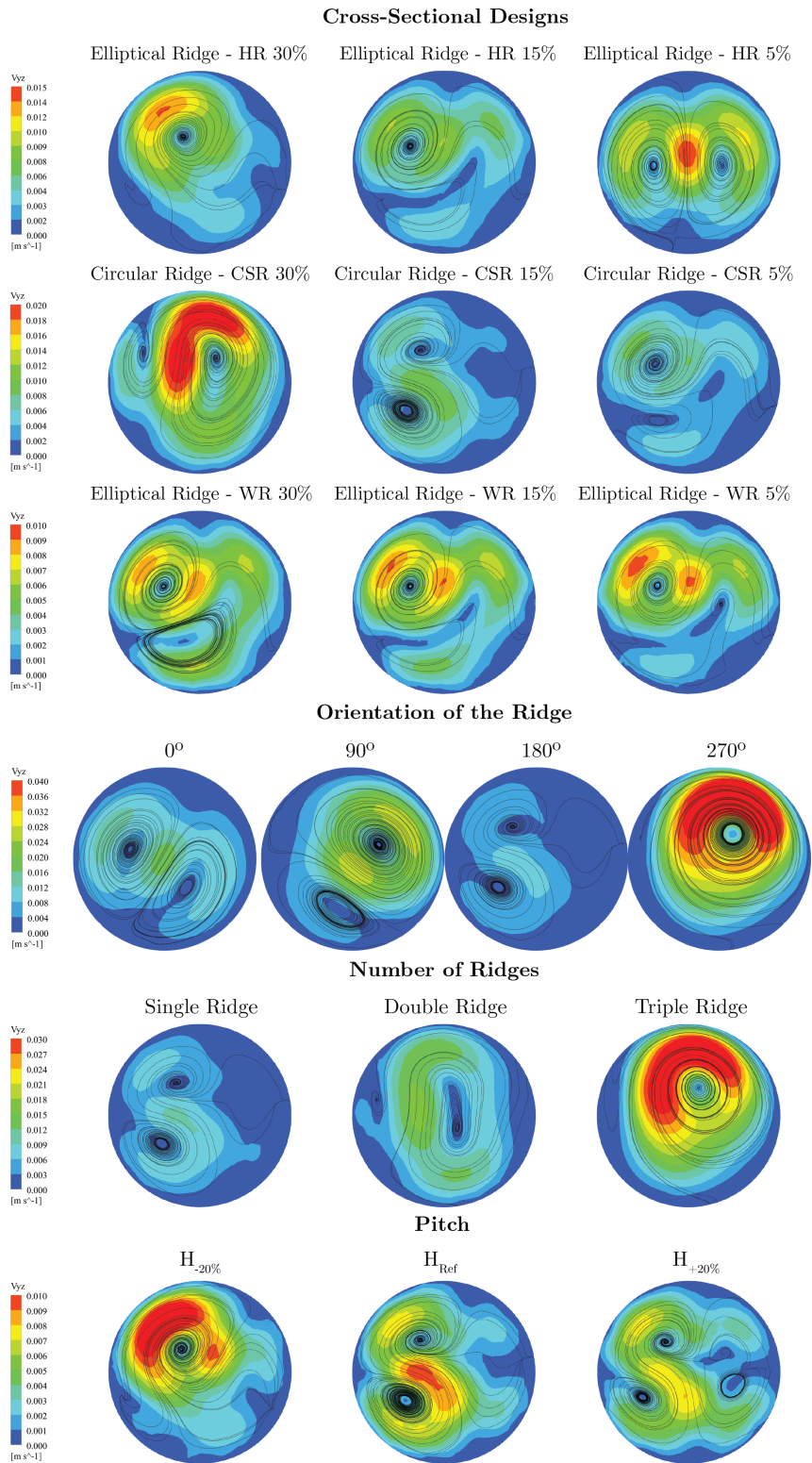
Figure 2.9: Contours of secondary velocity magnitude and crossflow streamlines for different ridge designs considered in design strategy A at monitoring plane 3.

33

Cross-Sectional Designs

Elliptical Ridge - Width   Circular Ridge   Elliptical Ridge - Height

Orientation of the Ridge

0°   90°   180°   270°

Number of Ridges

Single Ridge   Double Ridge   Triple Ridge

Pitch

H$_{-20\%}$ H$_{Ref}$ H$_{+20\%}$
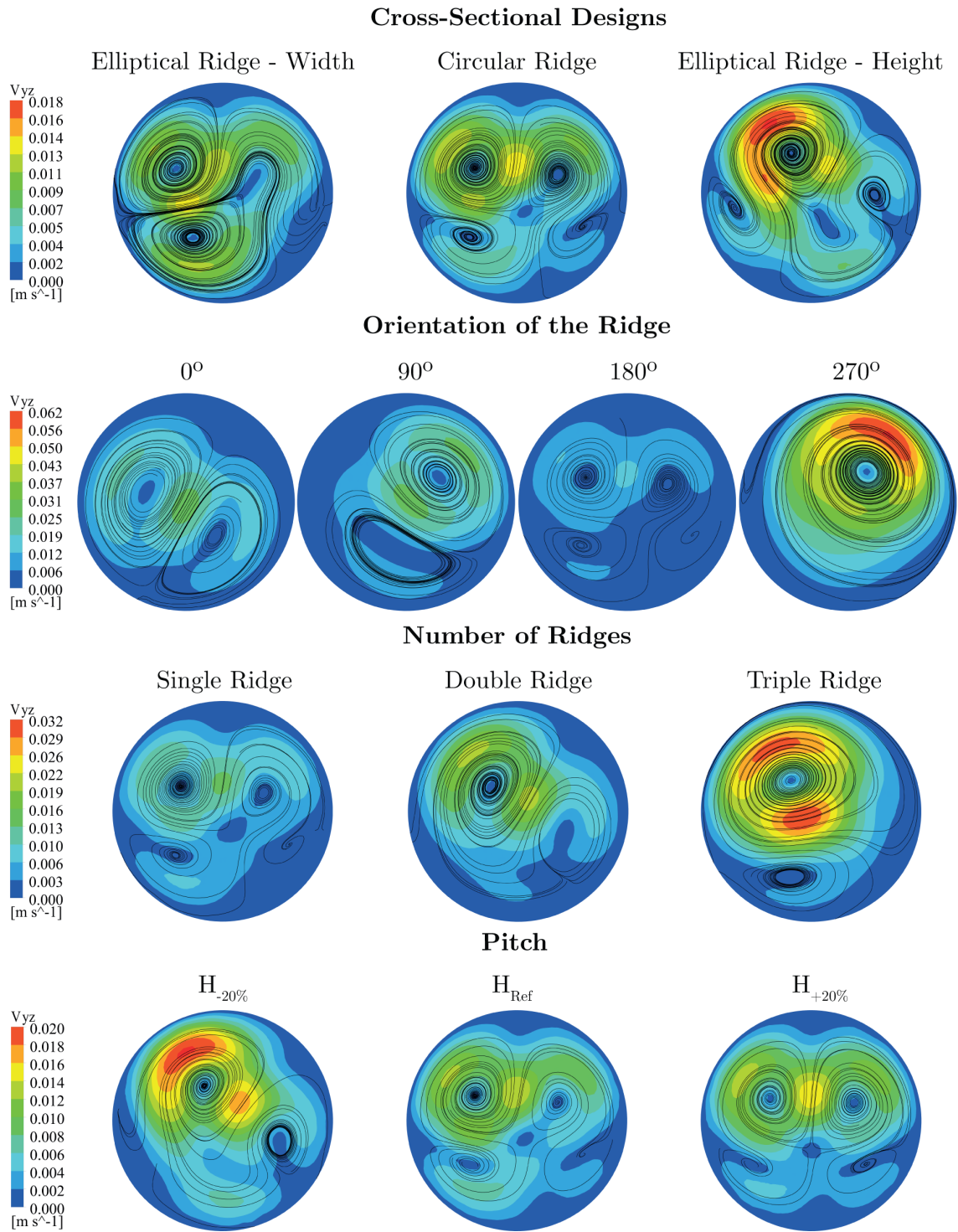
Figure 2.10: Contours of secondary velocity magnitude and crossflow streamlines for different ridge designs considered in design strategy B at monitoring plane 3.

Chapter 3

Eulerian Approach

3.1 Introduction

As was introduced in Chapter 1, the Eulerian flow description provides information of the fluid behaviour at every point of the fluid domain as a function of time. This traditional approach, that considers the blood as a continuous phase, will be used in this chapter to assess the influence of the different geometrical design parameters proposed in Chapter 2. In addition to the traditional WSS-based haemodynamic metrics (WSS, TAWSS, TAWSSG, OSI and RRT distributions), the rotational character of the flow field induced by the spiral ridge(s) will be assessed through the distributions of secondary velocity and helicity as well as the regions of recirculation and flow separation in the host artery. Despite of the lack of unanimity in the relationship between fluid dynamics parameters and physiological mechanisms of graft failure, widely accepted assumptions concerning the above-mentioned metrics will form the proposed improvement criteria. As a result, a preliminary enhanced configuration of spiral graft will be proposed and compared against the conventional designs of graft (no ridge) and spiral graft under pulsatile boundary conditions.

3.2 Numerical procedure

Building on the design strategy defined in Chapter 2, the different cross-sectional shapes, orientation, pitches and number of ridges, whose features are specified in Table 2.2 and illustrated in Figure 3.1, have been studied using the following numerical procedure.
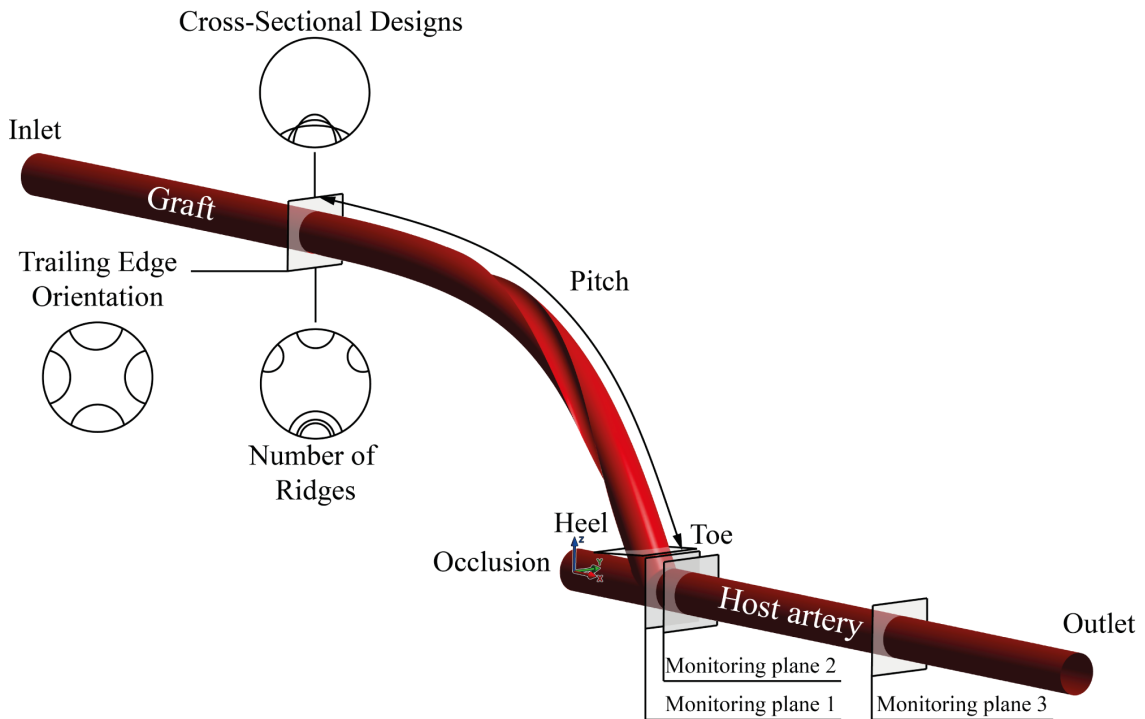
Figure 3.1: Schematic of the computational model.

3.2.1 Computational grid

The computational domain used in this chapter is based on finite-volume hybrid mesh consisting of prismatic elements for the near-wall and tetrahedral elements for the core regions and were generated using ANSYS Meshing (Version 17.1, Academic Research CFD license, ANSYS Inc., Canonsburg, USA). The number of elements

varies between 3.00-3.03 million, depending on the geometry simulated in each case, in order to limit the variation in velocity and wall shear stress to 1% with different mesh refinement levels, as shown in Figure 3.2. Skewness and orthogonal quality metrics were additionally checked to ensure the quality of the grids.
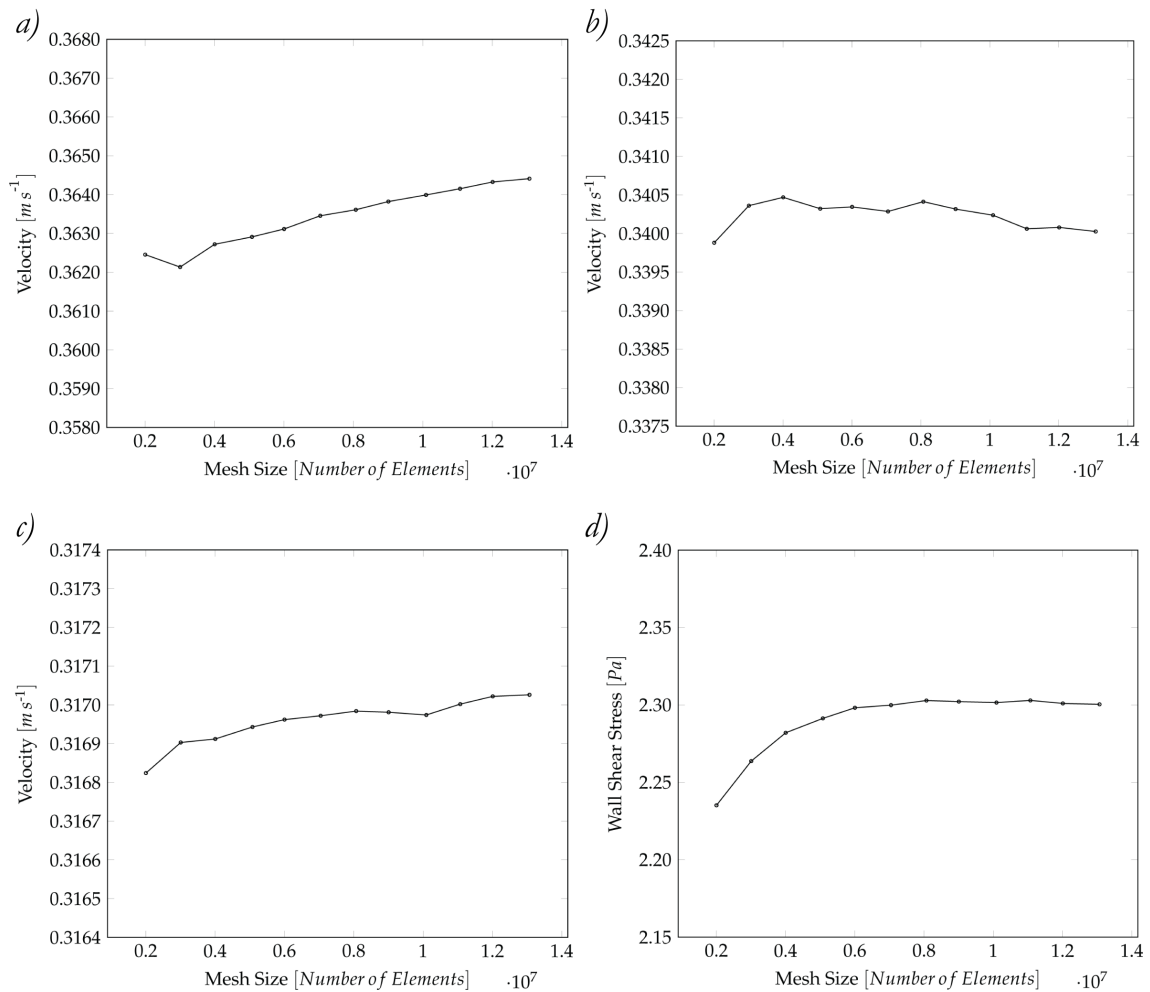
Figure 3.2: Area-weighted average values of velocity at monitoring planes a) 1, b) 2 and c) 3 and d) WSS in the host artery for different levels of mesh refinement.

3.2.2 Governing equations

The three-dimensional flow through the computational model is governed by the Navier-Stokes equations under the assumption of stationary flow.

Continuity equation,

$$\nabla \cdot \boldsymbol{u} = 0 \tag{3.1}$$

Momentum equations,

$$\nabla \cdot (\rho \boldsymbol{uu}) = -\nabla p + \nabla \cdot (\bar{\bar{\tau}}) \tag{3.2}$$

$$\bar{\bar{\tau}} = \mu[(\nabla \boldsymbol{u} + \nabla \boldsymbol{u^T}) - \frac{2}{3}\nabla \cdot \boldsymbol{u}\bar{\bar{I}}] \tag{3.3}$$

where ρ is the density of the blood, $\boldsymbol{u}$ is the velocity vector, p is the static pressure, $\bar{\bar{\tau}}$ is the stress tensor and μ is the dynamic viscosity. External body forces are neglected.

3.2.3 Non-Newtonian flow

Within the framework of the Eulerian description, the blood has been characterised as a homogeneous and incompressible fluid with a density of 1050 $kg\ m^{-3}$ [91, 92].

As described in Chapter 1, Section 1.5, due to the interest of this investigation on the study of secondary velocity and WSS-based haemodynamic parameters, among other metrics, in a fluid domain characterised by regions of low shear rates (bifurcations or anastomoses), the blood has been considered as a non-Newtonian fluid. The non-Newtonian behaviour of the blood has been implemented by means of the

Carreau-Yasuda model [93] that relates the dynamic viscosity, μ, as a function of the shear strain rate, $\dot{\gamma}$,

$$\mu = \mu_\infty + \frac{\mu_0 - \mu_\infty}{[1 + (\lambda\dot{\gamma})^\text{a}]^{\frac{1-n}{a}}} \tag{3.4}$$

where $\dot{\gamma}$ represents a scalar measure of the rate of deformation tensor, defined as

$$\dot{\gamma} = \sqrt{2tr(\bar{\bar{D}}^2)} \qquad\qquad \bar{\bar{D}} = [\nabla\boldsymbol{u} + (\nabla\boldsymbol{u})^{\boldsymbol{T}}]/2 \tag{3.5}$$

The low-shear viscosity, high-shear viscosity, time constant, Yasuda exponent, and power law index are taken to be $\mu_0 = 22 \cdot 10^{-3}$ Pa s, $\mu_\infty = 2.2 \cdot 10^{-3}$ Pa s, $\lambda = 0.11$ s, $a = 0.644$, and $n = 0.392$, respectively [94].

3.2.4 Boundary conditions

The configuration of boundary conditions was defined in terms of a constant and uniform velocity profile of 0.317 m s^{-1} ($Re = 570$) at the inlet and zero pressure at the outlet. The initial straight section of the graft, with an extension of 60 mm, enables the complete development of the velocity profile before approaching the leading edge of the ridge by reducing local inaccuracies at the inlet section [86]. The wall has been considered as rigid [18, 95] and a no-slip boundary condition has been applied to all wall boundaries.

The governing equations of the fluid dynamic problem were solved using a high resolution scheme in ANSYS CFX (Version 17.1, Academic Research CFD license, ANSYS Inc., Canonsburg, USA). The high resolution scheme models the advection term by providing a non-linear formulation that balances the accuracy and robustness of the solution according to the local gradients of the flow field [96, 97].

The convergence of solutions was simultaneously ensured by the global balance of the conservation equations and Root Mean Square (RMS) residual criteria. The conservation target and RMS criteria were set to 0.01 and 10^{-6}, respectively.

While most of the present simulations were conducted using steady-state conditions, a series of transient simulations were also conducted to obtain more advanced haemodynamics parameters (discussed further below). For transient simulations, an implicit second-order backward Euler method was used for the transient scheme with a time step of 0.01 s, according to previous investigations in this problem [83] and the available computational resources. The residual criterion to ensure the convergence of the numerical method was set to 10^{-6}. The results presented here were extracted from the last of four simulation periods in order to avoid initial instabilities of the numerical procedure [98].

3.3   Improvement criteria

Although it is widely accepted that haemodynamic parameters play an important role in the patency rate of graft anastomosis, there is no unanimity about the optimal flow pattern that improves the efficiency of the grafting [99]. Several authors have highlighted the benefits of high Wall Shear Stress (WSS) for avoiding the formation of plaque [100, 101], increase of intimal medial thickness [102] and proliferation of fibroatheroma and intermediate lesion [103]. In contrast, others suggest that high values of WSS may result in endothelial lesions [104]. This discrepancy gave rise to the theory of a safe bandwidth of WSS purposed by Kleinstreuer *et al.* [2, 105].

The paucity of *in vivo* data to support the existing hypotheses in the development of intimal hyperplasia and atherosclerosis in different bypass configurations are currently a major challenge [99]. The lack of quantitative thresholds of haemody-

namic metrics associated with physiological mechanisms of graft failure entails the use of qualitative design criteria and makes it difficult to find haemodynamically 'optimum' configurations.

Nevertheless, the swirling flow is considered to be a beneficial physiological mechanism to reduce abnormal flow conditions [106] in order to prevent thrombosis, intimal hyperplasia and atherosclerotic lesions [5, 107, 108] (i.e. the main causes of graft failure). Consequently, consistent with Kabinejadian *et al.* [83], the haemodynamic 'optimisation criteria' of the spiral-inducing graft in the present study will be based on the assumptions of high wall shear stress, high secondary velocity and reduction of separation and recirculation zones, as potential favourable haemodynamic factors.

3.4   Validation

This numerical procedure was validated in [109] using a series of steady-state simulations for a spiral-inducing graft configuration which have been tested experimentally by Kokkalis *et al.* [5]. In their experiments, the secondary flow motions induced by the Spiral Laminar Flow Peripheral Vascular Graft (Vascular Flow Technologies Ltd., Dundee, UK) were compared with those of a control device; constant flow rates were applied and data was collected in the cross-sectional view distal from the graft outflow and dual-beam vector Doppler was used to create 2-D velocity maps.

In the validation tests, the secondary velocity magnitude (normalised with the theoretical axial velocity produced by the mean flow rate) obtained from this simulation procedure was compared against the measurements of Kokkalis *et al.* at monitoring plane 2, 5 mm distal from the toe of the anastomosis, under a Reynolds number of $Re = 1140$ in this case. The maximum normalised secondary velocity was also compared under different flow rates at monitoring plane 3 (see Figure 3.3). As

can be observed in [109], the numerical results were in good qualitative agreement with the data, especially in identifying the spiral flow in the host artery and areas with the maximum velocity magnitude. Inherent differences may be due to unknow geometrical details of the experimental model such as a potential out-of-plane geometry, characteristics of the connection between graft and vessel as well as the effect of the elastic behaviour of gratf and vessel particularly with the increase of the Reynolds number.
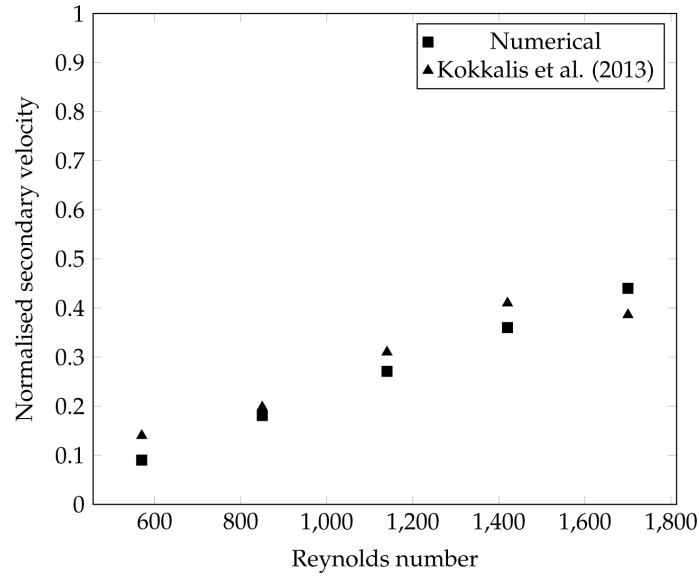
Figure 3.3: Comparison of maximum normalised secondary velocity magnitudes under different flow rates at monitoring plane 3 obtained from the present simulation procedure against measurements of Kokkalis *et al.* [5].

3.5 Results

3.5.1 Secondary Velocity

The swirling motion has been characterised through the secondary velocity contours and crossflow streamlines at the monitoring planes 1, 2, and 3 located at $1\,mm$, $5\,mm$

and 50 mm distal from the toe of the anastomosis, respectively. The secondary velocity was defined as the composition of the transverse velocities v and w along the Y and Z axes in the host artery, respectively,

$$v_{yz} = \sqrt{v^2 + w^2} \tag{3.6}$$

The average values of such distributions at the different monitoring planes are given in Table 3.1. Note that the direction of the flow in all secondary velocity distributions should be interpreted as into the page.

Figure 3.4 shows that while no significant changes can be seen at monitoring plane 1 for the different cross-sectional designs of the ridge, different patterns can be observed from monitoring plane 2 where the intensity of asymmetry increases downstream and the peak secondary velocity regions rotates around the axis of the host artery moving to the lateral side of the lumen. The differences in secondary velocity magnitude are more noticeable reaching an improvement of 15% with the increase of the height from the reference case. The higher secondary velocity magnitudes are associated with the dominant vortex. At monitoring plane 3, the increase of the height of the elliptical ridge results in a relevant improvement of 19% in average secondary velocity magnitude with respect to the circular configuration.

The helical flow generated by different orientations of the ridge is presented in Figure 3.5, where a number of prominent flow features are worth highlighting. At monitoring plane 1, all orientations show the maximum secondary velocity located around the centre of the lumen. Moving further away from the anastomosis in the streamwise direction, the secondary velocity peak region develops an important asymmetry and moves to a lateral side of the host artery, depending on the ridge orientation. At monitoring plane 3, the trailing edge orientation 270° stands out
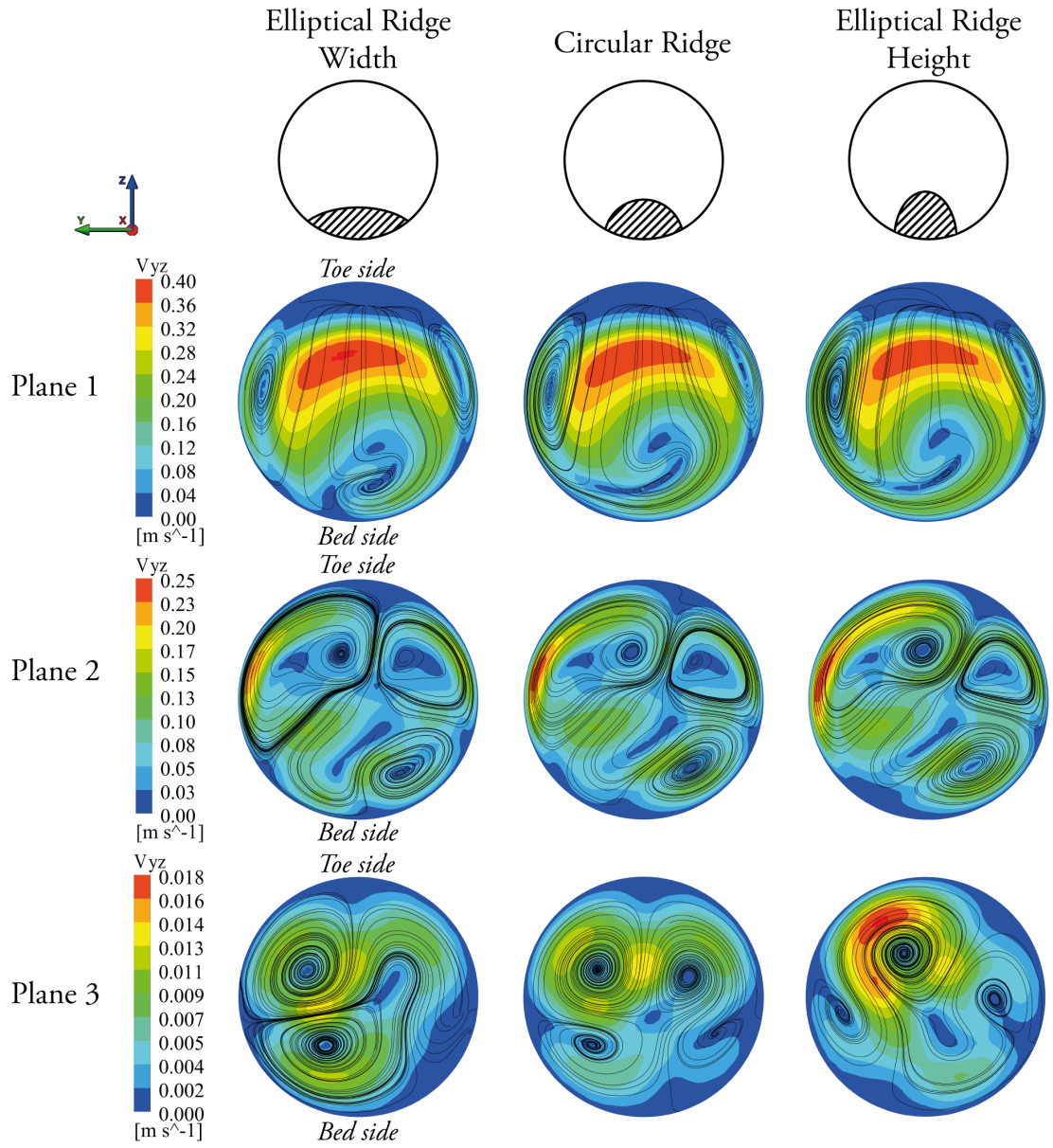
Figure 3.4: Secondary velocity distributions and crossflow streamlines for different cross-sectional designs of a single ridge.

amongst the other configurations by reaching the highest secondary velocity and producing a single dominant spiral as a result of dissipation of the weaker vortices.

Although one would assume that the trailing edge orientations 90° and 270° should produce similar distributions in the present case, the results highlight sig-
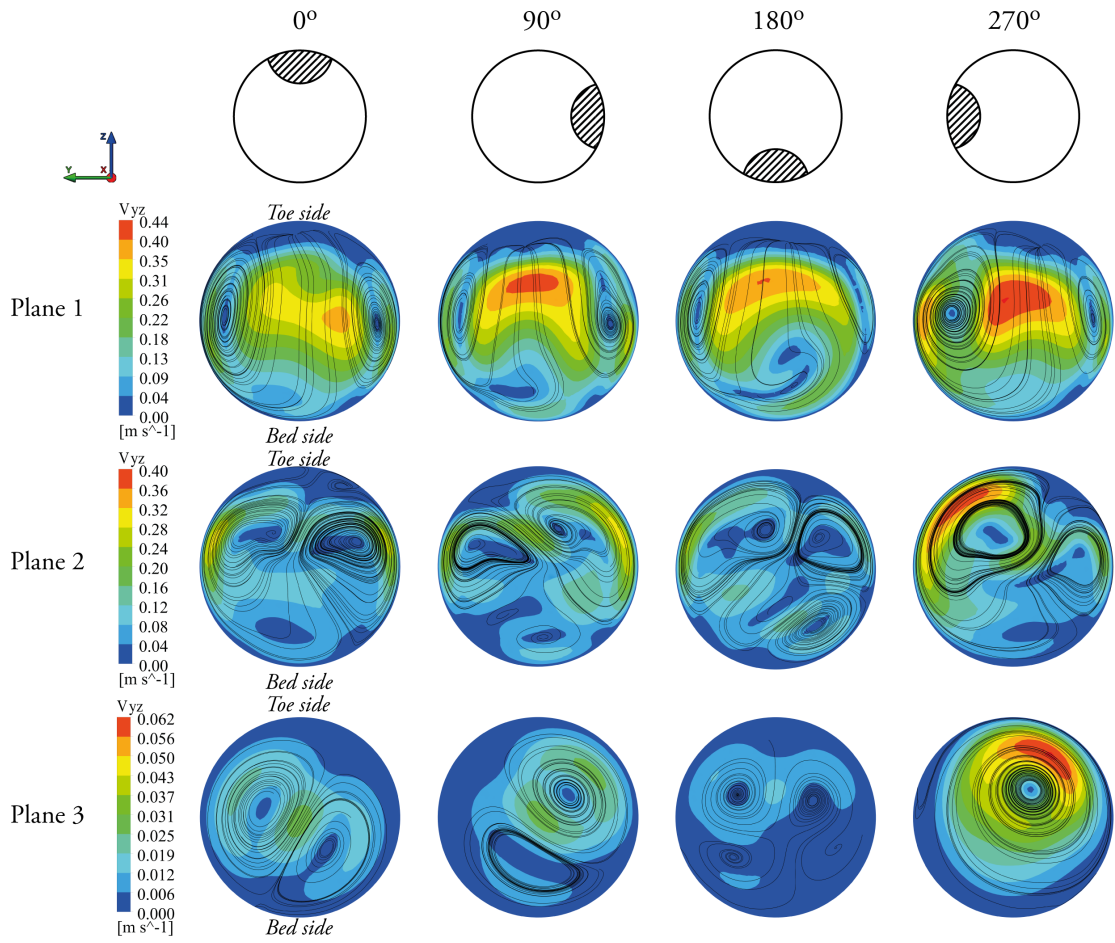
Figure 3.5: Secondary velocity distributions and crossflow streamlines for different orientation of the trailing edge.

nificant differences, mainly due to the spiral direction along the pitch. Since the secondary flow in the distal section of the graft is clockwise, in the case of trailing edge orientation 90°, the induced rotation by the ridge is supressed by the near side-wall effect in the host artery upon impingement on the arterial bed, as illustrated in Figure 3.6. However, in the case of trailing edge orientation 270°, the swirling flow receives lesser degree of suppression from the surrounding wall boundaries. This phenomenon could also be observed at plane 3 where the average secondary veloc-ity magnitude in the 270° model is over 4 times higher than that produced by the

reference case (180°), as shown in Table 3.1. Although each model shows a different secondary velocity distribution, the 180° and 270° orientations show the weakest and strongest average secondary velocity magnitudes, respectively, at all monitoring planes.
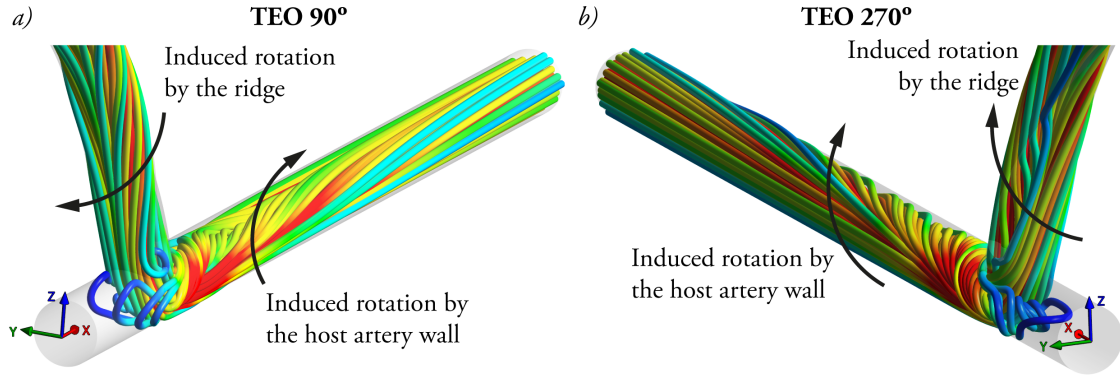
Figure 3.6: Streamlines and representation of the rotation induced by a single ridge with trailing edge orientations 90° and 270°, and those produced by the curvature of the arterial wall.

The effects of increasing the number of ridges are shown in Figure 3.7. At monitoring planes 1 and 2, the double ridge design results in a decrease of secondary velocity compared to the single ridge configuration. However, at monitoring plane 3 this pattern changes and the double ridge configuration produces 37% higher average secondary velocity magnitude in comparison with the reference case. The triple ridge design with three equally-spaced ridges at 60°, 180° and 300° leads to an even more significant increase of secondary velocity magnitude and shows the implicit effect of the trailing edge orientation through the ridges located at the orientations 60° and 300°.

The influence of the pitch is illustrated in Figure 3.8. Closer to the anastomotic region, changing the helical pitch has negligible effects on the magnitudes and distributions of the secondary velocity. However, further downstream in the host artery, a

46
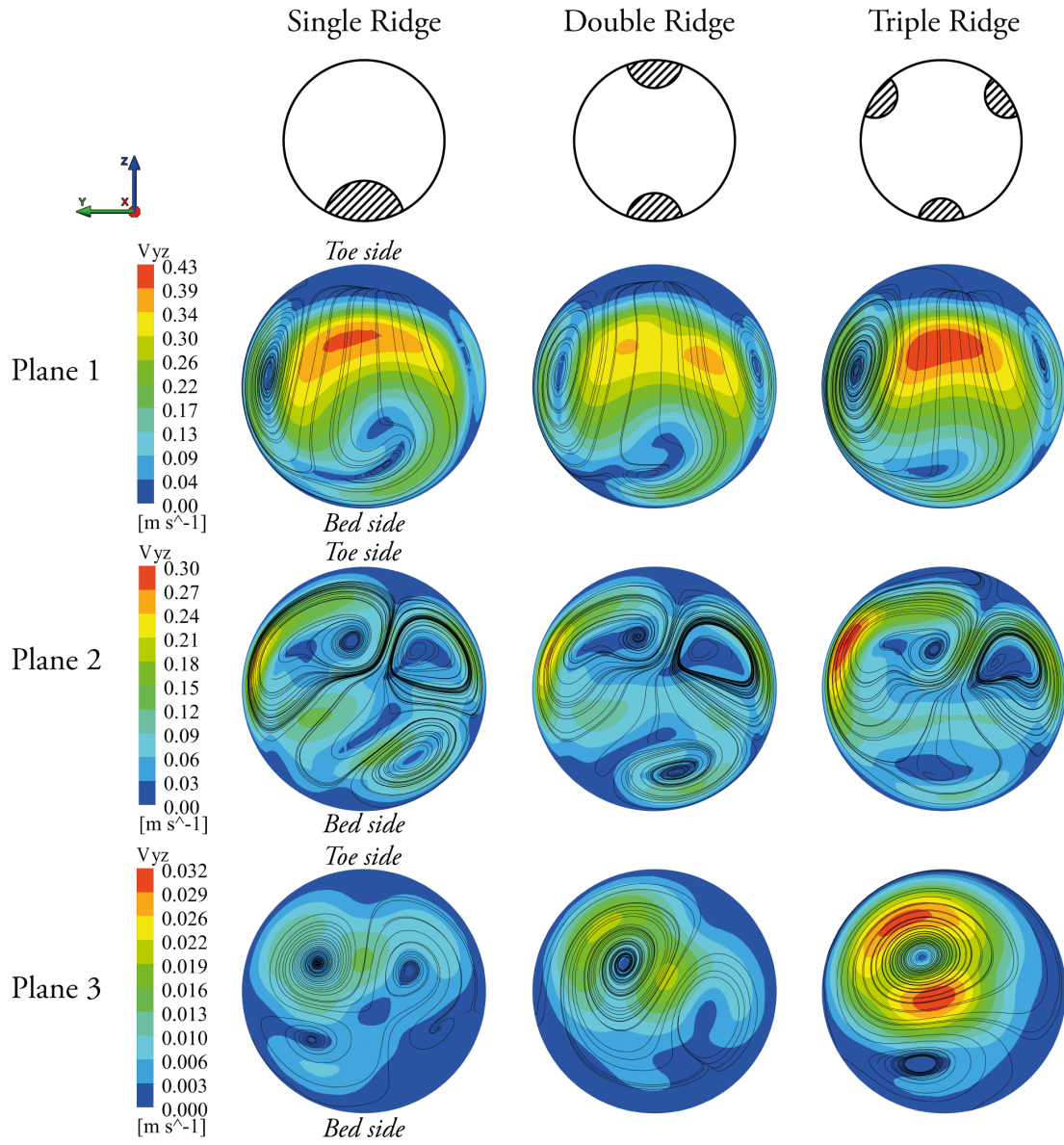
Figure 3.7: Secondary velocity distributions and crossflow streamlines for different numbers of ridges.

noteworthy increase of approximately 30% in secondary velocity magnitude is found at monitoring plane 3 by decreasing the pitch.
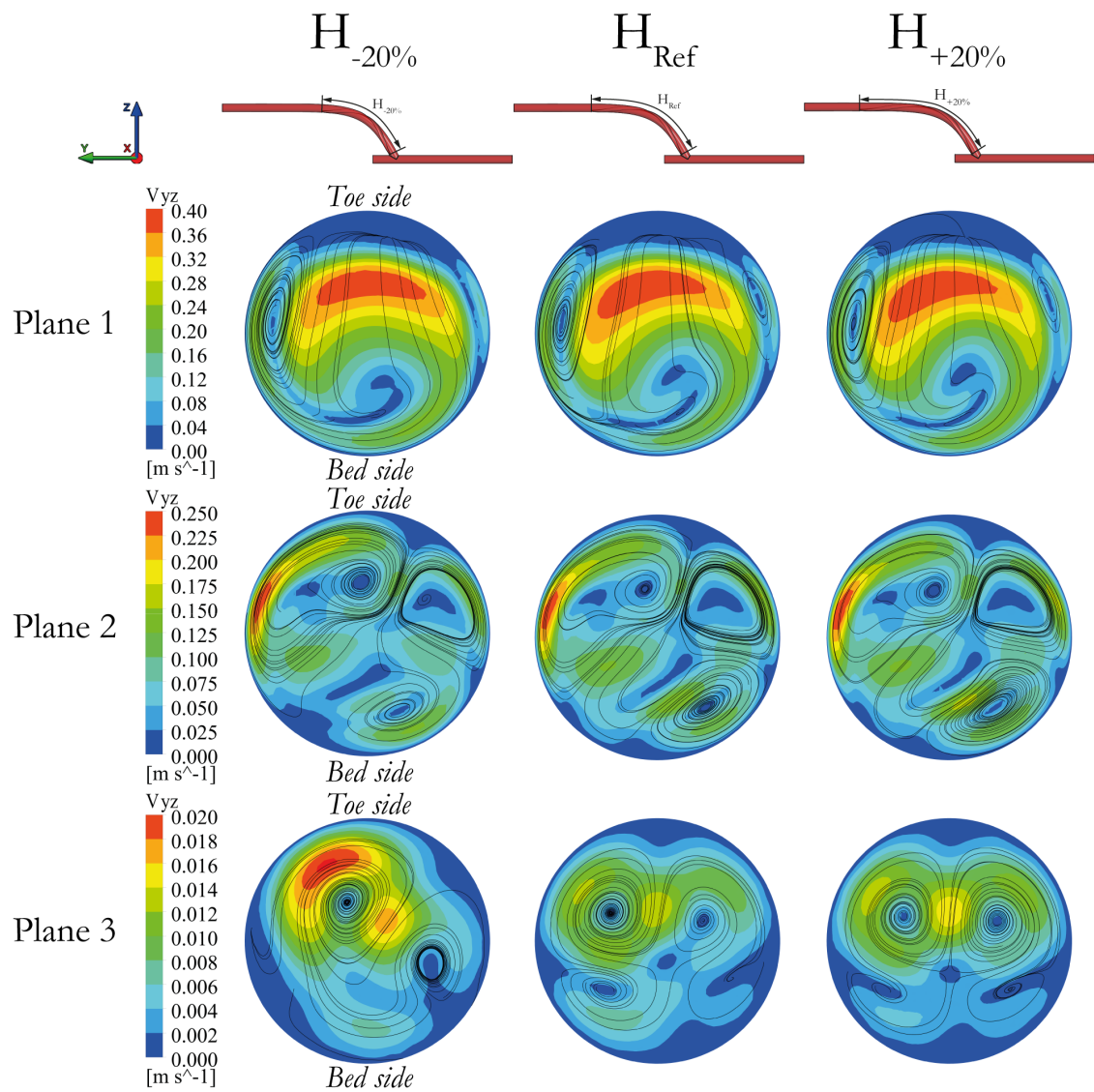
Figure 3.8: Secondary velocity distributions and crossflow streamlines for different ridge pitches.

Table 3.1: Average secondary velocity magnitude at the different monitoring planes along the host artery.

		v_{yz} [$m\ s^{-1}$]·10^{-2} Monitoring plane 1	v_{yz} [$m\ s^{-1}$]·10^{-2} Monitoring plane 2	v_{yz} [$m\ s^{-1}$]·10^{-2} Monitoring plane 3
Cross-sectional designs	Elliptical - Height	17.02	8.14	0.59
	Circular	16.43	7.10	0.50
	Elliptical - Width	16.08	6.64	0.54
Trailing edge orientation	0°	16.81	7.89	0.94
	90°	17.22	9.21	0.96
	180°	16.43	7.10	0.50
	270°	19.21	11.92	2.20
Number of ridges	Single	16.43	7.10	0.50
	Double	15.94	6.61	0.69
	Triple	17.18	7.86	1.15
Pitch	$H_{+20\%}$	16.70	7.35	0.52
	H_{Ref}	16.43	7.10	0.50
	$H_{-20\%}$	16.48	7.05	0.65

3.5.2 Helicity

In the present work, the helicity is measured through calculating the 'helicity density' defined as the dot product of vorticity (i.e. curl of the velocity vector) and velocity [4, 110],

$$h = (\nabla \times \boldsymbol{v}) \cdot \boldsymbol{v} \tag{3.7}$$

The distributions of absolute area-weighted average of helicity density along the host artery are shown in Figure 3.9. The integral of such distributions provides the values of helicity listed in Table 3.2.

In line with the above results of secondary velocity, as can be observed in Figure 3.9a, the case of 'Elliptical Ridge - Height' ($L_1/D = 0.3$) generates the highest distribution of helicity density. This effect is more noticeable within the anastomotic region where it can be seen that the peak helicity density is proportional to ridge

height. Moving further away in the streamwise direction, the differences in helicity density decrease with a slight predominance of the elliptical configurations.

The effects of varying the orientation of the ridge in the distribution of helicity are shown in Figure 3.9b, where consistent with the observations from Figure 3.5, the trailing edge orientation 270° produces the highest distribution of helicity density along the host artery. The 0° orientation shows a somewhat significant drop in helicity compared to the reference case (i.e., 180°) in the region of flow impingement onto the bed of the host artery (i.e., $x = 25 - 53\ mm$). In other regions of the host artery, the comparative performance of different configurations is similar to that at the anastomosis.

Figure 3.9c illustrates the distributions of helicity density for different number of ridges. It can be seen that the single and triple ridge configurations show the highest values of helicity density in the anastomosis region. The multiple ridge configurations fall below the case of single ridge in the region where the flow impinges on the bed of the host artery. However, the triple and double ridge configurations show higher helicity density than the reference case beyond $x = 50$ and $65\ mm$, respectively.

The distributions of helicity density due to the variation of the ridge pitch are shown in Figure 3.9d. In terms of helicity, the increase of the helical pitch enhances the swirling flow in the anastomosis region and produces a rise in helicity density. Similarly as observed before in terms of secondary velocity, in the region away from the anastomosis, specifically from $x = 65\ mm$, the decrease of the ridge pitch slightly increases the magnitude of helicity density.
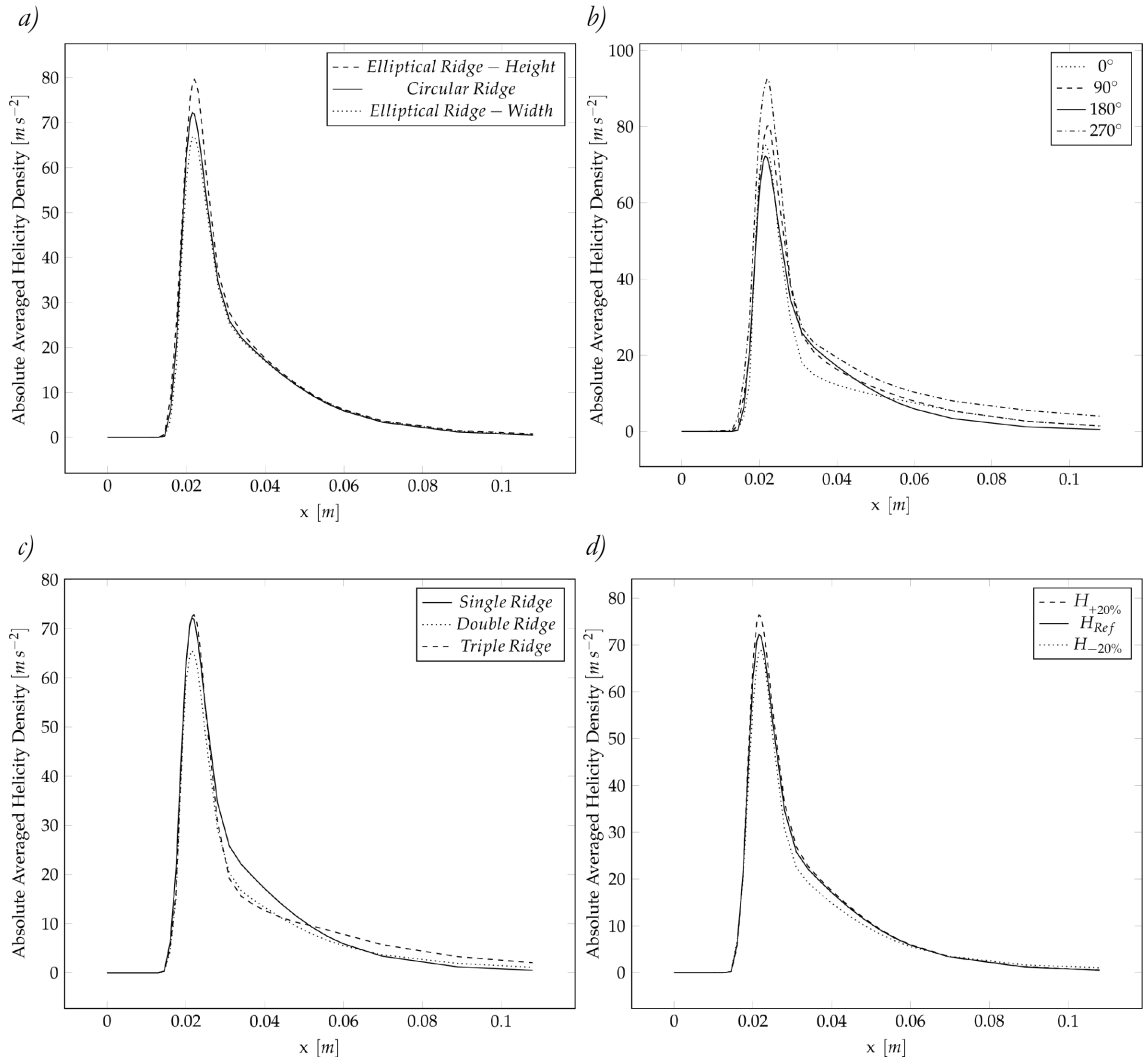
Figure 3.9: Distributions of helicity density along the host artery. Solid lines represent the reference case in each figure.

3.5.3 Wall Shear Stress

The WSS characterises the tangential fluid forces that act on the vessel wall. As was alluded to earlier, the intimal thickening and restenosis due to intimal hyperplasia is normally characterised by low WSS [100–103]. In addition to intimal hyperplasia, one should also consider the effects of mural platelet and fibrin deposits in the artery; the deposition of a mural layer of proteins and/or cells that can be the nidus

Table 3.2: Pressure drop in the fluid domain, absolute helicity and spatial mean of wall shear stress in the host artery.

		Pressure Drop [Pa]	Helicity $[m^2 s^{-2}]$	Wall Shear Stress [Pa]
Cross-sectional designs	Elliptical - Height	565.341	1.277	2.307
	Circular	550.341	1.182	2.295
	Elliptical - Width	535.490	1.142	2.290
Trailing edge orientation	0°	531.130	1.140	2.283
	90°	543.054	1.333	2.374
	180°	550.341	1.182	2.295
	270°	545.863	1.660	2.432
Number of ridges	Single	550.341	1.182	2.295
	Double	546.291	1.045	2.276
	Triple	547.317	1.183	2.256
Pitch	$H_{+20\%}$	559.310	1.225	2.310
	H_{ref}	550.341	1.182	2.295
	$H_{-20\%}$	537.986	1.103	2.281

for further cell and protein infiltration and atherosclerotic lesion progression, could subsequently result in graft failure. From the haemodynamic point of view, fibrinogen/fibrin is normally deposited at low shear rates and at areas exposed to eddies, flow separations and stasis (i.e. after stenosis and after areas of flow disturbance), thus, making the WSS metric even more relevant in the present study [83].

Figure 3.10 represents the distributions of WSS on an unfolded model of the host artery, which has been opened ventrally and the direction of the flow is from left to right. The spatial means of such distributions are given in Table 3.2.

The increase of the ridge height generates an increase of WSS on the bed in magnitude and asymmetry, slightly shifting the peak regions to the lateral side of the host artery.

The trailing edge orientation again represents an important parameter since the most homogeneous distribution and the highest average WSS are obtained by the 270° configuration; this trailing edge orientation also results in the high-shear region further extending proximally towards the occluded section of the host artery. Moreover, in agreement with the results presented in Figure 3.5 and Figure 3.9b, the 90° configuration also results in higher average WSS magnitude compared to 0° and 180° configurations.

The increase of the number of ridges results in consecutive and slight decrease of the spatial mean WSS, while the degree of asymmetry in the distributions tend to increase with respect to the reference case. The decrease in the WSS for the triple ridge design here is particularly interesting, since in Figure 3.7 it was shown that in fact the triple ridge design leads to an increase of secondary velocity magnitude at all monitoring planes. This observation highlights the importance of assessing the performance of such haemodynamics problems using a range of different metrics. Therefore, relying on a single parameter could lead to inconclusive outcomes.

The variation of the ridge pitch results in minor effects on the spatial mean of WSS in the host artery, returning differences less than 1% as shown in Table 3.2.

3.5.4   Flow separation and recirculation

Abnormal flow conditions and recirculation are associated to regions of low WSS that lead to cholesterol deposition, atheroma growth thrombus formation and, eventually, IH development [2]. Therefore, the focus of this section is on the recirculation and retrograde flow regions.

Figure 3.11 represents the regions of retrograde flow (negative axial velocity) generated by different graft designs at monitoring planes 1 and 2 located at 1 mm
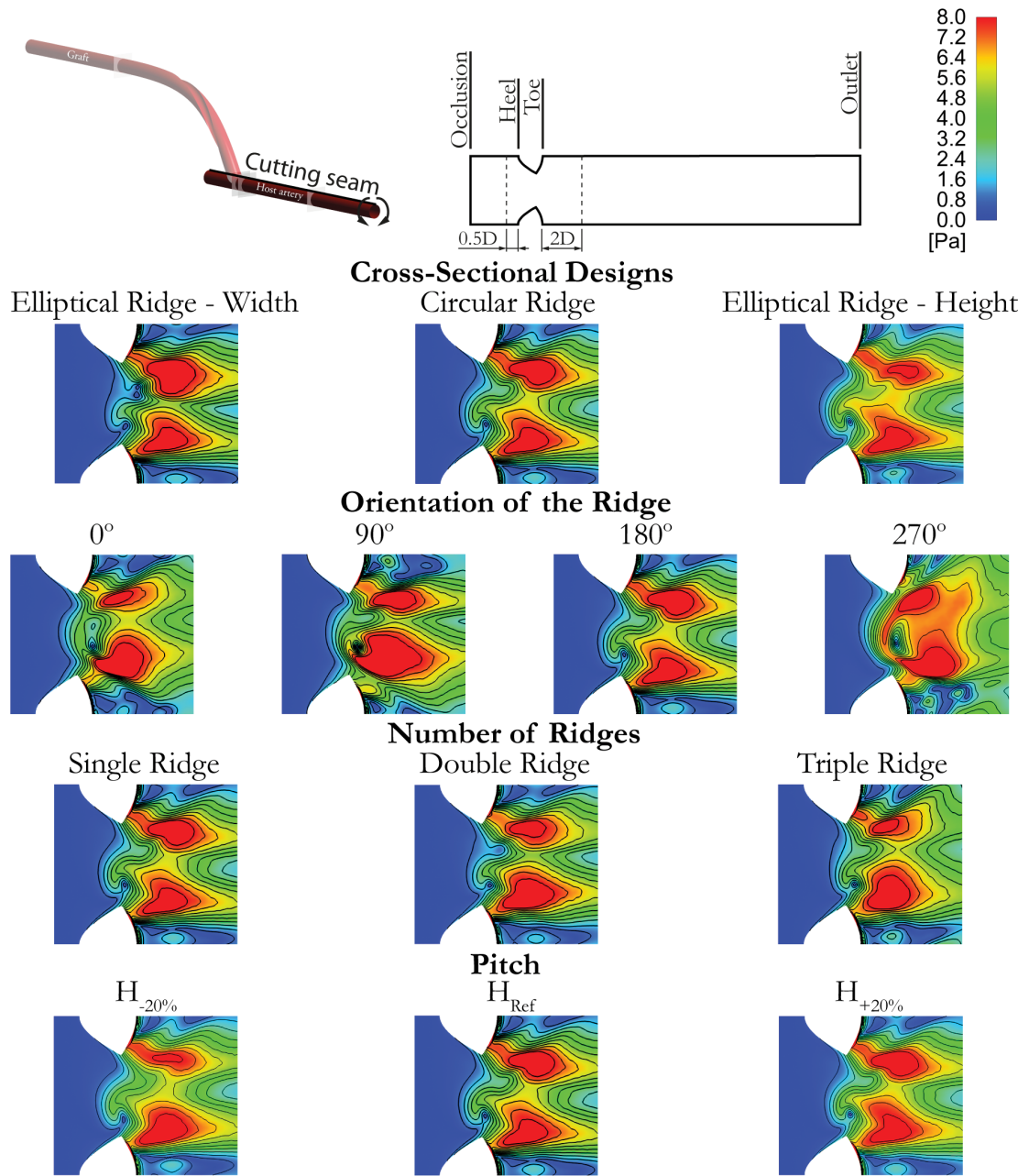
Figure 3.10: Wall Shear Stress distributions on an unfolded model of the host artery for different ridge designs.

and 5 *mm* distal from the toe of the anastomosis, respectively. These regions were insignificant at plane 3, hence not included in Figure 3.11. The direction of the flow

should be interpreted as into the page. The percentage of cross-sectional area of the host artery affected by this adverse effect is given in Table 3.3.

In all cases, the recirculation zones are found at the toe side of the host artery close to the anastomosis. At monitoring plane 1, except for the trailing edge orientation, the other three design parameters present minor effects on the flow separation zones with the maximum 1.2% difference compared to the reference case. The variation of the ridge trailing edge orientation with respect to the reference case, however, results in a slight decrease of the flow separation zone but an increase in the degree of asymmetry in these regions.

Distinct recirculation zones are found at monitoring plane 2, most of which can be seen to extend towards the centre of the lumen and to rotate due to the spiral motion of the graft outlet flow impinging onto the host arterial bed. The increase of the ridge height and width tend to decrease (3.4%) and increase (1.4%) the recirculation region, respectively. The variation of the trailing edge position with respect to the reference model results in significant reduction in both retrograde flow area (e.g. 8.6% for trailing edge orientation 270°) and the extent of recirculation region towards the centre of the lumen. Another interesting point to highlight here is how the recirculation regions of the orientations 270° and 90° rotate clockwise and anticlockwise, respectively, around the axis of the host artery. This can be explained again by considering the interaction between the induced rotations by the ridge and surrounding wall boundaries.

Increasing the number of ridges within the graft leads to reduction of the disturbed zones. In particular, the results of the triple ridge design are of significant interest here, where 7.4% reduction is achieved.

Finally, similar to the results obtained in terms of WSS, the modification of the pitch leads to insignificant effects on the variation of recirculation regions.
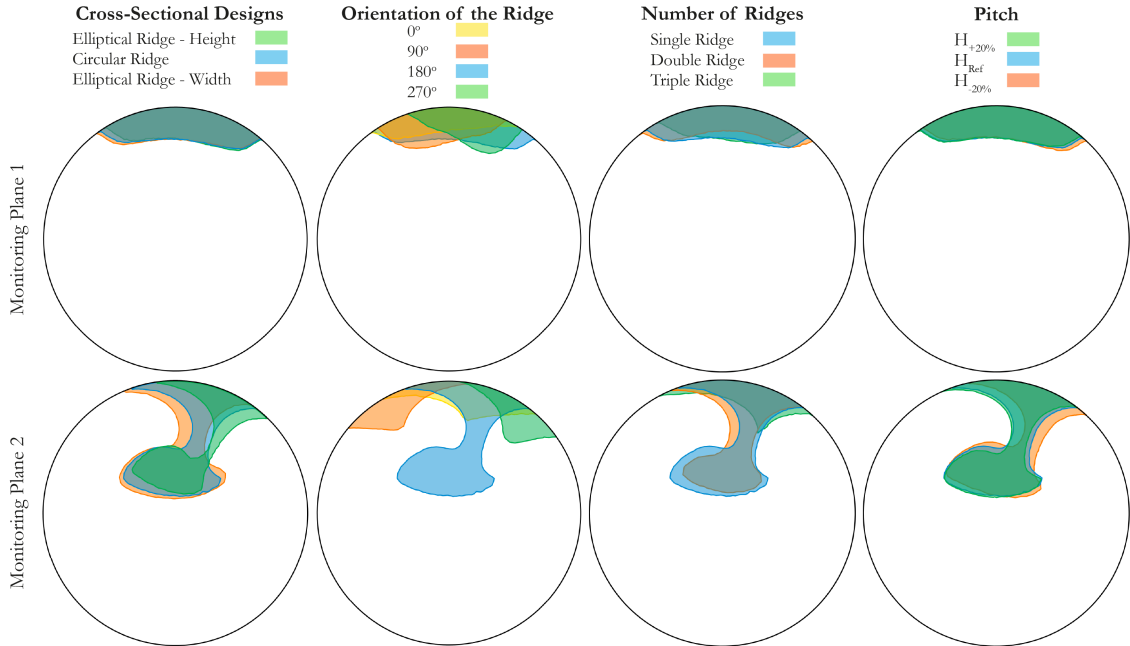
Figure 3.11: Regions of retrograde flow with different designs at monitoring planes 1 and 2. These regions are negligible in plane 3, hence not included here.

3.6 Discussion

Building on the important role of the haemodynamic parameters and the recognised sensitivity of the flow pattern to the geometry [34, 83, 111, 112], the present chapter has assessed different designs of a peripheral prosthetic graft with internal spiral ridge(s) using the Eulerian formulation of fluid mechanics. This description represents the traditional computational approach for the analysis of haemodynamics by considering the blood as a homogeneous fluid.

The design condition of constant total cross-sectional area adopted in Chapter 2 results in the same level of resistance against the flow and consequence pressure

Table 3.3: Percentage of cross-sectional area affected by recirculation at the different monitoring planes along the host artery.

		Monitoring Plane 1	Monitoring Plane 2	Monitoring Plane 3
Cross-sectional designs	Elliptical - Height	7.38%	8.71%	0%
	Circular	7.63%	12.07%	0%
	Elliptical - Width	7.78%	13.51%	0%
Trailing edge orientation	0°	4.59%	5.03%	0%
	90°	6.25%	3.82%	0%
	180°	7.63%	12.07%	0%
	270°	5.31%	3.52%	0%
Number of ridges	Single	7.63%	12.07%	0%
	Double	6.70%	10.83%	0%
	Triple	6.40%	4.71%	0%
Pitch	$H_{+20\%}$	7.47%	11.35%	0%
	H_{Ref}	7.63%	12.07%	0%
	$H_{-20\%}$	7.56%	11.76%	0%

drop, enabling the appropriate comparison of different configurations. Based on the widely accepted assumptions postulated in Section 3.3, the flow patterns have been studied in order to increase the swirling flow and wall shear stress as well as reducing flow separation and recirculation zones.

Figure 3.13 summarises the effects of different ridge designs on all the design parameters tested here, namely average secondary velocity magnitude, area affected by retrograde flow, pressure drop, helicity and spatial mean of WSS. The results have been normalised with the corresponding values of the reference configuration.

Based on Figure 3.13a, an improvement in the performance of the graft could be achieved through the variation of the height of an elliptical ridge. The increase of the ridge height has resulted in an enhancement of the swirling flow (with higher values of secondary velocity and helicity), a reduction of the recirculation zones and a slight increase in the spatial mean WSS.

In the present study, the location of the spiral ridge trailing edge at the anastomosis has been shown to be the most important design parameter in order to

improve the performance of the graft. As shown in Figure 3.13b, significant differences in the spiral flow patterns and the regions of flow separation have been observed amongst the four trailing edge orientations tested here. In a lower order of magnitude, the variation of the ridge orientation also results in the most noteworthy difference in spatial mean of WSS in the host artery when compared with the other design parameters. Increases in WSS of 3.44% and 5.97% were reported with orientations 90° and 270°, respectively. The most significant effect of the trailing edge orientation was observed at the interaction between the induced rotation and the ridge and the suppression produced by the near sidewall of the host artery upon impingement. Consequently, in the case of the trailing edge orientation 270°, the intensity of the swirling flow is effectively enhanced greater than the other configurations due to the lesser degree of suppression from the surrounding boundaries, when passing through the anastomosis.

Most of the results presented in this chapter including Figure 3.13c suggest that increasing the number of ridges in the graft could have measurable effects, especially on the secondary velocity magnitude and retrograde flow. However, the impact of varying the number of ridges is more influenced by the location of the ridge trailing edge(s) as opposed to the number of ridges. To further prove this fact, an additional study of the double ridge configuration was conducted using orientations 90° and 270° in comparison with the above-mentioned double ridge case where the ridges have orientations 0° and 180°. As can be observed in Figure 3.12, the new configuration returns higher secondary velocity, revealing the influence of the orientation over the number of ridges which supports the above hypothesis.

Figure 3.13d denotes a measurable improvement in terms of the secondary velocity magnitude in the region of the host artery away from the anastomosis by

	Double Ridge	
a)	$0°, 180°$	$90°, 270°$
V_{yz} [$m\,s^{-1}$]·10^{-3}, Plane 3	6.87	14.42

b)
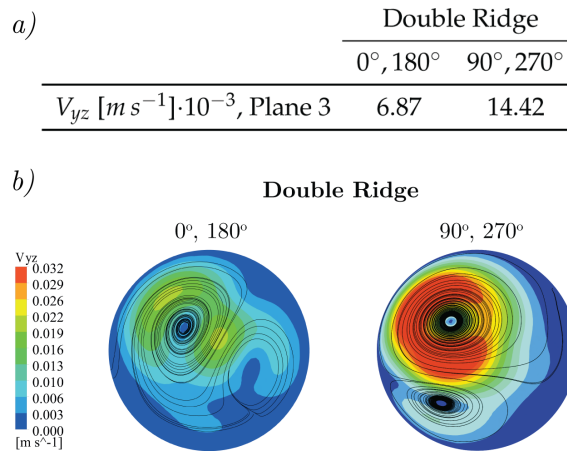
Double Ridge

Figure 3.12: Justification of the greater influence of the ridge orientation over the number of ridges on the secondary flow by comparing double ridge configurations with trailing edge orientations 0° and 180° against 90° and 270°.

decreasing the helical pitch. However, other results reported throughout this study suggest that the variation of the pitch tends to have minor influences on the region of the anastomosis.

3.6.1 Clinical relevance: Novel strategy for peripheral bypass surgery

The above observation about the different performances of spiral grafts depending on the orientation of the ridge has an important implication on the peripheral artery bypass surgeries, since the rotation of the blood flow has been found as clockwise in the left common iliac arteries and anticlockwise in the right common iliac arteries using magnetic resonance angiography [28, 30, 106]. Although the current design of SLF grafts incorporate the internal ridge with 180° orientation, the present findings could lead to a more effective peripheral bypass surgery strategy by considering two grafts with optimised ridge orientation and with opposite ridge rotational direction (i.e. clockwise and anticlockwise) in order to achieve the improved and physiologi-
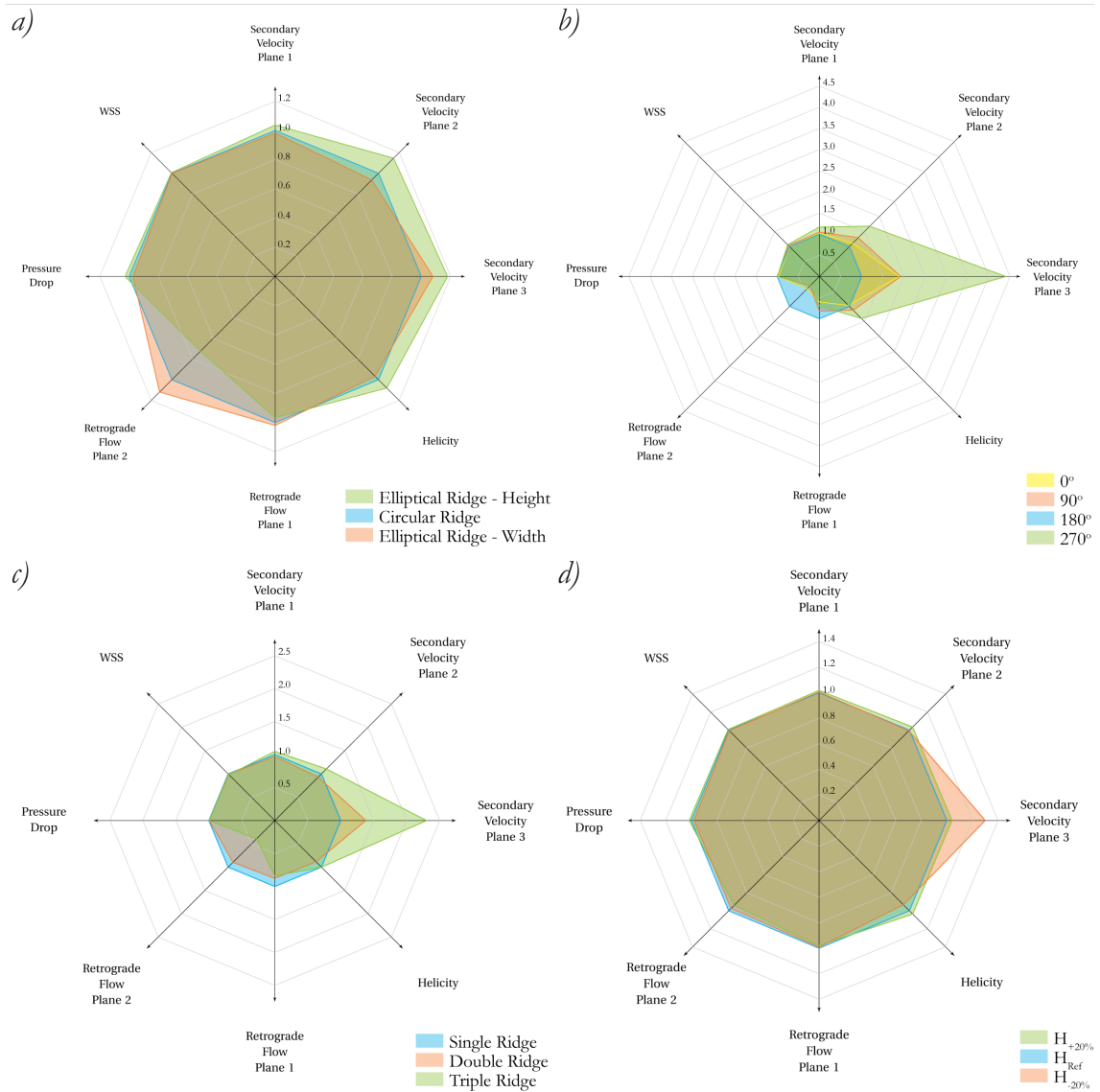
Figure 3.13: Overall comparison of normalised results for different ridge designs.

cally suitable rotation of the blood flow depending on the location of the stenosis, as shown in Figure 3.14.
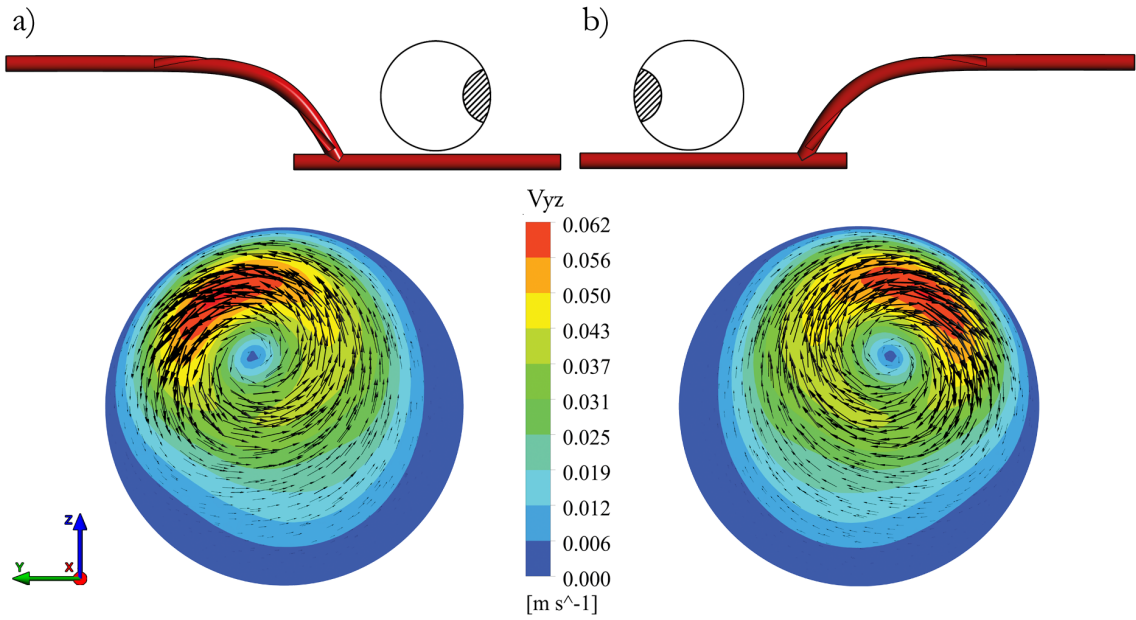
Figure 3.14: Contours of secondary velocity and velocity vector distributions of preliminary optimised a) anticlockwise configuration with trailing edge orientation 90° and b) clockwise configuration with trailing edge orientation 270°.

3.6.2 Comparative study between conventional, spiral and enhanced spiral grafts under transient boundary conditions

Based on the results presented earlier, an enhanced design of spiral graft is proposed for its comparison against the conventional graft (no ridge) and spiral graft (configuration with single circular ridge and trailing edge orientation 180°). The new enhanced spiral graft is developed according the most significant design parameters, i.e. single elliptical ridge ($L_1/D = 0.3$) and orientation of the trailing edge 270°.

The comparative analysis between conventional, spiral and enhanced spiral grafts has been carried out under transient boundary conditions using the inlet velocity waveform represented in Figure 3.15a that corresponds to MRI measurements in

femoral artery of a healthy subject [113] (details of the transient simulation can be found in Section 3.2).

a)

b)
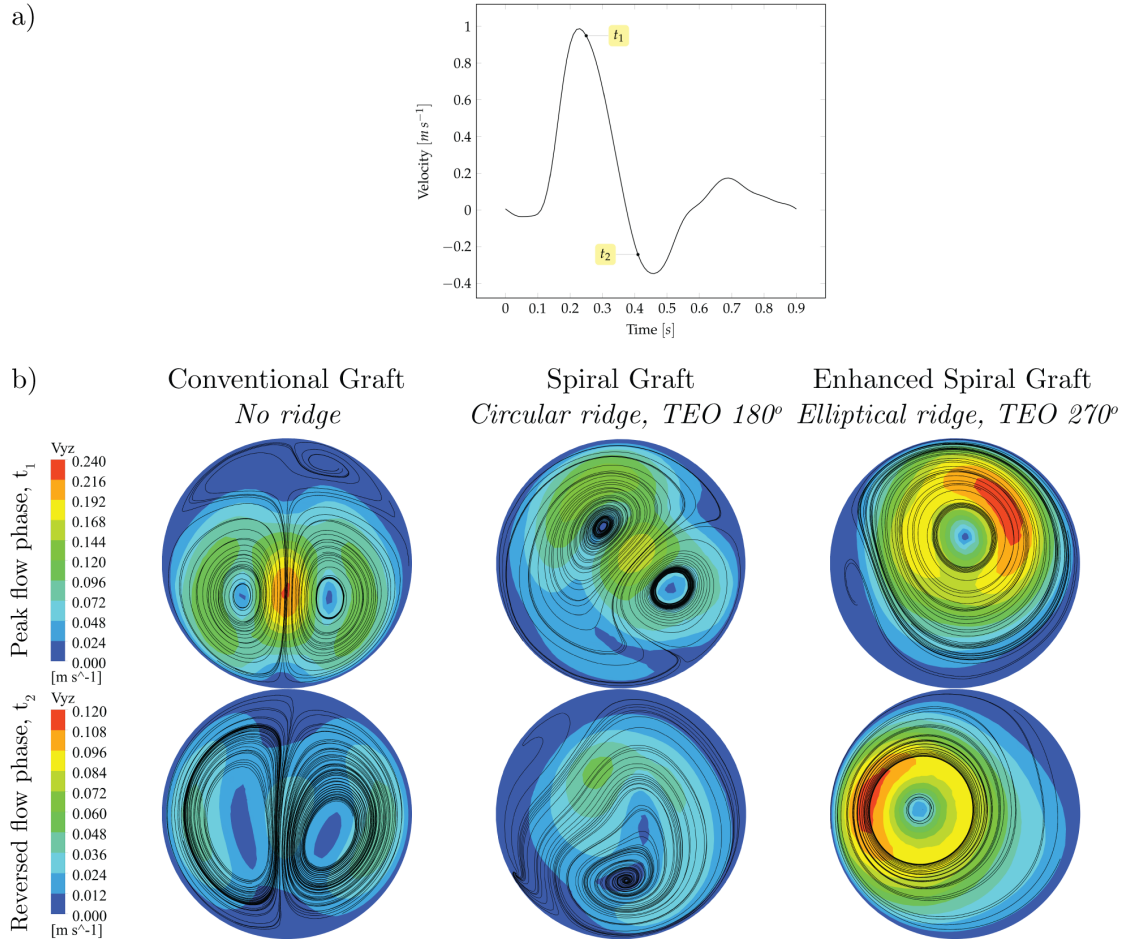
Figure 3.15: (a) Velocity waveform at the inlet and (b) contours of secondary velocity and crossflow streamlines at monitoring plane 3 and at peak (t_1) and reversed (t_2) flow phases.

Figure 3.15b shows the contours of secondary velocity and crossflow streamlines at peak ($t_1 = 0.25\ s$) and reversed ($t_2 = 0.41\ s$) flow phases and at monitoring plane 3, where the effects of graft designs and the swirling motion are more meaningful in comparison with monitoring planes 1 and 2, as was observed in Section 3.5. The incorporation of the spiral ridge and its enhancement results in an increase of rotation

and asymmetry of the transverse flow field. At both phases, the configuration of enhanced spiral graft shows a more important preponderance attributed to the dissipation of weaker vortices, a single dominant spiral and the complete development of the swirling flow.

A decrease in area-weighted secondary velocity magnitude can be observed by comparing the conventional ($0.067\ m\ s^{-1}$) to spiral ($0.061\ m\ s^{-1}$) grafts at the peak flow phase. This slight discrepancy is caused by the 'undeveloped' swirling flow of the spiral graft case. This would be in line with the investigation by Bechara *et al.* [82] where it was shown that the spiral flow graft did not lead to higher patency rates in comparison to conventional graft.

Transient haemodynamics metrics, such as Time-Averaged WSS (TAWSS), TAWSS Gradient (TAWSSG), Oscillatory Shear Index (OSI) and Relative Residence Time (RRT), have been identified as important fluid dynamic parameters to predict the development of cardiovascular diseases under physiological pulsatile conditions [83]. Such fluid dynamic variables are analysed according to the widely accepted low/oscillatory shear theory [114].

Figure 3.16 shows the distributions of TAWSS on the unfolded model of the host artery. TAWSS is defined through:

$$TAWSS = \frac{1}{T} \int_0^T |\boldsymbol{\tau}_w|\, dt \tag{3.8}$$

Where $\boldsymbol{\tau}_w$ is the WSS vector and T is the period of the flow cycle corresponding to $0.9\ s$ in the present case. An increase of the asymmetry intensity of the TAWSS is observed when the spiral ridge is added to the graft. The higher intensity of the swirling flow when the spiral ridge is enhanced, mainly caused by the orientation of

the ridge, slightly extends the region of high-TAWSS towards the occluded section, as was observed under steady-state conditions.
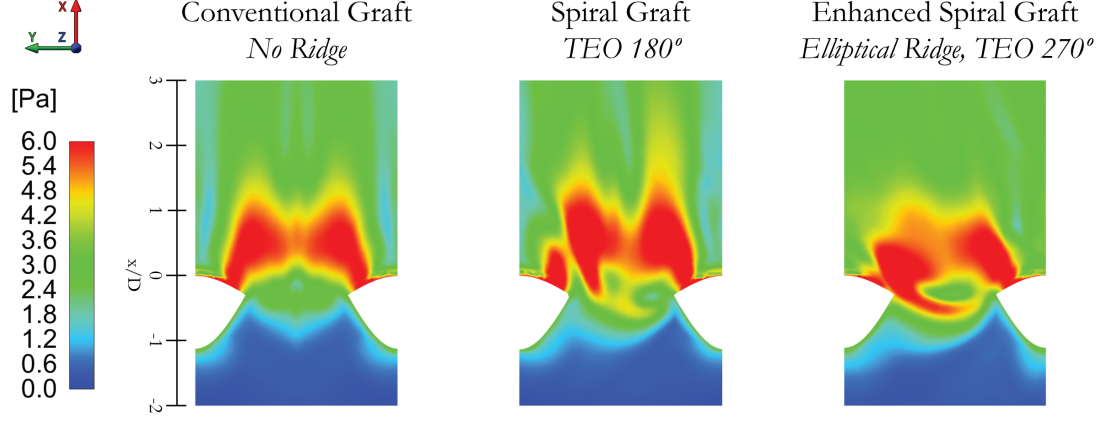
Figure 3.16: Distributions of Time-Averaged WSS on the unfolded model of the host artery.

Figure 3.17 shows the distributions of TAWSSG defined as:

$$TAWSSG = \frac{D_G}{\tau_0} \frac{1}{T} \int_0^T \sqrt{\left(\frac{\partial \tau_x}{\partial x}\right)^2 + \left(\frac{\partial \tau_y}{\partial y}\right)^2 + \left(\frac{\partial \tau_z}{\partial z}\right)^2} \, dt \qquad (3.9)$$

Where D_G is the diameter of the graft ($6~mm$) and τ_0 is the WSS corresponding to the Poiseuille flow under average flow conditions ($0.82~Pa$). Regions of high TAWSSG are identified in the anastomoses at the toe, heel and the stagnation point on the bed of the host artery. The spiral ridge shifts and extends these regions, while the enhanced spiral ridge generates a non-uniform band of high TAWSSG in the cross-sectional plane of the toe.

The analysis of OSI and RRT is presented in Figures 3.18 and 3.19 and described in Equations 3.10 and 3.11, respectively:

$$OSI = \frac{1}{2} \left(1 - \frac{\left| \int_0^T \vec{\tau}_w dt \right|}{\int_0^T |\vec{\tau}_w| \, dt} \right) \qquad (3.10)$$

64
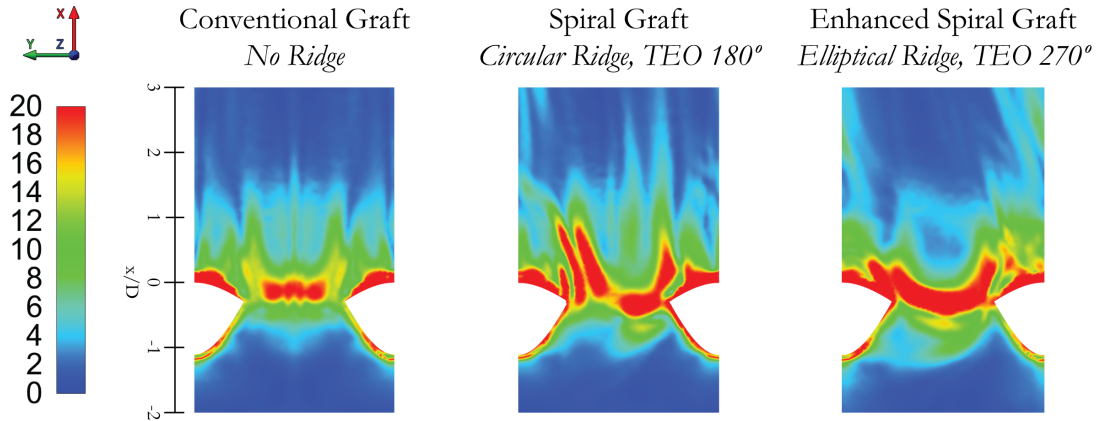
Figure 3.17: Distributions of Time-Averaged WSS Gradient on the unfolded model of the host artery.

$$RRT = \frac{1}{(1 - 2 \times OSI) \times TAWSS)} = \frac{1}{\frac{1}{T}\left|\int_0^T \vec{\boldsymbol{\tau}}_w dt\right|} \tag{3.11}$$

Regions of high OSI and RRT are initially symmetrical and located at the heel and around the impingement point in the case of conventional graft. The incorporation of the spiral ridge results in an oblique elevated region within the anastomosis and occluded region. The effect of the spiral ridge also results in asymmetry of the high OSI and RRT region distally extended from the toe which is dissipated by means of the enhancement of the ridge design.

3.7 Limitations

While the present study represents an important step towards improving the design and performance of spiral-inducing grafts, in order to find the 'optimum' configuration, further work is required to construct an appropriate 'cost function' against which to perform shape optimisation. The range of possible design configurations
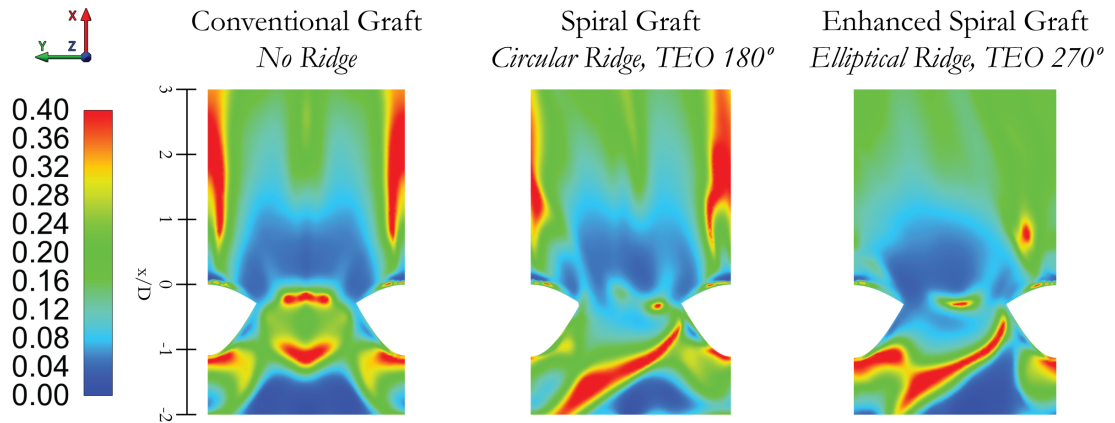
Figure 3.18: Distributions of Oscillatory Shear Index on the unfolded model of the host artery.
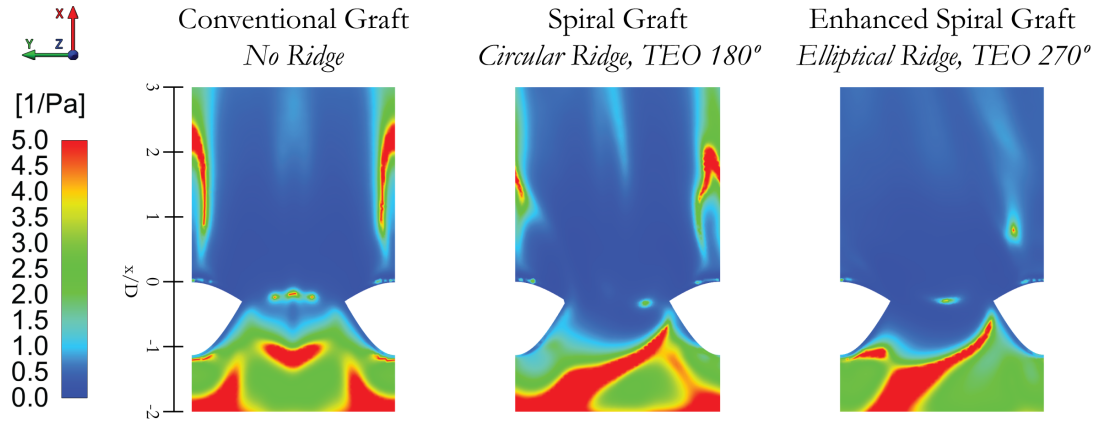
Figure 3.19: Distributions of Relative Residence Time on the unfolded model of the host artery.

in the problem presented in this work is large, therefore one would have to extend the number of design parameters and their range in order to undertake a complete shape optimisation. Furthermore, this work has employ a simplified geometry of distal anastomosis in agremeent with benchmark studies and with the purpose of elucidating the role of each design parameters on haemodynamics. However, with access to patient-specific cases and supported with the current increase of computa-

tional power, personalised geometries and dynamic conditions could be implemented according to the future trends of personalised medicine.

The interaction of the spiral ridge and out-of-plane grafts need to be investigated to match the direction of the spiral ridge with that resulting from the graft out-of-plane to maximise the swirling motion. Moreover, further studies are required in order to test a wider range of physical, geometrical and haemodynamic properties of both helical and spiral designs with a view to be utilised in different types of bypass grafts.

Although there are evidences in literature that justify the assumption of rigid walls under the present fluid dynamic conditions, compliance mismatch has been identified as an important postoperative factor in the development of restenosis around the suture line of the anastomosis [67,88,115]. The implementation of fluid-structure interaction considering the different mechanical properties of graft and host artery together with transient and physiological boundary conditions and the required level of accuracy could be accomplished using High Performance Computing (HPC).

Another possible future extension for the present study would be to study the proximal anastomosis, where the size of the ridge and the shape of the leading edge could lead to an increase in fluid resistance, the damage of inflow conditions to the prosthetic graft and the deposition of cholesterol, calcium, cellular debris and fatty substances at the leading edge.

All these points represent current lines of research within the author's research group.

Chapter 4

Lagrangian Approach

4.1 Introduction

The Eulerian analysis of haemodynamics in spiral grafts described the effects of the ridge design and highlighted the influence of the ridge orientation and height on inducing enhanced swirling flow, as was discussed in Chapter 3.

However, the traditional concept of blood as a continuous fluid contradicts the physiological rheology of this heterogeneous fluid in which a high volume concentration of biological particles (red blood cells, white blood cells and platelets) travel in a continuous phase (blood plasma) and define the mechanical properties of this non-Newtonian suspension.

This chapter will use of the Lagrangian fluid dynamic description, expounded in Chapter 1, and particle tracking simulations in order to assess and compare the transport of representative particles and the direct deposition on the boundary walls under the effects of the swirling flow generated by the different designs of spiral-inducing grafts described in Chapter 2.

4.2   Literature review

With the purpose of mimicking the behaviour of biological multiphase flows, particle-haemodynamics has been used to model various phenomena and devices of cardio-vascular and respiratory systems. In such applications, different numerical methods have demonstrated appropriate capabilities for modelling the blood as an heterogeneous mixture: Eulerian-Eulerian [116–120], Eulerian-Lagrangian [121–127] or Lattice-Boltzmann [128–130] methods, among others.

The Eulerian-Eulerian method is a multiphase model that provides global information of the particulate matter which is approximated as an additional continuous phase [97]. The capability of including cell and particle transport using the Eulerian-Eulerian method was highlighted by Ou *et al.* [120] to study the pathological response of intracranial aneurysms. Their results reported a prevalence for particle deposition in regions of patient-specific aneurysms characterised by flow disturbance, low WSS and complex secondary flow patterns. Similarly, Wen *et al.* [131] applied the Eulerian multiphase model to investigate the haemodynamics in helical grafts and proved its performance improvement against conventional artery bypass grafts. The swirling flow induced by the non-planar geometry decreased the accumulation of red blood cells in the distal anastomosis.

The Eulerian-Lagrangian method, also known as Lagrangian particle tracking multiphase model, couples the Eulerian framework, used to described the behaviour of the continuous phase, and the Lagrangian transport model, which traces the motion of discrete particles [97]. This model enables researchers to obtain complete information about the individual behaviour of dispersed particles as well as about the continuous phase. Longest *et al.* [123–125] studied the transport of particles in femoral ETS distal anastomoses linked to the development of vascular diseases

and proposed the near-wall residence time model capable of accounting for particle deposition and activation as well as surface reactivity. This model was used to assess the effects of the graft-end cut and the diameter ratio between graft and artery, including its application to Miller cuff, pre-cuffed, streamlined and conventional anastomotic configurations [123–125]. Basciano *et al.* [126, 127] implemented particle transport modelling to elucidate the particle transport associated to the development of intraluminal thrombus in abdominal aortic aneurysm. In addition to the assessment of fluid-related parameters, a detailed analysis of particle haemodynamics, including, among others, near-wall particle distribution and shear stress on particle surface linked to blood particle activation, successfully predicted the thrombus formation in a patient-specific case. The behaviour of micro-particles involved in the treatment of liver tumours and embolisation therapies has also been studied using particle transport modelling by Basciano [126] and Johnson *et al.* [122], respectively. For its part, Fabbri *et al.* [121] used particle tracking simulations to study the effect of emboli characteristics and the geometry of the cerebral arterial network on particle distributions.

In contrast to finite volume methods, Lattice-Boltzmann model considers the fluid as an aggregation of particles moving between Cartesian lattice points [132]. The growing use of this method has shown a particular relevance for modelling aggregation, deformation and interaction of particles [120].

This chapter will comparatively assess the movement of representative particles and the direct deposition on the model walls as a result of the enhanced swirling flow generated by different designs of spiral graft. Based on the aforementioned Eulerian-Lagrangian methodologies for particle-haemodynamics [121–127], the Lagrangian particle tracking multiphase model, available in the software package used

throughout the project, was used together with the geometrical and dynamic conditions defined in Chapters 2 and 3.

4.3   Computational model

4.3.1   Computational domain and mesh

The computational domain remains the ETS distal graft anastomosis described in Chapter 2 and 3. In this chapter, in order to evaluate the deposition of particles in the different zones of the anastomosis, with particular emphasis in those regions prone to the development of vascular diseases in prosthetic grafts and ETS anastomotic configurations, the junction was split into six different zones: toe, heel, host artery 1 (HA1 or upper wall), host artery 2 (HA2 or lateral side at orientation 90°), host artery 3 (HA3 or bed of the host artery) and host artery 4 (HA4 or lateral side at orientation 270°), as shown in Figure 4.1.

Finite-volume hybrid meshes of prismatic and tetrahedral elements are again developed using ANSYS Meshing (Version 17.1, Academic Research CFD license, ANSYS Inc., Canonsburg, USA). On the basis of the grid analysis carried out in Chapter 3 using Eulerian metrics, the computational mesh has additionally been evaluated to verify the independence of Lagrangian results, area integral of particle momentum flow density at the outlet, to further mesh refinements using the reference graft design. Meshes with numbers of elements between 3.06 and 3.43 million, depending on the geometry simulated in each case, assured differences less than 1% in the abovementioned metric with a feasible computational cost, as shown in Figure 4.2.
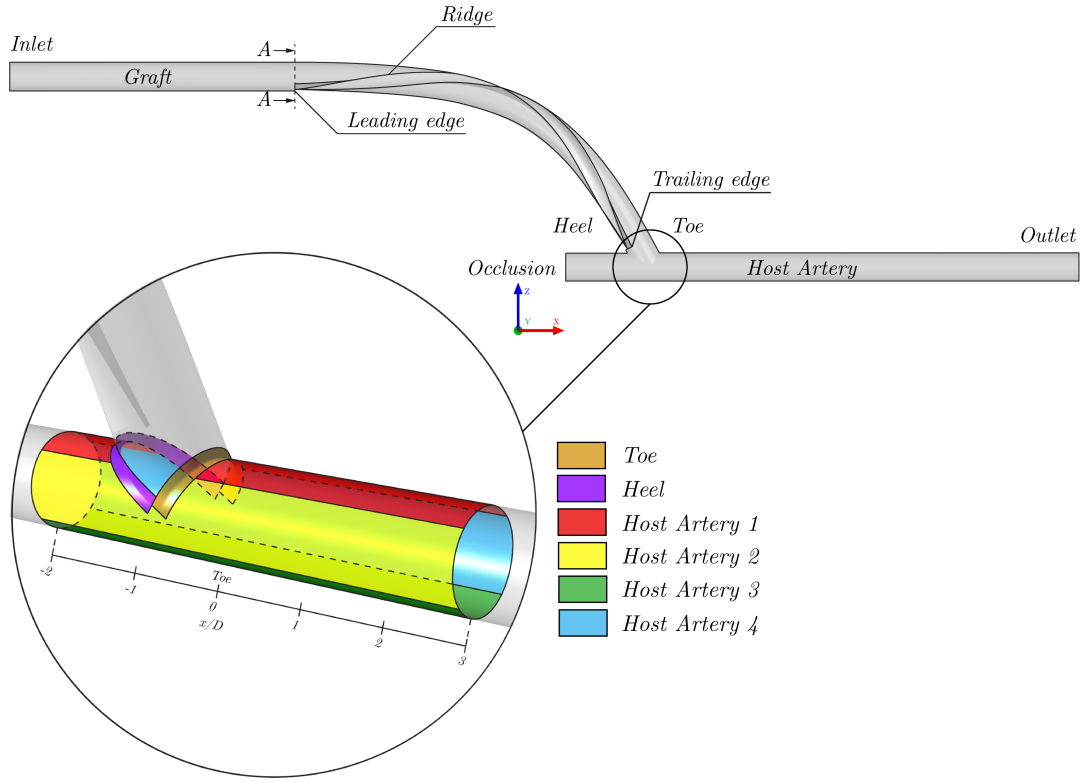
Figure 4.1: Schematics of the computational model with detail in the different regions of interest.

4.3.2 Lagrangian particle tracking multiphase model

Particle transport modelling is a multiphase technique that enables the computational simulation of solid particles (disperse phase) travelling in a continuous phase by coupling the Eulerian and Lagrangian fluid dynamics descriptions. In ANSYS CFX [96,97], the multiphase flow is simultaneously governed by the continuity and Navier-Stokes equations for the continuous phase (Equations 4.1) and particle momentum equations for the Lagrangian phase (Equations 4.2):

$$\nabla \cdot \boldsymbol{u} = 0 \qquad\qquad \nabla \cdot (\rho \boldsymbol{u} \boldsymbol{u}) = -\nabla p + \nabla \cdot (\bar{\bar{\tau}}) \qquad\qquad (4.1)$$
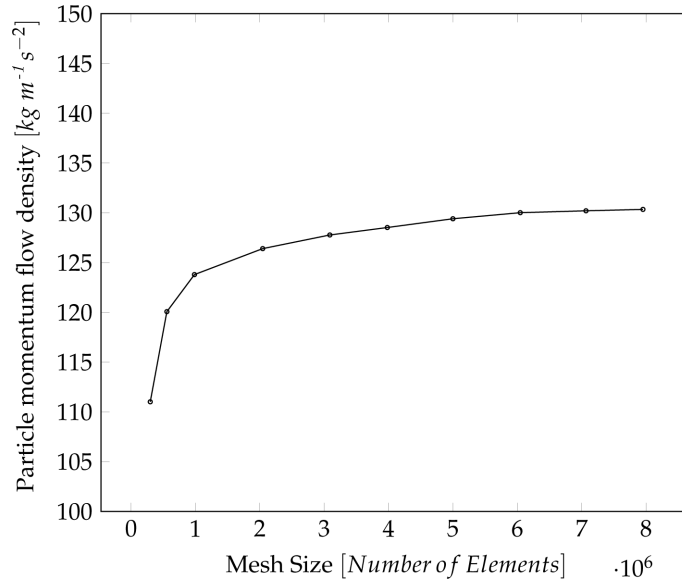
Figure 4.2: Area average of particle momentum flow density at the outlet for different levels of mesh refinement.

$$m_p \frac{d\boldsymbol{u}_p}{dt} = \sum \boldsymbol{F}_i \qquad (4.2)$$

where $\boldsymbol{u}$ and $\boldsymbol{u}_p$ are the velocities of fluid and particles, respectively. $\boldsymbol{F}_i$ represents the forces acting on particles and consists of drag force ($\boldsymbol{F}_D$), buoyancy force ($\boldsymbol{F}_B$), pressure gradient force ($\boldsymbol{F}_P$), rotational forces ($\boldsymbol{F}_R$) and virtual mass force ($\boldsymbol{F}_{VM}$) [96, 97].

The drag force acting on particles is described proportional to the relative velocity of the fluid with respect to the particle.

$$\boldsymbol{F}_D = \frac{1}{2} C_D \rho_f A_p \left| \boldsymbol{u} - \boldsymbol{u}_p \right| (\boldsymbol{u} - \boldsymbol{u}_p) \qquad (4.3)$$

Where C_D is the drag coefficient and A_p is the particle cross-section. Building on the assumption of spherical and disperse particles, the drag coefficient, C_D, can be modelled using the Schiller-Naumann model based on experimental results [96, 97]:

$$C_D = \frac{24}{Re}(1 + 0.15 Re^{0.687})$$ (4.4)

The gravitational force due to the density difference between particles and the continuous phase is implemented by means of the buoyancy force:

$$\boldsymbol{F}_B = (m_p - m_f)\mathbf{g}$$ (4.5)

Wen *et al.* [131] showed the importance of the gravitational force in cell transport by favouring particle sedimentation along its direction. In this study, the force of gravity is considered in the direction of -Z axis (see Figure 4.1).

The pressure gradient force accounts for the pressure difference around the particles as a result of the fluid acceleration.

$$\boldsymbol{F}_P = -\frac{m_f}{\rho_f}\nabla p$$ (4.6)

In the present study, the fluid domain remains stationary, so rotational forces (centripetal or Coriolis) are discarded.

The virtual mass force evaluates the acceleration of the fluid that would occupy the volume of the particle. This force is representative in flows with noticeable accelerations and in the motion of bubbles where the mass of the displaced fluid is much higher that the mass of the discrete phase.

$$\boldsymbol{F}_{VM} = \frac{C_{VM}}{2}m_f\left(\frac{d\boldsymbol{u}_f}{dt} - \frac{d\boldsymbol{u}_p}{dt}\right)$$ (4.7)

The maximum contribution of this force was evaluated by considering a non-dimensional virtual mass coefficient, C_{VM}, equal to 1. A minor influence of 0.01% in deposition ratio on the entire model of the ETS distal graft anastomosis was reported, and thus the effect of virtual mass force was neglected in this study, in concordance with [121, 122, 126].

The influence of the remaining forces, i.e. drag, bouyancy and pressure gradient forces, was evaluated in terms of particle deposition at the different zones of the anastomosis using the cases defined in Table 4.1. Figure 4.3a illustrates the noteworthy influence of the buoyancy forces and the negligible effects of the pressure gradient force.

Accordingly, in the present computational procedure, drag and buoyancy forces will govern the motion of particles immersed in the continuous phase through the model of ETS distal graft anastomosis illustrated in Figure 4.1.
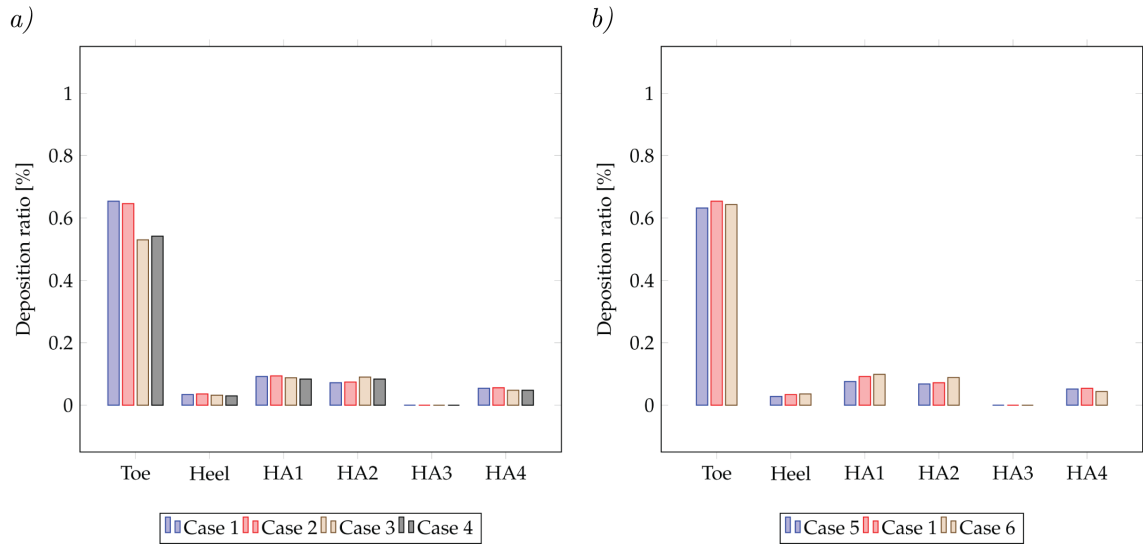
Figure 4.3: Effect of the different parameters in the Lagrangian model: a) influence of the different forces acting on particles and b) influence of the number of particles.

Table 4.1: Description of the different cases for the analysis of the influence of forces acting on particles and the number of particles.

Case		Forces		Number of particles
Case 1	Drag	Buoyancy	Pressure grad.	50000
Case 2	Drag	Buoyancy	-	50000
Case 3	Drag	-	Pressure grad.	50000
Case 4	Drag	-	-	50000
Case 5	Drag	Buoyancy	Pressure grad.	25000
Case 6	Drag	Buoyancy	Pressure grad.	75000

4.3.3   Blood characterisation

As introduced in Chapter 1, the rheology of the blood in a Lagrangian framework defines the fluid as discrete particles travelling in a continuous phase. Red blood cells (RBCs) represent the predominant solid phase and can amount to about 40 to 45%, much higher than the 1% corresponding to the concentration of white blood cells [46, 120, 133]. The influence of RBCs is not only observed in volume concentration but also in mechanical properties through shear thinning, viscoelasticity, thixotropy and yield stress. With the purpose of assessing the effects of the swirling flow on the behaviour of generalised particles, that may represent blood cells, cellular debris or fatty substances, idealised RBCs, whose size is intermediate between white blood cells and platelets, were considered as representative particles in this comparative study.

Accordingly, the heterogeneous mixture is characterised by representative particles with a diameter and density of $7.2\,\mu m$ [134] and $1099.6\,kg\,m^{-3}$ [135], respectively. Consistent with the rheology model used in Chapter 3, the continuous phase was modelled with a density of $1050\,kg\,m^{-3}$ and the Carreau-Yasuda viscosity model described in Section 3.2.3.

4.3.4 Boundary conditions

From this perspective, the performance of spiral grafts was evaluated by injecting 20,000 particles, which entails an affordable computational cost, at the inlet with the continuous fluid at a velocity of 0.317 m s^{-1} (Re = 570). The analysis of the influence of the number of particles injected at the inlet gave rise to minor differences in particle deposition at the different zones of the anastomosis, as shown in Figure 4.3b. Zero-pressure conditions were considered at the outlet. The walls were considered rigid and non-slip. The particle-wall interaction in ANSYS CFX is described by means of restitution coefficients [96,97]. The normal, R_n, and tangential, R_t, restitution coefficients are defined as the ratio between normal and tangential velocities after and before the impact with the wall, as illustrated in Equations 4.8 and Figure 4.4.

$$R_n = v_{2n}/v_{1n} \qquad R_t = v_{2t}/v_{1t} \tag{4.8}$$
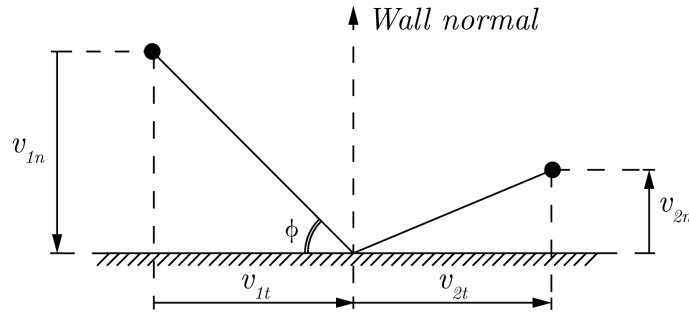
Figure 4.4: Model of particle-wall interaction and definition of restitution coefficients.

Where v_{in} and v_{it} represent the normal and tangential components of velocity, respectively, and ϕ is the angle of impact. Zero restitution coefficients, representing

fully inelastic collisions, were considered in this investigation to study the deposition of particles.

The three-dimensional and steady simulations that constitute the comparative study were conducted using ANSYS CFX (Version 17.1, Academic Research CFD license, ANSYS Inc., Canonsburg, USA). The convergence criteria was established taking into consideration both Eulerian and Lagrangian metrics. The global balance of the conservation equations and a RMS residual criterion of $5 \cdot 10^{-6}$ ensured the independence of results to further levels of convergence in the present configuration of ETS distal graft anastomosis.

Particle transport was also modelled under transient boundary conditions in order to assess the pulsatile behaviour of blood cells. A high resolution second-order backward Euler method was used for the transient scheme with a time step of 0.01 s. The residual criterion to ensure the convergence of the numerical method was set to $5 \cdot 10^{-6}$ supported by the global balance of the conservation equations. The results presented in Section 4.6.1 were extracted from the last of four simulation periods in order to avoid initial instabilities of the numerical procedure [98]. Further details will be given in Section 4.6.1.

4.4 Validation

The present computational setting was validated against the experimental results of Johnson *et al.* [122] aimed at elucidating the influence of operating parameters (injection technique, particle diameter and flow blockage) on the efficiency of the embolisation treatment using a multi-branch artery. The type of boundary conditions implemented by Johnson *et al.* in terms of steady-state mass flow rate and zero-pressure at the inlet and outlets, respectively, is in concordance with the dy-

namic description of the present study. Numerical and experimental exit fractions, defined as the ratio of particles that exits the domain through each outlet and the number of injected particles, were compared.

At the inlet, the multiphase flow with 10,000 particles characterised by a diameter and density of $0.125\,mm$ and $1600\,kg\ m^{-3}$, respectively, was uniformly injected with a constant mass flow rate of $7.067 \cdot 10^{-4}\ kg\ s^{-1}$. Zero-pressure conditions were imposed at the three outlet branches. According to the experimental procedure, no deposition on the wall was considered and, consequently, restitution coefficients were set equal to 1. In this problem, the convergence of results was achieved using a residual criterion of $2.5 \cdot 10^{-5}$.

The comparison between numerical-experimental results led to differences in exit fractions less than 5% for the different outlet branches. These results, corresponding to the Lagrangian analysis of an idealised multi-branch model, provide a favorable assessment on the accuracy of the subsequent simulations using the present methodology for the bypass graft.

4.5   Results

The results derived from the application of the Lagrangian particle tracking multiphase model to the different designs of spiral grafts defined in Chapter 2 were analysed in terms of particle trajectories and deposition and comparison is made against Eulerian haemodynamic metrics.

In spite of this study being focussed on the distal anastomosis, the Lagrangian particle tracking multiphase model provides relevant results that support the assumption introduced in Chapter 3 about the potential deposition of blood cells, fatty substances and cellular debris on the leading edge.

4.5.1 Trajectories and deposition of particles

Trajectories and deposition of particles have been investigated in the region of interest located between $(-2D, 3D)$ with respect to the toe of the anastomosis, in concordance with the region defined in Chapter 3 for the analysis of WSS-based haemodynamic metrics. The colour of particle terminal locations and trajectories in the following figures represents the region of impingement according to Figure 4.1. The quantification of particle terminal locations in each region of impingement is given in Table 4.2 in terms of deposition ratios, defined as the number of particles that collide in each region of interest when comparing with the total number of injected particles (20,000 particles). This analysis has been complemented with the longitudinal distribution of terminal locations along the x-direction of the host artery, shown in Figure 4.9.

Figure 4.5 shows the particle-transport results in terms of particle trajectories and deposition for different cross-sectional designs. The strength of the swirling flow introduces a moderate asymmetry in the behaviour of particle trajectories at the outlet of the graft that are subsequently affected by the surrounding boundaries in the host artery. In this sense, depending on the relative position of particles to the lateral boundaries at the outlet of the graft, particles are diverted to the near corner defined by the toe, HA1 and HA2 or HA4 when particle locations at the outlet of the graft are close to HA2 or HA4, respectively. Both behaviours share a common region of deposition at the upper wall of the host artery in the downstream direction. As can be observed in Figure 4.5, the effect of the decrease of the ridge height, from $L_1/D = 0.3$ to 0.2, also results in a reduction of particle deposition in the region HA1 corresponding to the upper wall of the host artery and a consecutive decrease of particle depositon in the region of the toe. These last results begin at the

region of the toe with a noteworthy and rapid decrease in particle deposition along the x-direction of the host artery, as shown in Figure 4.9a. Likewise, a residual deposition of particles close to the heel can be observed with the increase of the ridge width. However, taking into account the effects of other design parameters, that will be studied below, the influence of the cross-sectional design leads to less significant differences in particle transport, which is in line with the results obtained using the Eulerian approach in Chapter 3.

Figure 4.5: Trajectories and terminal locations of those particles that collide on the regions of interest in the host artery for different cross-sectional designs of a single ridge.

The significant effects in the response of particles to the flow produced by different orientations of a single circular ridge are illustrated in Figure 4.6. The influence of the trailing edge orientation on the induction of spiral flow was highlighted in Chapter 3 using the traditional Eulerian haemodynamics. Accordingly, the more pronounced swirling flow produced by the configuration with ridge orientation 270° results in an asymmetrical distribution of particle deposition. In this configuration,

the deposition of particles at the region HA2 is generated by the presence of the weaker vortex close to this boundary that is still not dissipated at monitoring planes 1 and 2 according to Figure 3.5. This asymmetrical ejection of particles further away in the streamwise direction and assisted by the rotational flow increase the deposition of particles in the region HA2 with respect to the other orientations. As shown in Figure 4.9b, the trailing edge orientations 90° and 180° give rise to the highest depositions of particles at the region of the toe and the entire anastomosis in contrast to the ride orientation 0° that, interestingly, reports the lowest deposition of particles. By contrast, a perceptible particle disturbance and deposition is produced at the region of occlusion with the ridge orientations 90° and 270°.

Figure 4.6: Trajectories and terminal locations of those particles that collide on the regions of interest in the host artery for different ridge orientations.

Figure 4.7 shows the effects of the multi-ridge configurations on particle-haemodynamics. The increase of the number of ridges results in a global decrease of particle deposition with respect to the reference case, with a noteworthy reduction in the case of double ridge. Particularly, this increase in the number of ridges reduces the deposition at the toe and slightly increases the impingement of particle at the heel with respect to the reference case, as illustrated in Figure 4.9c. However, as was observed in Chapter 3, the effects of the number of ridges are again more influenced by the orientation of the ridges than by the very nature of the multiridge configuration.
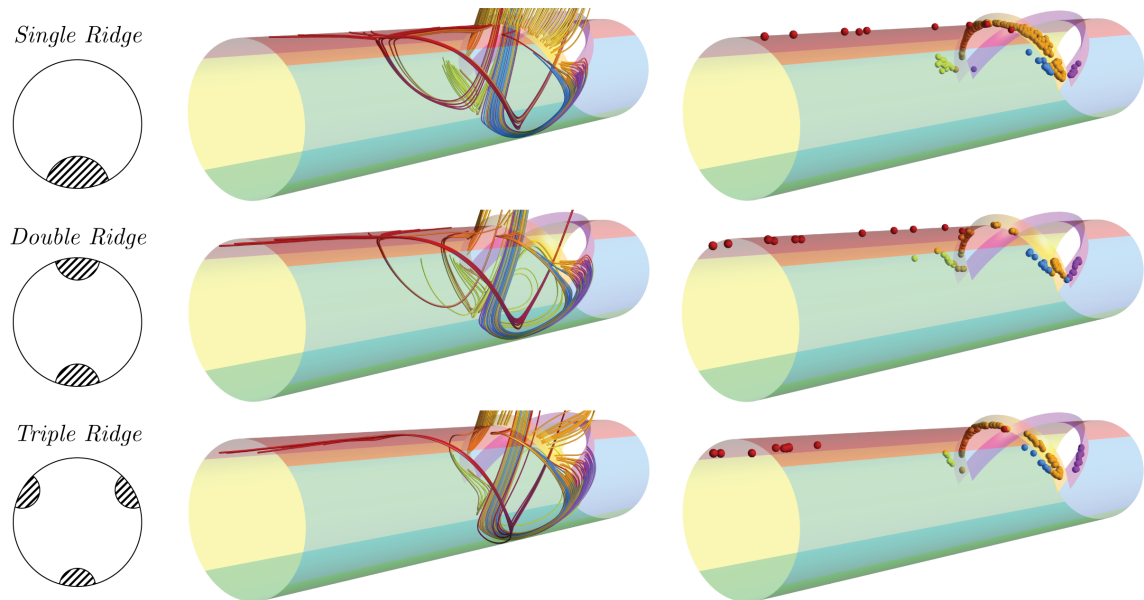
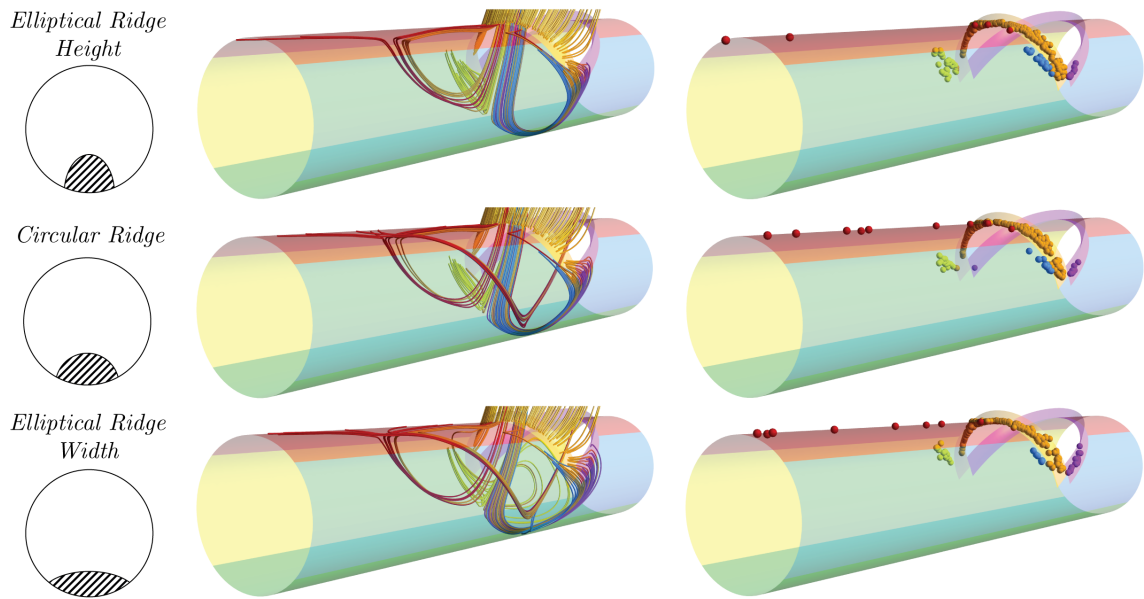
Figure 4.7: Trajectories and terminal locations of those particles that collide on the regions of interest in the host artery for different number of ridges.

The influence of the ridge pitch on particle trajectories and deposition is illustrated in Figure 4.8. An increase in the number of particles deposited in the region HA1 is reported with the consecutive increase of the ridge pitch. In the vicinity of the anastomosis, the number of particles deposited at the toe increases with the

consecutive decrease of the helical pitch, as illustrated in Figure 4.9d. At the heel, a slight increase in particle deposition is reported with the increase of the pitch, as shown in Table 4.2.
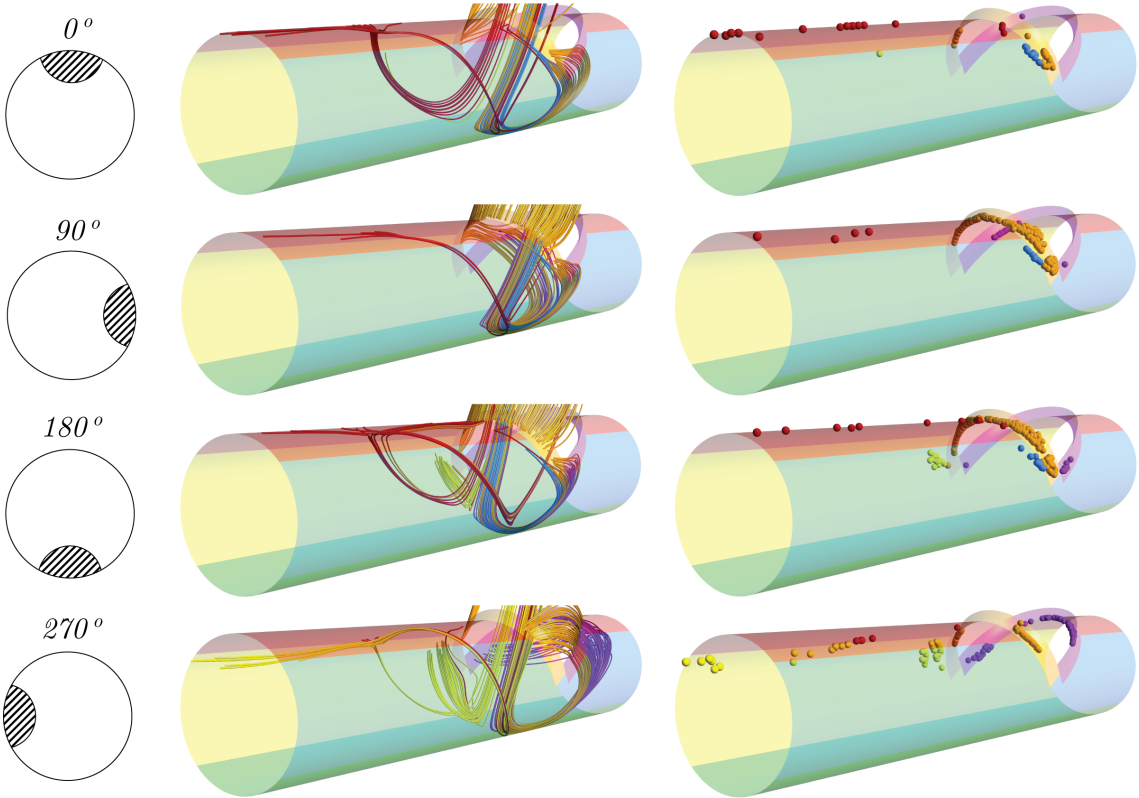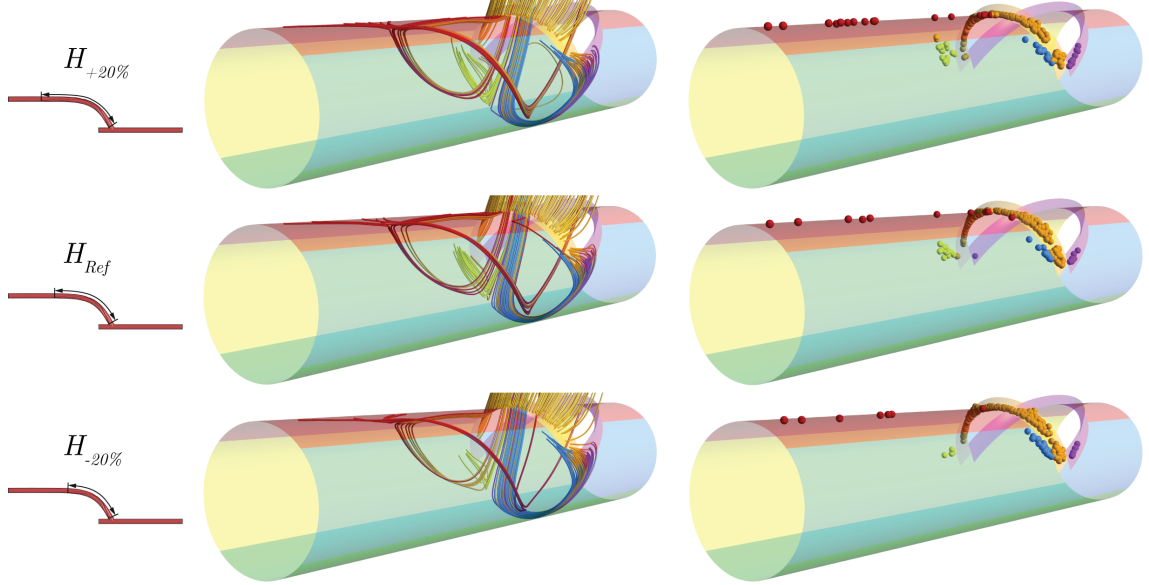

Figure 4.8: Trajectories and terminal locations of those particles that collide on the regions of interest in the host artery for different ridge pitches.

Table 4.2: Percentage of deposition ratios for different ridge designs.

		Toe	Heel	HA1	HA2	HA3	HA4	Leading edge
Cross-sectional designs	Elliptical - Height	1.270	0.045	0.030	0.145	0.000	0.095	1.400
	Circular	1.135	0.045	0.060	0.085	0.000	0.070	1.395
	Elliptical - Width	1.035	0.070	0.045	0.070	0.000	0.030	1.220
Trailing edge orientation	0°	0.255	0.005	0.085	0.005	0.000	0.060	1.560
	90°	1.070	0.105	0.020	0.000	0.000	0.045	1.410
	180°	1.135	0.045	0.060	0.085	0.000	0.070	1.535
	270°	0.370	0.265	0.025	0.250	0.000	0.000	1.530
Number of ridges	Single	1.135	0.045	0.060	0.085	0.000	0.070	1.535
	Double	0.400	0.065	0.060	0.050	0.000	0.065	1.465
	Triple	0.810	0.065	0.055	0.025	0.000	0.035	1.280
Pitch	$H_{+20\%}$	1.115	0.055	0.100	0.105	0.000	0.070	1.450
	H_{ref}	1.135	0.045	0.060	0.085	0.000	0.070	1.535
	$H_{-20\%}$	1.275	0.035	0.035	0.025	0.000	0.110	1.195
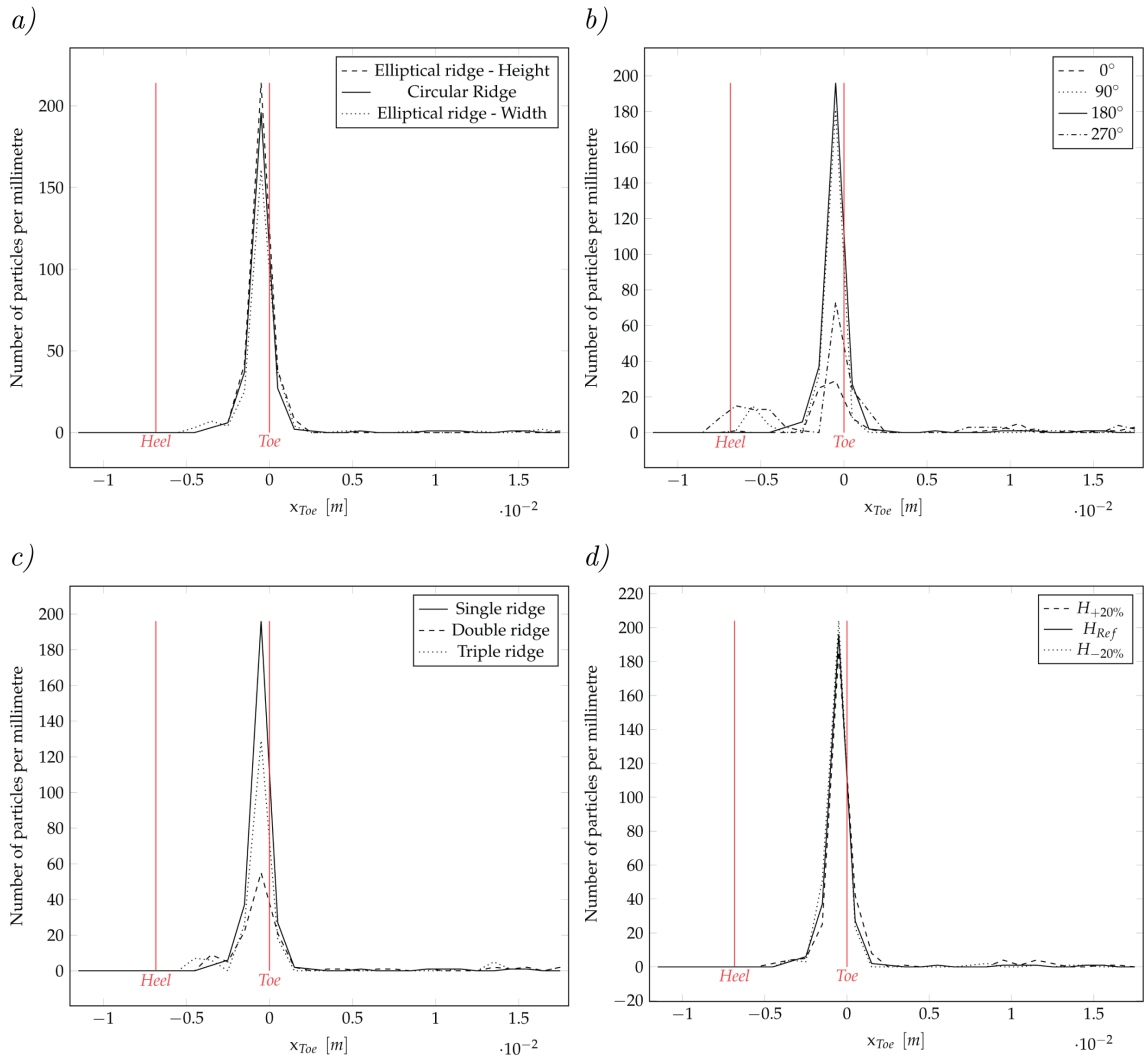
Figure 4.9: Distribution of particle terminal locations along the regions of interest in the host artery. Solid lines represent the reference case in each figure.

4.5.2 Impingement of particles on the leading edge

From the Lagrangian perspective, the number of particles that impinge on the leading edge can be assessed in terms of the deposition ratios listed in Table 4.2. The bulk flow impinges on the blunt surface of the ridge and particles collide generating higher deposition ratios than those obtained in the anastomotic region.

The elliptical ridge configurations, particularly with the increase of the ridge width, results in a slight decrease of particle deposition in the leading edge with respect to the reference case. Regarding to the orientation of the ridge, the cross-sectional area and shape of the single ridge remain the same with the variation of the ridge location and generate similar deposition ratios at the leading edge. In the multi-ridge configurations, the deposition ratio at the leading edge decreases with the increase of the number of ridges. When varying the pitch of the ridge, the deposition of particles in the leading edge is affected by the initial curvature of the graft in the configuration $H_{-20\%}$. As a result, the decrease of the ridge pitch reduces the deposition of particles at the leading edge.

4.5.3 Correlation between WSS and particle deposition

In Figures 4.10-4.13, the distributions of shear force are represented on an unfolded model of the host artery. In this case, terminal locations of particles have been superimposed in order to evaluate any potential correlation between Eulerian and Lagrangian haemodynamic metrics.

The effect of different cross-sectional shapes in such correlation is represented in Figure 4.10. The deposition of particles represented through the lateral edge of the graph indicates deposition of particles approximately in the intersection of the plane XZ and the upper wall of the host artery. The enhancement of the swirling flow with the increase of the ridge height reduces the number of terminal locations in this region. As will be also observed through the different correlations under steady-state boundary conditions, it can be observed a tendency of particle deposition in regions of low WSS.

Figure 4.10: Correlation between distributions of WSS and particle deposition on the unfolded model of the host artery for different cross-sectional designs of a single ridge.

The Eulerian-Lagragian correlation under the effect of the ridge orientation is shown in Figure 4.11. As described in Chapter 3, the interaction of the flow with the surrounding boundaries defines the rotational direction of the fluid flow field in the host artery. Consequently, the trailing edge orientation 270° results in particle deposition at the region of the lateral wall HA2 close to the anastomosis where the spiral flow is still not totally developed. By contrast, terminal locations in the proximity of the heel are an indicator of the flow disturbance in the region of occlusion, as illustrated in Figure 4.6 in the cases with ridge orientations 90° and 270°. As mentioned above, the sweep effect of the shear stress results in distributions of particle deposition out the regions of high WSS.

The variation of the number of ridges shows the implicit influence of the ridge orientations by inducing different asymmetries in the distributions of WSS and particle deposition, as shown in Figure 4.12. As previously stated, the increase in the number of ridges reduces the deposition of particles in the host artery and, particularly, at the toe of the anastomosis with respect to the reference case.
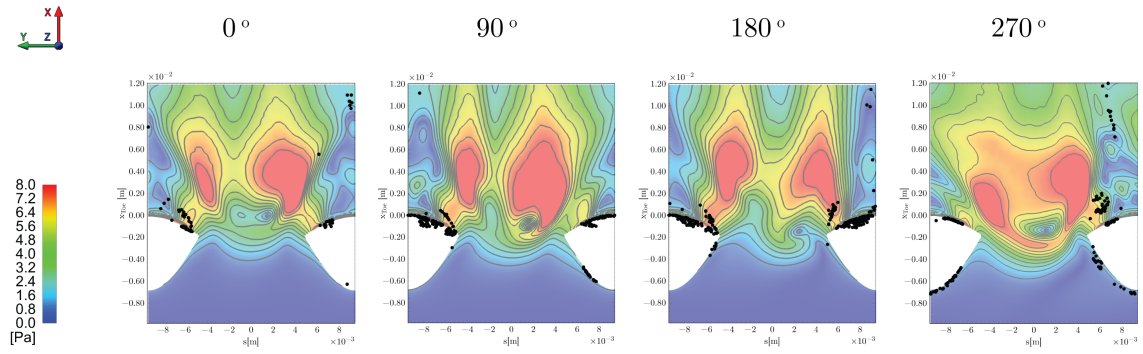
Figure 4.11: Correlation between distributions of WSS and particle deposition on the unfolded model of the host artery for different orientations of the trailing edge.
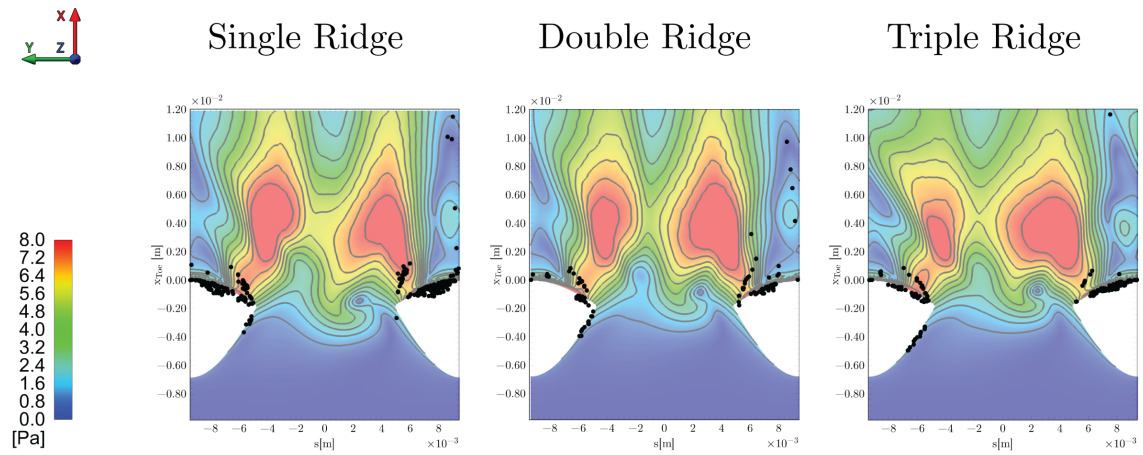
Figure 4.12: Correlation between distributions of WSS and particle deposition on the unfolded model of the host artery for different number of ridges.

Figure 4.13 shows the Eulerian-Lagrangian correlation corresponding to different ridge pitches. The decrease of the pitch reduces the number of deposition points through the right lateral edge of the graph corresponding to impingements at the region HA1 and HA2. By contrast, such decrease in the ridge pitch increases the deposition at the toe and at the region HA4 corresponding to negatives values of the arch length s (horizontal axis).
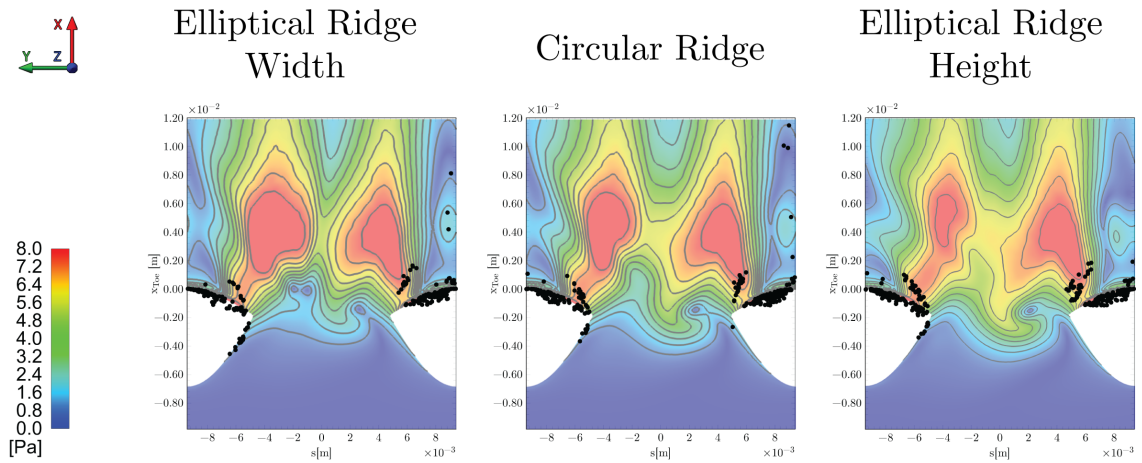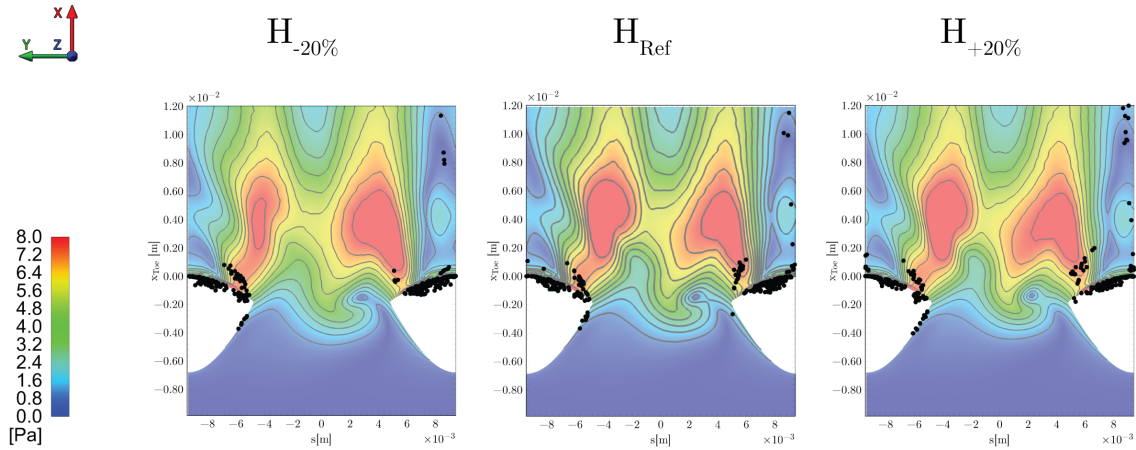
Figure 4.13: Correlation between distributions of WSS and particle deposition on the unfolded model of the host artery for different ridge pitches.

4.6 Discussion

In view of the uncertainty associated with the relationship between fluid mechanics parameters and biological mechanisms attributed to graft failure, the Lagrangian approach was used in this chapter in order to assess the influence of different graft designs on the underlying transport of particles. The Lagrangian particle tracking multiphase model enables one to obtain comprehensive information about the behaviour of discrete and dispersed blood particles travelling in a continuous phase.

As was observed in Chapter 3, changing the orientation and, to a lesser extent, the height of the elliptical ridge have significant influence on producing an enhanced swirling blood flow in the lumen. These effects were also observed using Lagrangian particle tracking in terms of deposition, trajectories and WSS distributions.

The analysis of Figures 4.5-4.9 provided useful information about the predominant areas of particle deposition: toe, heel and the regions HA1, HA2 and HA4 of the host artery. Interestingly, no deposition were reported at the region HA3 in this study. The different designs of grafts alter the relative distribution of particle

deposition in the host artery. The region of the toe was observed as the predominant zone of deposition. The deposition of particles at the heel results from the backward flow rotation after the impingement of the bulk flow in the bed of the host artery and supported by the curvature of surronding wall boundaries.

The orientation of the ridge was again highlighted as an important design parameter to improve the transport of particles in spiral-inducing grafts. In addition to the benefits produced by the configuration with ridge orientation 270°, the trailing edge orientation 0° has interestingly resulted in an even lower deposition of particles on the anastomosis. This fact highlights the need of a complete and multi-approach optimisation to ellucidate the best ridge orientation. Contrary to the widely assumed benefits associated with the Eulerian swirling flow, it was observed that complex and enhanced rotational flow can lead to certain degree of particle disturbance. This evidence is in concordance with the conclusions reported by Ou *et al.* [120] who observed an increase in particle deposition on the regions of aneureyms affected by complex secondary flow. In this particular problem, particle disturbance has particularly been observed in the region of occlusion with the configuration 270°. However, in spite of this particle recirculation detected at the region of occlusion in those cases with enhanced swirling flow, deposition starts in the cross-section corresponding to the heel showing different behaviours along the host artery according to the induced flow field, as can be observed in Figure 4.9. Additionally, it has to be taken into account that the jet flow generated by a case with partial stenosis can drastically change the behaviour of particle in this region. That is why future work is proposed in order to model different degrees of stenosis or alternatively use patient-specific geometries.

The study of the leading edge illustrated the important influence of this region on the inflow conditions. The influence of the ridge and the initial curvature of the graft was observed in the number of particles that impinge on this region.

The particle-tracking approach enabled to observe in this problem a tendency of particle deposition in regions of low WSS, which are prone to the development of vascular diseases, as a result of a lower influence of the sweep effect produced by the bulk spiral flow, as shown in Figures 4.10-4.13. This supports the assumptions that were initially considered as 'optimisation criteria' in Chapter 3 and those that consider high levels of WSS as a beneficial measure to increase the efficiency of prosthetic grafts [100–103].

The present numerical investigation will be complemented in Section 4.6.1 with the study of the pulsatile behaviour of particles using the reference spiral graft.

4.6.1 Particle tracking in spiral-inducing grafts under transient boundary conditions

The reference case (circular ridge with trailing edge orientation 180°) was simulated under pulsatile conditions. Figure 4.14 shows the mass flow rates of fluid and particles that were implemented at the inlet. The fluid mass flow rate corresponds to the waveform used in Chapter 3 obtained from MRI measurements in the femoral artery [113]. Mass flow rate of particles was defined proportionally to that of the fluid with positive values in order to avoid numerical errors associated with negative values of particle mass flow rate.

Figure 4.15 illustrates the trajectories and terminal locations of particles that collide in the region of interest of the host artery. As was expected, the alternation of peak and reversed flow phases results in a noticeable flow disturbance that can
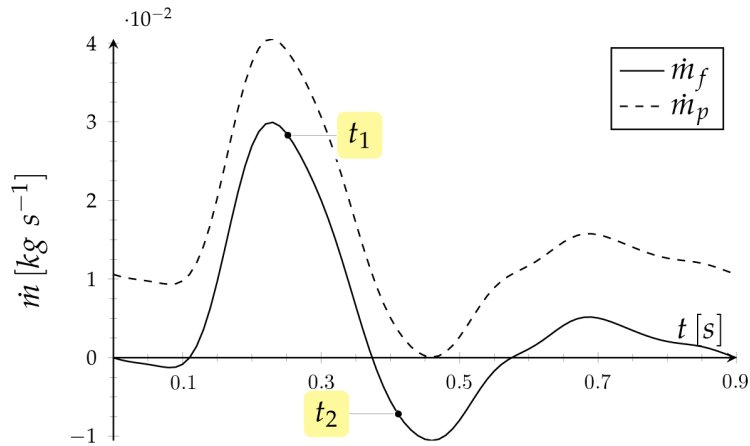
Figure 4.14: Fluid and particle mass flow rates imposed at the inlet of the reference configuration of spiral graft.

be observed in the behaviour of particle trajectories. Contrary to that which has been obtained in the analysis of particle deposition under steady-state boundary conditions, the implementation of pulsatile flow produces impingement of particles on the bed of the host artery.
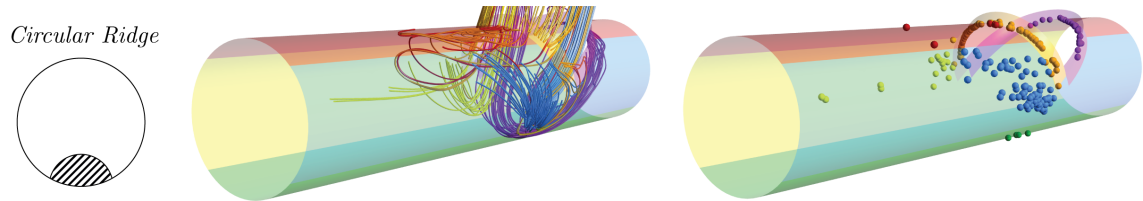
Figure 4.15: Trajectories and terminal locations of those particles that collide on the regions of interest in the host artery of the reference case under pulsatile conditions.

Figure 4.16 illustrates the terminal locations of particles superimposed over the distributions of transient WSS-based haemodynamic metrics. Distributions of TAWSS, TAWSSG, OSI and RRT are represented according to their definitions expressed by the Equations 3.8-3.11 in Chapter 3. However, no clear correlation is observed on this occasion because of the different temporary nature of instantaneous impacts of particles and time-averaged distributions of Eulerian metrics.
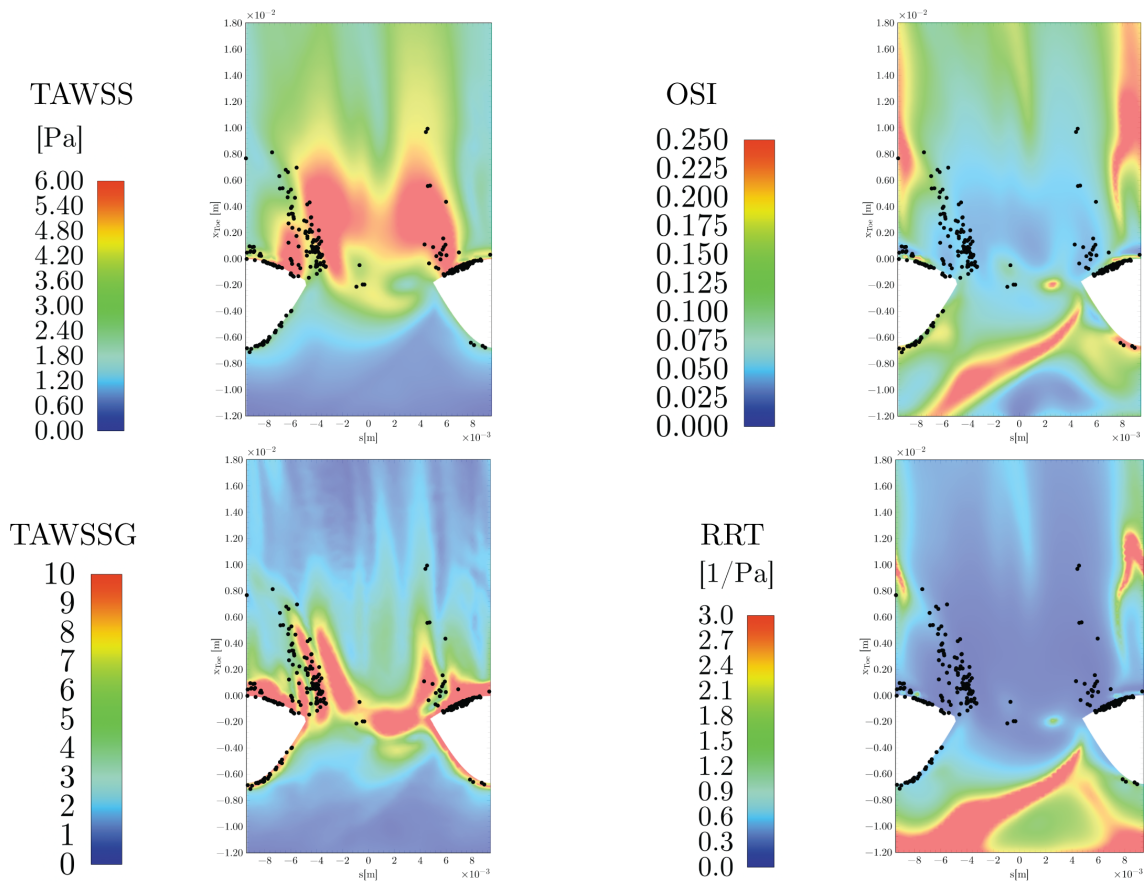
Figure 4.16: Distributions of transient WSS-based haemodynamic metrics and terminal locations of those particles that collide on the regions of interest in the host artery.

4.7 Limitations

An evident shortcoming of this analysis methodology is the implementation of a limited volume concentration of haematocrit. In this investigation, 20,000 particles were used with the purpose of comparing the Lagrangian performance of different designs of spiral-inducing grafts with an affordable computational cost. The use of a physiological level of haematocrit concentration within the appropiate multiphase methology could improve the physiology of the problem in terms of the rheological and mechanical definition of blood.

In line with the above, larger concentrations of blood particles could be additionally considered through the complementary use of different particle transport models, such as the Eulerian-Eulerian or Lattice-Boltzmann multiphase methods. Moreover, additional haemodynamic metrics, such as the near-wall residence time model proposed by Longest [123] or velocity and forces of blood particles at the time of impact on the host artery wall, would provide valuable information linked to the activation of blood and endothelial cells as well as the tissue response affected by the fluid-particle flow.

The benefits of trailing edge orientation were reported in terms of secondary velocity, WSS and recirculation in the host artery. However, Figure 4.6 showed a higher disturbance of particle trajectories in the region of occlusion in those configurations with enhanced swirling flow. The residual flow at the region of occlusion would be highly dependent on the degree of stenosis and thus the jet flow from the boundary considered in the present study as occlusion. The assessment of different degrees of stenosis at the occlusion and, where feasible, the use of patient-specific geometries would enable one to directly ellucidate the influence of the jet flow and obtain a rigurous prediction of the anastomosis performance.

As was alluded in Chapter 3, the investigation of the proximal anastomosis and/or the leading edge of the ridge can give rise to interesting results related to the deposition of cellular debris and fatty substances which might entail the loss of performance of the graft. This methodology has shown a high deposition of particles in the leading edge of the ridge influenced by the design parameters of ridge and graft. Further work on the proximal anastomosis could elucidate the effects of the ridge leading edge on the graft inflow conditions.

Finally, in addition to the above-mentioned points of future work of a numerical nature, *in vitro* experiments would significatly contribute by providing valuable information to validate and calibrate the multiphase methods.

Chapter 5

Conclusion and Future Work

Cardiovascular diseases are unfortunately one of the leading causes of death in the world. Arterial bypass grafts and arterio-venous grafts have become a widely used treatment of blood vessel replacement and vascular access, respectively. However, the long-term efficiency of these devices is adversely affected by the development of stenosis due to thrombosis, atherosclerosis and intimal hyperplasia, where the impact of haemodynamic metrics has been widely recognised. This thesis has studied such influences from the two traditional descriptions of fluid mechanics, Eulerian or Lagrangian formulations, linked to the concept of the blood as a homogeneous or heterogeneous fluid, respectively.

The identification of the physiological blood flow as spiral in the whole arterial system has led to novel designs of spiral-inducing prosthetic graft including spiral laminar flow peripheral vascular graft, commercialised by Vascular Flow Technologies Ltd., a design which is the main focus of the present work. Different geometrical parameters of the graft, including the cross-sectional shape, trailing edge orientation, pitch and number of ridges, were assessed with the design condition of constant

cross-sectional area of ridge(s), which enabled an appropriate performance comparison under similar conditions of vascular resistance.

Building on the above-mentioned design strategy and an improvement criteria based on the potential favourable effects of high wall shear stress, high secondary velocity and reduction of separation and recirculation zones, Chapter 3 used the traditional concept of blood as a homogeneous fluid to evaluate the secondary flow and WSS-based haemodynamic metrics under steady-state and pulsatile conditions. This investigation highlighted the influence of the elliptical ridge height and, particularly, the trailing edge orientation of the ridge on inducing swirling flow in the host artery. The interaction between the induced rotation by the spiral ridge and the lesser suppression produced by the near sidewall of the host artery upon impingement with the ridge orientation 270°, enhanced the swirling flow of this configuration in comparison with other orientations considered in this study. This design parameter has particular clinical relavance when taking into account the different rotational direction of the blood, depending on the location of the blood vessel. In this thesis, a new peripheral bypass surgery strategy was proposed by considering two grafts with optimised ridge orientation and with opposite ridge rotational direction (i.e. clockwise and anticlockwise) in order to achieve the improved and physiologically suitable rotation of the blood flow depending on the location of the stenosis.

The implementation of the Lagrangian particle tracking multiphase model enabled the consideration of the blood as a heterogeneous fluid composed of discrete particles travelling in a continuous phase. Complete information about particle trajectories and terminal locations was analysed in order to assess the influence of the different graft design parameters from the perspective of the particle disturbance and predominant regions of deposition on surrounding wall boundaries. In

agreement with the results obtained using the Eulerian methodology, the orientation of the ridge reported a great influence on particle-haemodynamics. As a result of the sweep effect produced by the spiral flow, a correlation between the regions of low-WSS and particle deposition was observed under steady-state conditions, which supports the initial optimisation criteria assumed in the Eulerian framework. However, cases with enhanced swirling flow also resulted in an increased particle disturbance in the region of occlusion although deposition of particles was only reported from the cross-section corresponding to the heel of the anastomosis. In spite of this study being focussed on the distal anastomosis, the particle transport model revealed a noteworthy impingement of particles at the leading edge.

The limitations of the present analysis, described in detail in Chapters 3 and 4, are summarised below, as suggestions for future work (given in the order to CFD workflow):

- *In-vitro experiments.* As has been proved during the last decades, numerical simulation, recently also known as *in-silico* testing, is able to rigorously model biomedical problems like bypass grafting, additionally providing information that in some cases cannot be obtained using experimental procedures. However, experimental methods, *in-vitro*, *in-vivo* or *ex-vivo* testing, cannot be discarded since they represent an indispensable tool for validating numerical results. Specifically with respect to explored methodology, experimental information could enable a complete calibration and validation of Eulerian and Lagrangian frameworks, particularly in terms of fluid-structure, fluid-particle and particle-structure interactions.

- *Patient-specific models.* The geometry of the fluid domain, together with the dynamic conditions, have a direct influence on haemodynamic results. An ide-

alised geometry of End-To-Side distal graft anastomosis has been used in this project, in the absence of access to realistic models and also in line with parallel investigations by the author's research group on the effect of non-planar helical designs of grafts, to understand the physics of the problem and assess the influence of the ridge design parameters in spiral-inducing grafts. The use of patient-specific geometries would increase the accuracy and physiology of model and consequently the results, thus enabling the implementation of a realistic degree of stenosis, contraints in the deployment of grafts, an accurate gravity direction, dimensions of the lumen, curvature and morphological details. From the clinician's point of view, it would additionally enable them to plan surgical intervations and obtain a personalised prediction of the device performance.

- *Compliance mismatch and Fluid-Structure Interaction (FSI).* Although the assumption of rigid walls in arteries and veins under the dynamic conditions considered in this problem can be considered acceptable, the analysis of the difference in mechanical properties between prosthetic graft and host artery continues to be a major challenge. Compliance mismatch has been identified as an important parameter associated with the postoperative development of restenosis around the suture line. The implementation of FSI, keeping the required accuracy and using pulsatile boundary conditions, would significantly increase the computational cost, which has posed as a limiting factor in the present project, and consequently requires the use of High Performance Computing (HPC).

- *Multiphase approaches.* In this thesis, the Lagrangian particle tracking multiphase model was selected in order to obtain complete information about the

behaviour of representative particles along its path through different design of spiral gratfs. The consideration of Eulerian-Eulerian or Lattice-Boltzmann methods would enable the implementation of larger concentrations of particles and could complement this methodology by providing additional particle-transport metrics. Likewise, should the proposed *in vitro* experiments take place, these results would be of great interest to calibrate the model of interaction and collision between particles and arterial walls.

- *Complete design optimisation.* This investigation has covered the parametric analysis of spiral grafts in order to understand the physics of the problem as well as highlighting the most relevant design parameters. The identification of the predominant influence of the elliptic ridge height and, particularly, the orientation of the ridge on haemodynamics enables researchers to narrow the search of the optimal spiral graft design and, therefore, decrease the future computational cost. Building on the results presented in this thesis, a multi-objective optimisation would result in the optimal combination of graft design parameters that would produce the most appropriate swirling blood flow to avoid the potential development of vascular diseases.

Bibliography

[1] S. Seshadhri, "Cardiovascular Engineering," *ANSYS Advantage*, 2013.

[2] D. N. Ghista and F. Kabinejadian, "Coronary artery bypass grafting hemodynamics and anastomosis design: a biomedical engineering review.," *Biomedical engineering online*, vol. 12, p. 129, 2013.

[3] C. S. Rihal, D. L. Raco, B. J. Gersh, and S. Yusuf, "Indications for coronary artery bypass surgery and percutaneous coronary intervention in chronic stable angina: review of the evidence and methodological considerations.," *Circulation*, vol. 108, no. 20, pp. 2439–45, 2003.

[4] X. Liu, A. Sun, Y. Fan, and X. Deng, "Physiological Significance of Helical Flow in the Arterial System and its Potential Clinical Applications.," *Annals of biomedical engineering*, 2014.

[5] E. Kokkalis, P. R. Hoskins, G. A. Corner, P. A. Stonebridge, A. J. Doull, and J. G. Houston, "Secondary flow in peripheral vascular prosthetic grafts using vector Doppler imaging.," *Ultrasound in medicine & biology*, vol. 39, no. 12, pp. 2295–307, 2013.

[6] H. Do, A. A. Owida, W. Yang, and Y. S. Morsi, "Numerical simulation of the haemodynamics in end-to-side anastomoses," *International Journal for Numerical Methods in Fluids*, vol. 67, no. 5, pp. 638–650, 2011.

[7] F. Loth, P. F. Fischer, and H. S. Bassiouny, "Blood Flow in End-to-Side Anastomoses," 2008.

[8] S. Sarkar, T. Schmitz-Rixen, G. Hamilton, and A. M. Seifalian, "Achieving the ideal properties for vascular bypass grafts using a tissue engineered approach: a review.," *Medical & biological engineering & computing*, vol. 45, no. 4, pp. 327–36, 2007.

[9] H. Haruguchi and S. Teraoka, "Intimal hyperplasia and hemodynamic factors in arterial bypass and arteriovenous grafts: a review.," *Journal of artificial organs : the official journal of the Japanese Society for Artificial Organs*, vol. 6, no. 4, pp. 227–35, 2003.

[10] D. N. Ku, "Blood flow in arteries," *Annual Review of Fluid Mechanics*, vol. 29, no. 1, pp. 399–434, 1997.

[11] D. F. Young, "Fluid Mechanics of Arterial Stenoses," *Journal of Biomechanical Engineering*, vol. 101, no. 3, p. 157, 1979.

[12] D. M. Wootton and D. N. Ku, "Fluid mechanics of vascular systems, diseases, and thrombosis.," *Annual review of biomedical engineering*, vol. 1, pp. 299–329, 1999.

[13] P. Losi, S. Lombardi, E. Briganti, and G. Soldani, "Luminal surface microgeometry affects platelet adhesion in small-diameter synthetic grafts.," *Biomaterials*, vol. 25, no. 18, pp. 4447–55, 2004.

[14] L. R. Sauvage, M. W. Walker, K. Berger, S. B. Robel, M. M. Lischko, S. G. Yates, and G. A. Logan, "Current arterial prostheses. Experimental evaluation by implantation in the carotid and circumflex coronary arteries of the dog.," *Archives of surgery (Chicago, Ill. : 1960)*, vol. 114, no. 6, pp. 687–91, 1979.

[15] A. M. Malek, S. L. Alper, and S. Izumo, "Hemodynamic shear stress and its role in atherosclerosis.," *JAMA*, vol. 282, no. 21, pp. 2035–42, 1999.

[16] H. C. Stary, A. B. Chandler, S. Glagov, J. R. Guyton, W. Insull, M. E. Rosenfeld, S. A. Schaffer, C. J. Schwartz, W. D. Wagner, and R. W. Wissler, "A definition of initial, fatty streak, and intermediate lesions of atherosclerosis. A report from the Committee on Vascular Lesions of the Council on Arteriosclerosis, American Heart Association.," *Circulation*, vol. 89, no. 5, 1994.

[17] D. N. Ku, D. P. Giddens, C. K. Zarins, and S. Glagov, "Pulsatile flow and atherosclerosis in the human carotid bifurcation. Positive correlation between plaque location and low oscillating shear stress.," *Arteriosclerosis (Dallas, Tex.)*, vol. 5, no. 3, pp. 293–302.

[18] J. Moore, J. E., S. E. Maier, D. N. Ku, and P. Boesiger, "Hemodynamics in the abdominal aorta: a comparison of in vitro and in vivo measurements," *J Appl Physiol*, vol. 76, no. 4, pp. 1520–1527, 1994.

[19] X. He and D. N. Ku, "Pulsatile flow in the human left coronary artery bifurcation: average conditions.," *Journal of biomechanical engineering*, vol. 118, no. 1, pp. 74–82, 1996.

[20] A. M. Imparato, A. Bracco, G. E. Kim, and R. Zeff, "Intimal and neointimal fibrous proliferation causing failure of arterial reconstructions.," *Surgery*, vol. 72, no. 6, pp. 1007–17, 1972.

[21] V. Echave, A. R. Koornick, M. Haimov, and J. H. Jacobson, "Intimal hyperplasia as a complication of the use of the polytetrafluoroethylene graft for femoral-popliteal bypass.," *Surgery*, vol. 86, no. 6, pp. 791–8, 1979.

[22] F. W. LoGerfo, W. C. Quist, M. D. Nowak, H. M. Crawshaw, and C. C. Haudenschild, "Downstream anastomotic hyperplasia. A mechanism of failure in Dacron arterial grafts.," *Annals of surgery*, vol. 197, no. 4, pp. 479–83, 1983.

[23] T. R. Kohler, T. R. Kirkman, L. W. Kraiss, B. K. Zierler, and A. W. Clowes, "Increased blood flow inhibits neointimal hyperplasia in endothelialized vascular grafts.," *Circulation research*, vol. 69, no. 6, pp. 1557–65, 1991.

[24] X. Liu, A. Sun, Y. Fan, and X. Deng, "Physiological Significance of Helical Flow in the Arterial System and its Potential Clinical Applications.," *Annals of biomedical engineering*, 2014.

[25] V. S. Sottiurai, J. S. T. Yao, R. C. Batson, S. L. Sue, R. Jones, and Y. A. Nakamura, "Distal anastomotic intimai hyperplasia: Histopathologic character and biogenesis," *Annals of Vascular Surgery*, vol. 3, no. 1, pp. 26–33, 1989.

[26] M. Sankaranarayanan, L. P. Chua, D. N. Ghista, and Y. S. Tan, "Computational model of blood flow in the aorto-coronary bypass graft.," *Biomedical engineering online*, vol. 4, p. 14, 2005.

[27] H. Ha, D. Hwang, W.-R. Choi, J. Baek, and S. J. Lee, "Fluid-dynamic optimal design of helical vascular graft for stenotic disturbed flow.," *PloS one*, vol. 9, no. 10, p. e111047, 2014.

[28] P. A. Stonebridge, P. R. Hoskins, P. L. Allan, and J. F. F. Belch, "Spiral laminar flow in vivo," *Clinical Science*, vol. 91, no. 1, pp. 17–21, 1996.

[29] B. Jung, M. Markl, D. Föll, and J. Hennig, "Investigating myocardial motion by MRI using tissue phase mapping," *European Journal of Cardio-thoracic Surgery*, vol. 29, no. SUPPL. 1, 2006.

[30] C. G. Caro, D. J. Doorly, M. Tarnawski, K. T. Scott, Q. Long, and C. L. Dumoulin, "Non-Planar Curvature and Branching of Arteries and Non-Planar-Type Flow," 1996.

[31] P. A. Stonebridge, "Three-dimensional blood flow dynamics: spiral/helical laminar flow.," *Methodist DeBakey cardiovascular journal*, vol. 7, no. 1, pp. 21–6.

[32] U. Gülan, B. Lüthi, M. Holzner, A. Liberzon, A. Tsinober, and W. Kinzelbach, "Experimental study of aortic flow in the ascending aorta via Particle Tracking Velocimetry," *Experiments in Fluids*, vol. 53, no. 5, pp. 1469–1485, 2012.

[33] L. J. Frazin, G. Lanza, M. Vonesh, F. Khasho, C. Spitzzeri, S. McGee, D. Mehlman, K. B. Chandran, J. Talano, and D. McPherson, "Functional chiral asymmetry in descending thoracic aorta.," *Circulation*, vol. 82, no. 6, pp. 1985–94, 1990.

[34] A. Frydrychowicz, J. T. Winterer, M. Zaitsev, B. Jung, J. Hennig, M. Langer, and M. Markl, "Visualization of iliac and proximal femoral artery hemodynamics using time-resolved 3D phase contrast MRI at 3T," *Journal of Magnetic Resonance Imaging*, vol. 25, pp. 1085–1092, 2007.

[35] L. J. Frazin, M. J. Vonesh, K. B. Chandran, T. Shipkowitz, A. S. Yaacoub, and D. D. McPherson, "Confirmation and initial documentation of thoracic and abdominal aortic helical flow. An ultrasound study.," *ASAIO journal (American Society for Artificial Internal Organs : 1992)*, vol. 42, no. 6, pp. 951–6.

[36] M. Kaazempur-Mofrad and C. Ethier, "Mass transport in an anatomically realistic human right coronary artery," *Annals of biomedical engineering*, 2001.

[37] P. Stonebridge and C. Brophy, "Spiral laminar flow in arteries?," *The Lancet*, vol. 338, no. 8779, pp. 1360–1361, 1991.

[38] G. Van Langenhove, J. J. Wentzel, R. Krams, C. J. Slager, J. N. Hamburger, and P. W. Serruys, "Helical velocity patterns in a human coronary artery: a three-dimensional computational fluid dynamic reconstruction showing the relation with local wall thickness.," *Circulation*, vol. 102, no. 3, pp. E22–4, 2000.

[39] S. Wetzel, S. Meckel, A. Frydrychowicz, L. Bonati, E.-W. Radue, K. Scheffler, J. Hennig, and M. Markl, "In vivo assessment and visualization of intracranial arterial hemodynamics with flow-sensitized 4D MR imaging at 3T.," *AJNR. American journal of neuroradiology*, vol. 28, no. 3, pp. 433–8, 2007.

[40] P. Bächler, N. Pinochet, J. Sotelo, G. Crelier, P. Irarrazaval, C. Tejos, and S. Uribe, "Assessment of normal flow patterns in the pulmonary circulation by using 4D magnetic resonance velocity mapping," *Magnetic Resonance Imaging*, vol. 31, no. 2, pp. 178–188, 2013.

[41] C. R. Ethier, "Computational Modeling of Mass Transfer and Links to Atherosclerosis," *Annals of Biomedical Engineering*, vol. 30, no. 4, pp. 461–471, 2002.

[42] J. G. Houston, S. J. Gandy, D. G. Sheppard, J. B. Dick, J. J. Belch, and P. A. Stonebridge, "Two-dimensional flow quantitative MRI of aortic arch blood flow patterns: Effect of age, sex, and presence of carotid atheromatous disease

on prevalence of spiral blood flow," *Journal of Magnetic Resonance Imaging*, vol. 18, no. 2, pp. 169–174, 2003.

[43] J. G. Houston, S. J. Gandy, W. Milne, J. B. C. Dick, J. J. F. Belch, and P. A. Stonebridge, "Spiral laminar flow in the abdominal aorta: a predictor of renal impairment deterioration in patients with renal artery stenosis?," *Nephrology Dialysis Transplantation*, vol. 19, no. 7, pp. 1786–1791, 2004.

[44] T. Sochi, "Non-Newtonian Rheology in Blood Circulation," 2013.

[45] O. K. Baskurt and H. J. Meiselman, "Blood Rheology and Hemodynamics," *Seminars in Thrombosis and Hemostasis*, vol. 29, no. 5, pp. 435–450, 2003.

[46] A. M. Robertson, A. Sequeira, and R. G. Owens, "Rheological models for blood," in *Cardiovascular Mathematics*, pp. 211–241, Milano: Springer Milan, 2009.

[47] P. K. Mandal, "An unsteady analysis of non-Newtonian blood flow through tapered arteries with a stenosis," *International Journal of Non-Linear Mechanics*, vol. 40, no. 1, pp. 151–164, 2005.

[48] Z. Lou and W. J. Yang, "A computer simulation of the non-Newtonian blood flow at the aortic bifurcation.," *Journal of biomechanics*, vol. 26, no. 1, pp. 37–49, 1993.

[49] R. L. Replogle, H. J. Meiselman, and E. W. Merrill, "Clinical Implications of Blood Rheology Studies," *Circulation*, vol. 36, no. 1, 1967.

[50] M. M. Molla and M. C. Paul, "LES of non-Newtonian physiological blood flow in a model of arterial stenosis.," *Medical engineering {&} physics*, vol. 34, no. 8, pp. 1079–1087, 2012.

[51] B. M. Johnston, P. R. Johnston, S. Corney, and D. Kilpatrick, "Non-Newtonian blood flow in human right coronary arteries: Transient simulations," *Journal of Biomechanics*, vol. 39, no. 6, pp. 1116–1128, 2006.

[52] L. L. Formaggia, A. Quarteroni, and A. A. Veneziani, *Cardiovascular mathematics : modeling and simulation of the circulatory system.* Springer, 2009.

[53] F. J. Gijsen, F. N. van de Vosse, and J. D. Janssen, "The influence of the non-Newtonian properties of blood on the flow in large arteries: steady flow in a carotid bifurcation model.," *Journal of biomechanics*, vol. 32, no. 6, pp. 601–8, 1999.

[54] C. Fisher and J. S. Rossmann, "Effect of non-newtonian behavior on hemodynamics of cerebral aneurysms.," *Journal of biomechanical engineering*, vol. 131, p. 91004, sep 2009.

[55] Y. H. Kim, X. Xu, and J. S. Lee, "The effect of stent porosity and strut shape on saccular aneurysm and its numerical analysis with lattice Boltzmann method.," *Annals of biomedical engineering*, vol. 38, no. 7, pp. 2274–92, 2010.

[56] J. V. Soulis, O. P. Lampri, D. K. Fytanidis, and G. D. Giannoglou, "Relative residence time and oscillatory shear index of non-Newtonian flow models in aorta," in *2011 10th International Workshop on Biomedical Engineering*, pp. 1–4, IEEE, 2011.

[57] J. Chen, X.-Y. Lu, and W. Wang, "Non-Newtonian effects of blood flow on hemodynamics in distal vascular graft anastomoses.," *Journal of biomechanics*, vol. 39, no. 11, pp. 1983–95, 2006.

[58] A. Liñán Martínez, *Mecánica de Fluidos.* Madrid: Escuela Técnica Superior de Ingenieros Aeronáuticos, 2005.

[59] T. O. Brien, M. Walsh, and T. McGloughlin, "On reducing abnormal hemodynamics in the femoral end-to-side anastomosis: the influence of mechanical factors.," *Annals of biomedical engineering*, vol. 33, no. 3, pp. 310–22, 2005.

[60] D. Y. Fei, J. D. Thomas, and S. E. Rittgers, "The effect of angle and flow rate upon hemodynamics in distal vascular graft anastomoses: a numerical model study.," *Journal of biomechanical engineering*, vol. 116, pp. 331–336, 1994.

[61] P. E. Hughes and T. V. How, "Effects of geometry and flow division on flow structures in models of the distal end-to-side anastomosis.," *Journal of biomechanics*, vol. 29, no. 7, pp. 855–72, 1996.

[62] R. Pietrabissa, F. Inzoli, and R. Fumero, "Simulation study of the fluid dynamics of aorto-coronary bypass.," *Journal of biomedical engineering*, vol. 12, no. 5, pp. 419–24, 1990.

[63] N. H. Staalsen, M. Ulrich, J. Winther, E. M. Pedersen, T. How, and H. Nygaard, "The anastomosis angle does change the flow fields at vascular end-to-side anastomoses in vivo.," *Journal of vascular surgery*, vol. 21, no. 3, pp. 460–71, 1995.

[64] R. S. Keynton, S. E. Rittgers, and M. C. Shu, "The effect of angle and flow rate upon hemodynamics in distal vascular graft anastomoses: an in vitro model study.," *Journal of biomechanical engineering*, vol. 113, no. 4, pp. 458–63, 1991.

[65] Z. S. Jackson, H. Ishibashi, A. I. Gotlieb, and B. Langille, "Effects of anastomotic angle on vascular tissue responses at end-to-side arterial grafts," *Journal of Vascular Surgery*, vol. 34, no. 2, pp. 300–307, 2001.

[66] J. D. Folts, E. B. Crowell, and G. G. Rowe, "Platelet aggregation in partially obstructed vessels and its elimination with aspirin.," *Circulation*, vol. 54, no. 3, pp. 365–70, 1976.

[67] A. A. Owida, H. Do, and Y. S. Morsi, "Numerical analysis of coronary artery bypass grafts: An over view," *Computer Methods and Programs in Biomedicine*, vol. 108, pp. 689–705, 2012.

[68] A. Qiao and Y. Liu, "Influence of graft-host diameter ratio on the hemodynamics of CABG.," *Bio-medical materials and engineering*, vol. 16, no. 3, pp. 189–201, 2006.

[69] Z. El Zahab, E. Divo, and A. Kassab, "Minimisation of the wall shear stress gradients in bypass grafts anastomoses using meshless CFD and genetic algorithms optimisation.," *Computer methods in biomechanics and biomedical engineering*, vol. 13, no. 1, pp. 35–47, 2010.

[70] S. J. Sherwin, O. Shah, D. J. Doorly, J. Peiro, Y. Papaharilaou, N. Watkins, C. G. Caro, and C. L. Dumoulin, "The Influence of Out-of-Plane Geometry on the Flow Within a Distal End-to-Side Anastomosis," *Journal of Biomechanical Engineering*, vol. 122, no. 1, pp. 86–95, 2000.

[71] Y. Papaharilaou, D. J. Doorly, and S. J. Sherwin, "The influence of out-of-plane geometry on pulsatile flow within a distal end-to-side anastomosis," *Journal of Biomechanics*, vol. 35, pp. 1225–1239, 2002.

[72] T. Zheng, Y. Fan, Y. Xiong, W. Jiang, and X. Deng, "Hemodynamic performance study on small diameter helical grafts.," *ASAIO journal (American Society for Artificial Internal Organs : 1992)*, vol. 55, no. 3, pp. 192–9, 2009.

[73] S. Giordana, S. J. Sherwin, J. Peiró, D. J. Doorly, J. S. Crane, K. E. Lee, N. J. W. Cheshire, and C. G. Caro, "Local and global geometric influence on steady flow in distal anastomoses of peripheral bypass grafts.," *Journal of biomechanical engineering*, vol. 127, no. 7, pp. 1087–98, 2005.

[74] F. Loth, S. A. Jones, D. P. Giddens, H. S. Bassiouny, S. Glagov, and C. K. Zarins, "Measurements of velocity and wall shear stress inside a PTFE vascular graft model under steady flow conditions.," *Journal of biomechanical engineering*, vol. 119, pp. 187–194, 1997.

[75] A. F. Da Silva, T. Carpenter, T. V. How, and P. L. Harris, "Stable vortices within vein cuffs inhibit anastomotic myointimal hyperplasia?," *European Journal of Vascular and Endovascular Surgery*, vol. 14, pp. 157–163, 1997.

[76] C. G. Caro, N. J. Cheshire, and N. Watkins, "Preliminary comparative study of small amplitude helical and conventional ePTFE arteriovenous shunts in pigs.," *Journal of the Royal Society, Interface / the Royal Society*, vol. 2, pp. 261–266, 2005.

[77] A. N. Cookson, D. J. Doorly, and S. J. Sherwin, "Mixing through stirring of steady flow in small amplitude helical tubes.," *Annals of Biomedical Engineering*, vol. 37, no. 4, pp. 710–721, 2009.

[78] A. Sun, Y. Fan, and X. Deng, "Numerical Comparative Study on the Hemodynamic Performance of a New Helical Graft With Noncircular Cross Section and SwirlGraft," *Artificial Organs*, vol. 34, no. 1, pp. 22–27, 2010.

[79] K. E. Lee, J. S. Lee, and J. Y. Yoo, "A numerical study on steady flow in helically sinuous vascular prostheses.," *Medical engineering & physics*, vol. 33, no. 1, pp. 38–46, 2011.

[80] A. Cookson, D. Doorly, and S. Sherwin, "Using coordinate transformation of Navier–Stokes equations to solve flow in multiple helical geometries," *Journal of Computational and Applied Mathematics*, vol. 234, no. 7, pp. 2069–2079, 2010.

[81] P. a. Stonebridge, F. Vermassen, J. Dick, J. J. F. Belch, and G. Houston, "Spiral laminar flow prosthetic bypass graft: medium-term results from a first-in-man structured registry study.," *Annals of vascular surgery*, vol. 26, no. 8, pp. 1093–9, 2012.

[82] C. Bechara, "Comparing Short and Midterm Infrainguinal Bypass Patency Rates Between Two ePTFE Prosthetic Grafts: Spiral Laminar Flow and Propaten," *Vascular Disease Management*, vol. 11, pp. E54–E58, 2014.

[83] F. Kabinejadian, M. McElroy, A. Ruiz-Soler, H. L. Leo, M. Slevin, L. Badimon, and A. Keshmiri, "Numerical Assessment of Novel Helical/Spiral Grafts with Improved Hemodynamics for Distal Graft Anastomoses," *PLOS ONE*, p. 2016.

[84] W. L. P. o. B. E. Murphy, J. Black, and G. W. Hastings, *Handbook of biomaterial properties.*

[85] D. Doorly and S. Sherwin, "Geometry and flow," in *Cardiovascular Mathematics*, pp. 177–209, Milano: Springer Milan, 2009.

[86] C. Basciano, C. Kleinstreuer, S. Hyun, and E. A. Finol, "A relation between near-wall particle-hemodynamics and onset of thrombus formation in abdominal aortic aneurysms.," *Annals of biomedical engineering*, vol. 39, no. 7, pp. 2010–26, 2011.

[87] A. Qiao, Y. Liu, and Z. Guo, "Wall shear stresses in small and large two-way bypass grafts.," *Medical engineering & physics*, vol. 28, no. 3, pp. 251–8, 2006.

[88] M. Hofer, G. Rappitsch, K. Perktold, W. Trubel, and H. Schima, "Numerical study of wall mechanics and fluid dynamics in end-to-side anastomoses and correlation to intimal hyperplasia," *Journal of Biomechanics*, vol. 29, pp. 1297–1308, 1996.

[89] D. A. Steinman and C. R. Ethier, "The effect of wall distensibility on flow in a two-dimensional end-to-side anastomosis.," *Journal of biomechanical engineering*, vol. 116, no. 3, pp. 294–301, 1994.

[90] F. M. Donovan, R. W. McIlwain, D. H. Mittmann, and B. C. Taylor, "Experimental correlations to predict fluid resistance for simple pulsatile laminar flow of incompressible fluids in rigid tubes," *Journal of Fluids Engineering, Transactions of the ASME*, vol. 116, no. 3, pp. 516–521, 1994.

[91] F. Kabinejadian, L. P. Chua, D. N. Ghista, and Y. S. Tan, "CABG models flow simulation study on the effects of valve remnants in the venous graft," *Journal of Mechanics in Medicine and Biology*, vol. 10, no. 04, pp. 593–609, 2010.

[92] F. Kabinejadian, F. Cui, B. Su, A. Danpinid, P. Ho, and H. L. Leo, "Effects of a carotid covered stent with a novel membrane design on the blood flow regime and hemodynamic parameters distribution at the carotid artery bifurcation.," *Medical & biological engineering & computing*, vol. 53, no. 2, pp. 165–77, 2015.

[93] R. Bird, R. C. Armstrong, and O. Hassanger, *Dynamics of polymeric liquids, Fluid mechanics*, vol. 25. 1987.

[94] F. Kabinejadian and D. N. Ghista, "Compliant model of a coupled sequential coronary arterial bypass graft: Effects of vessel wall elasticity and non-Newtonian rheology on blood flow regime and hemodynamic parameters distribution," *Medical Engineering and Physics*, vol. 34, pp. 860–872, 2012.

[95] K. Perktold and G. Rappitsch, "Computer simulation of local blood flow and vessel mechanics in a compliant carotid artery bifurcation model," *Journal of Biomechanics*, vol. 28, no. 7, pp. 845–856, 1995.

[96] ANSYS, "ANSYS CFX-Solver Theory Guide," tech. rep., ANSYS, Canonsburg, PA, USA, 2016.

[97] ANSYS, "ANSYS CFX-Solver Modeling Guide," tech. rep., ANSYS, Inc., Canonsburg, PA, USA, 2016.

[98] B. Su, Y. Huo, G. S. Kassab, F. Kabinejadian, S. Kim, H. L. Leo, and L. Zhong, "Numerical investigation of blood flow in three-dimensional porcine left anterior descending artery with various stenoses," *Computers in Biology and Medicine*, vol. 47, pp. 130–138, 2014.

[99] V. Peiffer, S. J. Sherwin, and P. D. Weinberg, "Does low and oscillatory wall shear stress correlate spatially with early atherosclerosis? A systematic review," 2013.

[100] U. Olgac, V. Kurtcuoglu, S. C. Saur, and D. Poulikakos, "Identification of atherosclerotic lesion-prone sites through patient-specific simulation of low-density lipoprotein accumulation," in *Lecture Notes in Computer Science (including subseries Lecture Notes in Artificial Intelligence and Lecture Notes in Bioinformatics)*, vol. 5242 LNCS, pp. 774–781, 2008.

[101] P. Siogkas, A. Sakellarios, T. P. Exarchos, L. Athanasiou, E. Karvounis, K. Stefanou, E. Fotiou, D. I. Fotiadis, K. K. Naka, L. K. Michalis, N. Filipovic, and O. Parodi, "Multiscale - Patient-specific artery and atherogenesis models," *IEEE Transactions on Biomedical Engineering*, vol. 58, pp. 3464–3468, 2011.

[102] K. C. Koskinas, C. L. Feldman, Y. S. Chatzizisis, A. U. Coskun, M. Jonas, C. Maynard, A. B. Baker, M. I. Papafaklis, E. R. Edelman, and P. H. Stone, "Natural history of experimental coronary atherosclerosis and vascular remodeling in relation to endothelial shear stress: A serial, in vivo intravascular ultrasound study," *Circulation*, vol. 121, pp. 2092–2101, 2010.

[103] Y. S. Chatzizisis, A. B. Baker, G. K. Sukhova, K. C. Koskinas, M. I. Papafaklis, R. Beigel, M. Jonas, A. U. Coskun, B. V. Stone, C. Maynard, G. P. Shi, P. Libby, C. L. Feldman, E. R. Edelman, and P. H. Stone, "Augmented expression and activity of extracellular matrix-degrading enzymes in regions of low endothelial shear stress colocalize with coronary atheromata with thin fibrous caps in pigs," *Circulation*, vol. 123, pp. 621–630, 2011.

[104] D. L. Fry, "Certain Chemorheologic Considerations Regarding the Blood Vascular Interface with Particular Reference to Coronary Artery Disease," 1969.

[105] C. Kleinstreuer, M. Nazemi, and J. P. Archie, "Hemodynamics Analysis of a Stenosed Carotid Bifurcation and its Plaque-Mitigating Design," *Journal of Biomechanical Engineering*, vol. 113, no. 3, p. 330, 1991.

[106] K. Perktold and M. Resch, "Numerical flow studies in human carotid artery bifurcations: basic discussion of the geometric factor in atherogenesis.," *Journal of biomedical engineering*, vol. 12, pp. 111–123, 1990.

[107] K. Perktold, R. O. Peter, M. Resch, and G. Langs, "Pulsatile non-Newtonian blood flow in three-dimensional carotid bifurcation models: a numerical study of flow phenomena under different bifurcation angles.," *Journal of biomedical engineering*, vol. 13, pp. 507–515, 1991.

[108] J.-J. Chiu and S. Chien, "Effects of disturbed flow on vascular endothelium: pathophysiological basis and clinical perspectives.," *Physiological reviews*, vol. 91, pp. 327–387, 2011.

[109] A. Ruiz-Soler, F. Kabinejadian, M. Slevin, P. J. Da Silva Bartolo, and A. Keshmiri, "Optimisation of a Novel Spiral-Inducing Bypass Graft Using Computational Fluid Dynamics," *Scientific Reports (in-review)*, 2017.

[110] H. K. Moffatt and A. Tsinober, "Helicity in Laminar and Turbulent Flow," *Annual Review of Fluid Mechanics*, vol. 24, no. 1, pp. 281–312, 1992.

[111] P. E. Vincent, A. M. Plata, A. A. E. Hunt, P. D. Weinberg, and S. J. Sherwin, "Blood flow in the rabbit aortic arch and descending thoracic aorta.," *Journal of the Royal Society, Interface / the Royal Society*, vol. 8, no. 65, pp. 1708–19, 2011.

[112] M. McElroy and A. Keshmiri, "Impact of using conventional inlet/outlet boundary conditions on haemodynamic metrics in a subject-specific rabbit aorta," *Proceedings of the Institution of Mechanical Engineers, Part H: Journal of Engineering in Medicine*, 2017.

[113] W. M. Klein, L. W. Bartels, L. Bax, Y. van der Graaf, and W. P. Mali, "Magnetic resonance imaging measurement of blood volume flow in peripheral arteries in healthy subjects," *Journal of Vascular Surgery*, vol. 38, no. 5, pp. 1060–1066, 2003.

[114] V. Peiffer, S. J. Sherwin, and P. D. Weinberg, "Computation in the rabbit aorta of a new metric - the transverse wall shear stress - to quantify the multidirectional character of disturbed blood flow.," *Journal of biomechanics*, vol. 46, no. 15, pp. 2651–8, 2013.

[115] P. D. Ballyk, C. Walsh, J. Butany, and M. Ojha, "Compliance mismatch may promote graft-artery intimal hyperplasia by altering suture-line stresses.," *Journal of biomechanics*, vol. 31, no. 3, pp. 229–37, 1998.

[116] M. Massoudi, J. Kim, and J. F. Antaki, "Modeling and numerical simulation of blood flow using the theory of interacting continua," *International Journal of Non-Linear Mechanics*, vol. 47, no. 5, pp. 506–520, 2012.

[117] W.-T. Wu, N. Aubry, M. Massoudi, J. Kim, and J. F. Antaki, "A numerical study of blood flow using mixture theory," *International Journal of Engineering Science*, vol. 76, pp. 56–72, 2014.

[118] J. Jung, A. Hassanein, and R. W. Lyczkowski, "Hemodynamic Computation Using Multiphase Flow Dynamics in a Right Coronary Artery," *Annals of Biomedical Engineering*, vol. 34, no. 3, pp. 393–407, 2006.

[119] J. Jung and A. Hassanein, "Three-phase CFD analytical modeling of blood flow," *Medical Engineering & Physics*, vol. 30, no. 1, pp. 91–103, 2008.

[120] C. Ou, W. Huang, M. M.-F. Yuen, and Y. Qian, "Hemodynamic modeling of leukocyte and erythrocyte transport and interactions in intracranial aneurysms by a multiphase approach," *Journal of Biomechanics*, vol. 49, no. 14, pp. 3476–3484, 2016.

[121] D. Fabbri, Q. Long, S. Das, and M. Pinelli, "Computational modelling of emboli travel trajectories in cerebral arteries: influence of microembolic particle size and density," *Biomechanics and Modeling in Mechanobiology*, vol. 13, no. 2, pp. 289–302, 2014.

[122] N. Johnson, J. Abraham, Z. Helgeson, and M. Hennessey, "Numerical Simulation of Blood Flow in the Presence of Embolizing Agents," in *Volume 2: Biomedical and Biotechnology Engineering*, pp. 191–198, ASME, 2010.

[123] P. W. Longest, *Computational Analyses of Transient Particle Hemodynamics with Applications to Femoral Bypass Graft Designs*. PhD thesis, 2003.

[124] P. W. Longest, C. Kleinstreuer, and J. P. Archie, "Particle hemodynamics analysis of Miller cuff arterial anastomosis.," *Journal of vascular surgery*, vol. 38, no. 6, pp. 1353–62, 2003.

[125] P. W. Longest, C. Kleinstreuer, and A. Deanda, "Numerical Simulation of Wall Shear Stress and Particle-Based Hemodynamic Parameters in Pre-Cuffed and Streamlined End-to-Side Anastomoses," *Annals of Biomedical Engineering*, vol. 33, no. 12, pp. 1752–1766, 2005.

[126] C. A. Basciano, *Computational Particle-Hemodynamics Analysis Applied to an Abdominal Aortic Aneurysm with Thrombus and Microsphere-Targeting of Liver Tumors.* PhD thesis, North Carolina State University, 2010.

[127] C. Basciano, C. Kleinstreuer, S. Hyun, and E. A. Finol, "A relation between near-wall particle-hemodynamics and onset of thrombus formation in abdominal aortic aneurysms," *Annals of Biomedical Engineering*, vol. 39, no. 7, pp. 2010–2026, 2011.

[128] M. M. Dupin, I. Halliday, C. M. Care, L. Alboul, and L. L. Munn, "Modeling the flow of dense suspensions of deformable particles in three dimensions," *Physical Review E*, vol. 75, no. 6, p. 066707, 2007.

[129] J. R. Clausen, D. A. Reasor, and C. K. Aidun, "Parallel performance of a lattice-Boltzmann/finite element cellular blood flow solver on the IBM Blue Gene/P architecture," *Computer Physics Communications*, vol. 181, no. 6, pp. 1013–1020, 2010.

[130] J. Zhang, P. C. Johnson, and A. S. Popel, "Effects of erythrocyte deformability and aggregation on the cell free layer and apparent viscosity of microscopic blood flows," *Microvascular Research*, vol. 77, no. 3, pp. 265–272, 2009.

[131] J. Wen, K. Liu, K. Khoshmanesh, W. Jiang, and T. Zheng, "Numerical investigation of haemodynamics in a helical-type artery bypass graft using non-Newtonian multiphase model," *Computer Methods in Biomechanics and Biomedical Engineering*, vol. 18, no. 7, pp. 760–768, 2015.

[132] A. E. Randles, *Modeling Cardiovascular Hemodynamics Using the Lattice Boltzmann Method on Massively Parallel Supercomputers.* PhD thesis, Harvard University, 2013.

[133] J. Nunziato, "A Multiphase Mixture Theory for Fluid-Particle Flows," in *Theory of Dispersed Multiphase Flow*, pp. 191–226, 1983.

[134] M. L. Turgeon, *Clinical hematology : theory and procedures.* Lippincott Williams & Wilkins, 2004.

[135] E. Ponder, "The relation between red blood cell density and corpuscular hemoglobin concentration," *Journal of Biological Chemistry*, vol. 144, pp. 333–338, jul 1942.

Appendix A

Publications

The present research has generated the following publications:

Journal Articles

1. **Andres Ruiz-Soler**, Foad Kabinejadian, Mark A. Slevin, Paulo J. Bartolo and Amir Keshmiri. 2017. "Optimisation of a Novel Spiral-Inducing Bypass Graft Using Computational Fluid Dynamics". *Scientific Reports, Nature.* DOI: 10.1038/s41598-017-01930-x.

2. Foad Kabinejadian, Michael McElroy, **Andres Ruiz-Soler**, Hwa Liang Leo, Mark Slevin, Lina Badimon and Amir Keshmiri. 2016. "Numerical Assessment of Helical and Spiral Grafts in Improving the Hemodynamics of Distal Graft Anastomoses". *PLoS ONE* 11(11): e0165892. DOI: 10.1371/journal.pone.0165892.

3. Amir Keshmiri, **Andres Ruiz-Soler**, Michael McElroy and Foad Kabinejadian. "Numerical Investigation on the Geometrical Effects of Novel Graft Designs for Peripheral Artery Bypass Surgery". *J. Procedia CIRP*, Vol. 49, 2016, 147–152. DOI: 10.1016/j.procir.2015.11.005.

4. Michael McElroy, **Andres Ruiz-Soler** and Amir Keshmiri. "Left Ventricular Assist Devices: Impact of Flow Ratios on the Localisation of Cardiovascular Diseases Using Computational Fluid Dynamics". *J. Procedia CIRP*, Vol. 49, 2016, 163–169. DOI: 10.1016/j.procir.2015.11.008.

Conference Papers

1. **Andres Ruiz-Soler** and Amir Keshmiri. "Hemodynamic Performance of Spiral Grafts using Eulerian and Lagrangian Frameworks". *5th International Conference on Computational and Mathematical Biomedical Engineering*, Pittsburgh, United States. April 2017.

2. **Andres Ruiz-Soler** and Amir Keshmiri. "The Parametric Study of a Spiral-Inducing Bypass Graft Using Computational Fluid Dynamics". *2nd International Conference on CFD in Medicine and Biology*, Albufeira, Portugal. September 2015.

3. **Andres Ruiz-Soler** and Amir Keshmiri. "Numerical Investigation of Design Parameter Effects on Hemodynamics in a Novel Spiral-Inducing Bypass Graft". *25th Congress of the International Society of Biomechanics*, Glasgow, UK. July 2015.